universität wien

DISSERTATION / DOCTORAL THESIS

Titel der Dissertation /Title of the Doctoral Thesis

„Generation of arbitrary light patterns and their application“

verfasst von / submitted by

Mario Rusev, BSc

angestrebter akademischer Grad / in partial fulfilment of the requirements for the degree of

Doktor der Naturwissenschaften (Dr. ret. nat.)

Wien, 2016 / Vienna 2016

Studienkennzahl lt. Studienblatt / degree programme code as it appears on the student record sheet:	A 307 270
Dissertationsgebiet lt. Studienblatt / field of study as it appears on the student record sheet:	Physik
Betreut von / Supervisor:	o. Univ. Prof. DDr.h.c. Anton Zeilinger/ degree(s) first name family name

Contents

To my parents. Rest in peace.

Acknowledgements

During the years I spent at the Institute for Quantum Optics and Quantum Information in Vienna I had the pleasure of meeting many exceptionally interesting people. Many of them have contributed to the work that I did over the past years of my Doctorate and have taught me many lessons I am sure I would use in the future. I would also like to posthumously thank my parents for supporting me lovingly at the very beginning of the project. I will greatly miss them both and I dedicate the memories spent at IQOQI to their eternal special presence in my heart.

I would like to sincerely thank Prof. Anton Zeilinger for teaching me the fundamental ways of looking at Physics and much more. He was like a father figure to me and has helped me immensely throughout my endeavor. He is an incredible person and the most intelligent person I know. I would like to also thank all other professors from the Physics department at University of Vienna, University of Innsbruck and the Technical University of Vienna, who have taught me useful lessons in Physics.

Many thanks for the Ultracold Atom Correlations Lab, which I had the pleasure to interact with. Maximilian Ebner, Mateusz Kotyrba, Michael Keller and Mariusz Semczuk, all of which were instrumental in my development as a doctoral candidate. I would also like to thank all IQOQI members for their collaboration and friendly atmosphere, as well as our technician Roland Blach, who has helped us in many crucial steps in developing the technology needed to run our experiments.

This thesis would have not been possible without the funding support form the University of Vienna, the Austrian Science Fund and the Special Research Programme (SFB F 4007), SFB “FoQuS” F 4007-N23.

I would also like to thank the teachers at Iki Language Institute, for teaching me German and making it fun and interesting, thus allowing me to reach the ÖSD C1 level in three years of German exposure. Their assistance is immensely appreciated.

Introduction

At the beginning of 20^{th} century two revolutionary theories were formulated, namely quantum mechanics and relativity, which revolutionized the world, as we know it. Even though we nowadays use devices that are based on quantum mechanics, the full potential of the quantum mechanics field has not yet been realized to its most of extent. One example is quantum information, which finds applications not only in cryptography, but also in other fields like chemistry and biology. Entanglement has been proven on various occasions in different systems such as ions [45, 46], superconducting qubits [47], cold atomic ensembles [48], and photons [49]. Entanglement is one of the most groundbreaking discoveries in the realm of quantum physics and a seminal ingredient in quantum information science. However, the original states proposed by Einstein, Podolsky and Rosen, still wait to be experimentally tested. The idea involves entanglement in the external degrees of freedom, position and momentum, of massive particles. With the advent of Bose Einstein Condensates (BEC), which Bose and Einstein successfully predicted in 1924 (that particles with integer spin at extremely low temperatures will tend to collapse into a single quantum state), a new state of matter has been established. Laser cooling and trapping techniques allow the experimenter to prepare gaseous samples of atoms at very low temperatures. Quantum gases then are one of the most active fields of atomic physics nowadays. Moreover, the ability to implement single atom detection opens the crossroads to performing matter-wave analogue experiments [50, 52] and some of the pioneering photon-entanglement experiments [53, 54]. It opens a garden variety of opportunities in fundamental physics, many-body physics etc.

In this thesis, I present some of the advances we have achieved in the past 3 years and my contribution to that. Generally, spatial light modulators open a new door to implementing various light configurations or trap potentials

with atomic ensembles, as well as imparting quantized angular momentum on a BEC. Such trap configurations can be utilized to exploit interesting experiments in Physics, using the SLM to create boxes, light sheets, gratings, arrays of traps and others. Our experiments in plan are concerned with being able to employ arbitrary light patterns (in our case Gaussian spots with controllable parameters) and imprint them on an atom ensemble. The SLM devices have also been successfully used in quantum communication protocols and orbital angular momentum experiments (feats already achieved by the Zeilinger group in the past). Optical dipole traps are also of great advantage, since they can confine both magnetically sensitive and insensitive states. We have been recently able to produce optical dipole traps (ODT) with our setup. Furthermore, specific features of matter waves such as Fermi statistics and gravity sensitivity can extend the possibilities of experiments we can further do.

Outline of this thesis

In Chapter 1 I discuss the specific technical features of spatial light modulators, their application, specific functionality and ways of proper utilization. Furthermore, I discuss the problems we have come across over time in terms of realizing the holograms we want to produce properly and with high quality according to the modern standard of realization in various groups around the world. Some theoretical work on this subject needed to be performed as well in the form of modeling and some brief portion of that is discussed as well. We choose one particular algorithm (Vector Holography) since it performs the best in terms of quality of spots. The size of the spots is diffraction limited though, but can be simply changed with an iris and proper algorithmic intensity compensation. The controllability in terms of position, variety of patterns, quality of spots, focal length of each pattern, relative distance between patterns is controlled with very good precision in the order of 10um (the diameter of a diffraction limited Gaussian in this case limited by the optimization camera we use).

In the second chapter, I present the experiment we would like to perform realizing entanglement of external degrees of freedom. This experiment was already presented in the thesis of Maximilian Ebner. Therefore, I briefly discuss the idea and present the theoretical framework that was added to it in order to model possible realizations of induced noise by the SLM or non-homogeneous density of the trapped Bose-Einstein condensate.

The third chapter is concerned with our work with optical dipole traps. It presents some of the technical work I was involved with and the experiment I was directly involved with, namely scattering of an optically trapped Bose-Einstein condensate on an optical lattice.

Chapter 4 is concerned with results from experimental realization of the outcoupling with Raman pulses of atoms from

the Bose-Einstein condensate ensemble, which we have also performed with the optically trapped Bose-Einstein condensate.

Chapter 5 is a note of the similarity between a Bose-Einstein condensate and a parametric-down-conversion crystal, which I find is striking because of the broadened range of experiments in Quantum Optics that this may allow us to do in the future.

In chapter 6 I propose two types of experiments, which we can do in the near future. That is a test of Born's rule, or Kolmogorov sum rule and the interplay between the exciting field of orbital angular momentum photons and a Bose-Einstein condensate.

Chapter 7 is a brief summary of the message I wanted to convey with this thesis, followed by a brief appendix that I found necessary to the general reader to have, and references I used in the dissertation.

1. Spatial light modulators

1.1. Introduction

Most experiments in Bose-Einstein condensation are carried out in harmonic potentials, where considerable effort is usually engaged in controlling the laser frequency, polarization, intensity, and alignment of many laser beams, used to manipulate and probe an atom ensemble. However, little attempt is typically made to sculpt a laser beam's profile beyond the simple Gaussian mode. While a parabolic potential is relatively easy to produce, it is not the most revealing trap shape in which to study many-body quantum mechanics and to combine potentials with small distance separation on the order of micrometers in a readily controllable manner. It is known that different trap geometries can produce different dispersion relations, different transport properties and different three-body loss rates for instance [1, 2, 3].

Three- and two-body losses are important for the following reason: as discussed in the thesis of our former group member, Mateusz Kotyrba, a magneto-optical trap (MOT) of metastable helium is very peculiar as compared to the typical MOT of alkali atoms, used in most other experiments in degenerate quantum gases. The simple level structure of *He* allows the experimenter to use a single laser frequency for the MOT. Also, the two-body loss rate is higher than for other species because of Penning ionization, leading to a short lifetime of the cloud [55]. Penning ionization is a collisional process de-exciting the metastable helium atom back to the ground state and ionizing the collisional partner. [55] We would therefore have to be careful of the trap configuration, be it magnetic or optical dipole trap. Providing the flexibility for different trap configurations would lead to a different cloud density, exploring that process or reducing the rate even further. Keeping the density of atoms as low as possible does the usual minimization of Penning ionization, which sets limit on the MOT size and laser detuning and power thereof, for example.

It is a major experimental challenge to combine controlled collisions with the loading and addressing of individually trapped atoms in an optical dipole trap or a magnetic trap too. There are techniques that actually exist to confine single atoms in micrometer-size or larger traps [4,5]. Our group has also recently demonstrated the ability to trap atoms in an optical dipole trap (discussed later on).

One can even design an array micrometer-sized of optical traps with a spatial light modulator (SLM) for storing a single atom per trap and manipulation of individual trapping sites [6]. That requires the traps to be reconfigurable and addressed individually, which is readily done with holographic techniques. Neutral atoms then are one of the most promising candidates for storing and processing quantum information. A qubit can be encoded in the internal or motion state of an atom, and several qubits can be entangled using light-atom interaction or atom-atom interaction. Schemes for quantum gates even have been theoretically proposed that rely on dipole-dipole interactions [95-99] or controlled collisions [100-103]. These are examples of seminal ideas, which require the utilization of micro trap arrays, which we are namely able to produce with holographic techniques. Holography was first demonstrated as a way to record both the phase and amplitude of light scattered from an object in order to reconstruct the light field when the object was absent. [11] Nowadays this refers to the process of computationally reconstructing a desired light pattern by altering light's phase and/or amplitude in one control plane. Such holographic techniques change the phase of the optical field at each pixel without attenuating the amplitude.

In many such applications, including ours, SLMs are used as phase modulators (for a brief idea of how it works see Figure 1), since they preserve the light intensity. One of our goals was to be able to generate a controllable array of Gaussian beams of arbitrary number with controllable intensity. Our choice of top performance algorithm is Vector holography, described later. The SLM type used is the Hamamatsu X10468-03 LCOS-SLM. That is a reflective type of pure SLM, based on Liquid Crystal on Silicon (LCOS) technology in which the Liquid Crystal (LC) is controlled by a direct voltage source, thereby modulating the wavefront of a light beam. We control the device through a standard digital video interface (DVI) connection. In principle it behaves almost like a mirror (if of course no pattern is projected), which can be used to encode a two-dimensional phase pattern on the reflected beam, thereby acting like a phase grating. The amount of phase shift can be controlled by varying the optical path length, accomplished by the orientation of the molecules in a layer of parallel-aligned (PAL) liquid crystals. The SLM consists of a LC layer deposited on a dielectric mirror, behind which there is an amorphous silicon photoconductive layer. That is typically placed in between two transparent electrodes. The orientation of the LC

molecules is determined by the electric field, which is controlled locally by changing the impedance of the layer with photoconductive crystals. The total active area of the SLM is 16 by 12 mm, 800 by 600 pixels with a pixel fill factor of approximately 95%. The typical efficiency for which it is commercially optimized is 95% at 1064 nm. Therefore we had to correct the response of the SLM crystals for use at 1083 nm, the wavelength of our choice. The refresh rate of the SLM is 60 Hz, which is the standard refresh rate of a DVI connection.

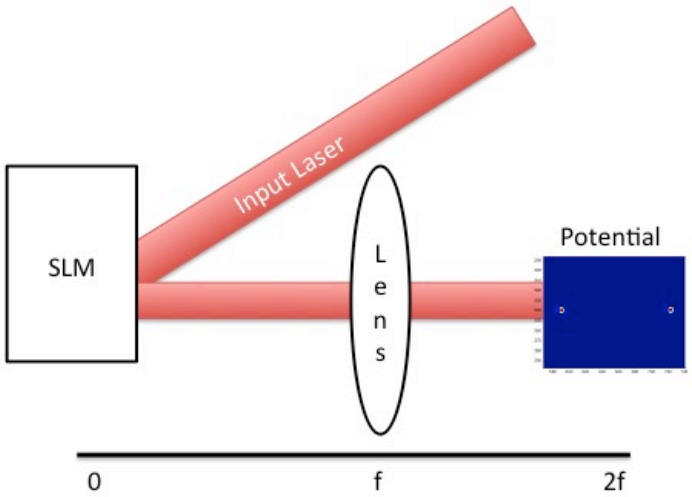

Figure 1. An illustration of the simplest use of a Spatial Light Modulator: The incoming laser field is reflected on the SLM surface, picking up the phase imprinted on the device. That Fourier plane is then imaged on the focus point of a lens (the lens does approximately the inverse Fourier transform of the light field impinging on it).

1.2. Algorithms for hologram generation

1.2.1. Gerchberg Saxton (GS) algorithm

The first-developed iterative algorithm to produce a light pattern of an arbitrary geometrical shape is the Gerchberg Saxton (GS) algorithm [7]. It is an iterative fast Fourier transform algorithm, which exploits a numerical method to calculate the optimal phase modulation of the laser beam, incident on the SLM, in order to get the desired intensity pattern on the image plane. It is the most widely

implemented and easiest algorithm to produce arbitrary light patterns.

Basically, what it tries to achieve is the relation between the intensity at the focal plane of a lens and the necessary phase modulation at the input plane of the SLM ($E_0(r)$). The algorithm stars with an initial phase guess $\varphi_0(r)$, which in many cases is a random phase pattern as a starting point. For other algorithms derived from it, it is a spherical phase pattern for example. Imposing either a free parameter Gaussian laser modulus or unity (for uniform illumination at the SLM, E_0=1) resulting in the field right after the SLM

$$A_1^n(r) = |E_0(r)|e^{i\,\varphi_n(r)}$$

where "n" signifies the iteration number in the loop between imaging plane and SLM plane (figure 2). The parameter $E_0(r)$ is the light field impinging on the SLM initially. In order to simplify this we use uniform illumination (the light field impinging on the SLM initially is much bigger than the SLM size, in our case a factor of 6). We have also imposed Gaussian illumination, but that adds three extra free parameters (width and position), estimating where the SLM is illuminated and is alignment dependent. One way to overcome this is to illuminate the SLM with a very large Gaussian beam (large is of course relative, for our purposes a beam six times the SLM size was enough), such that the illumination at the input plane is close to uniform. This was the initialization step. Now follow the iterative part. Propagating to the output plane, or focus plane of the lens can be done with a Fourier transform, which assumes the paraxial approximation in focusing optics [9]. The idea is that the lens then does the Fourier transform in real space, approximately. That results in the field propagated in the output plane

$$A_2^n(r) = F\{A_1^n\}$$

This would be in principle the patter that we obtain after the lens. However, in the loop we then have to replace the resulting field's amplitude with a desired pattern $P(r)$ and take the phase of A_2^n , which combined produces the following

$$A_3^n(r) = P(r)e^{i \arg(A_2^n)}$$

That is a field, imposed in the imaging plane at the focus point of the lens. Once this is achieved, we have to propagate the field back to the SLM plane, taking the inverse Fourier transform producing

$$A_4^n(r) = F^{-1}\{A_3^n\}$$

At this point, we can either take the phase of this field, or arg (A_4^n) as the produced hologram (also known as kinoform), if the Fourier transform of that phase is considerably close to the desired pattern, for our estimates the error boundary is a deviation of 0.1%, which turns out to require at least 15 iterations. If not (that is $F\{\arg(A_4^n)\} \neq P(r)$), we take arg (A_4^n) and replace it in the first step of the algorithm as a starting initial guess until the Fourier transform of the kinoform produces the desired pattern within the error boundary.

The algorithm can also start with the target intensity and a random phase pattern (used again crudely as a guess of the initial phase modulation). In principle, if the incoming beam at the SLM surface is big enough, this accompanies for this unity (E_0) quite well. We chose to expand the beam before the SLM in order to minimize the free parameters estimate in the algorithm and therefore make it faster. Else, we could use a Gaussian profile if the incoming beam is for example as wide as the SLM surface (say 16 by 16 mm), which does not provide any advantage in quality of the phase pattern obtained or intensity profile of the spots at the focal plane of the lens. The only significant difference observed is the quality of the pattern among algorithms, discussed later.

Once the hologram is calculated, it can be modified by changing various parameters: modulation area of the SLM can be reduced or changed in shape, translated to optimize a match with the beam's size and position, and the modulation amplitude can be varied for optimal diffraction efficiency, which is a subject of the problems needed to overcome when using a Spatial Light Modulator, discussed further.

Our target was producing two Gaussian spots with variable intensity and relative position in the micrometer scale, the produced pattern is (1 pixel = 4.65 um) diffraction limited. It is, however possible to go to larger Gaussian beams. The problem with this is that

phase or optical vortices appear in the trapping plane and are locked in the code immediately at the beginning of the execution. That is usually a sign of the finite size of the hologram and sudden, steep intensity variation. The MRAF algorithm and OMRAF algorithm further reduce the vortex count, but not completely remove it. The flooring of the number of optical vortices has to do with the finiteness of the hologram size, and the fact that the Fourier transform is not taken in the infinity limit algorithmically. Due to the physical limitation of the finite size of the transform and SLM, there is no algorithm that would completely remove the vortices, but rather floor them to a particular minimal value, based on the algorithm. An illustration of the basic structure of the GS algorithm is available at Figure 2. On a further note, the actual lens operation and propagation can be further improved with a Helmholtz propagator, which is done in the OMRAF algorithm, but can also be conceived as being implemented here instead of the Fourier transform.

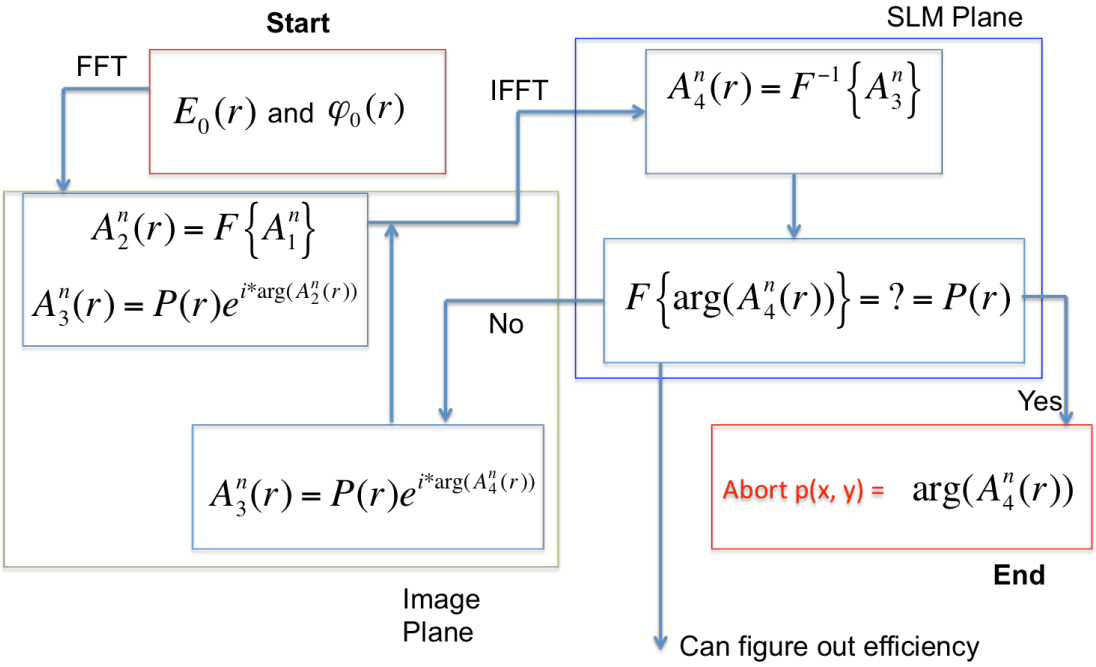

Figure 2. The basic structure of the GS algorithm, running between two planes of interest: the trapping plane (image plane) and SLM plane (pattern projected as hologram). The efficiency and error is estimated algorithmically, where the standard deviation of the image expected is at least 0.1%, which is when the algorithm stops execution and the kinoform is sent to the SLM as a value in [0, 255].

1.2.2. Mixed Region Amplitude Freedom (MRAF) algorithm

For generating more complex patterns with reduced intensity fluctuations one can implement the MRAF algorithm. [8] In many ways the MRAF algorithm is similar to the GS algorithm since it has in its core the GS algorithm. However, what is central to the MRAF algorithm is the introduction of a restricted amplitude freedom to some region of the output plane and the use of one single mixing parameter, m. The primary reason for the development of the MRAF algorithm at the time were the demand for more complex light patterns and the elimination of optical vortices, a problem discussed later on, in order to generate a high quality optical field at the focal plane of the lens. The main difference is the definition of a region where $P(r) > 0$together with some narrow canvas C of zero intensity around this region. That clearly changes the field amplitude A_3^n resulting in

$$A_3^n(r) = m\, P(r) e^{i \arg(A_2^n)}$$

if the region is within interest or

$$A_3^n = (1 - m) A_2^n(r)$$

if the region is outside of the canvas. The mixing parameter m can be chosen for giving some minimum RMS deviation in terms of intensity fluctuations, which in our case turns out to be 0.38. Some implementations can also start with a quadratic phase guess for the initial starting phase. However, optical vortices are still present and can be even further minimized by the offset MRAF algorithm [10].

Because of the canvas imperfections, the region around the spots looks significantly worse as compared to the GS, while the fluctuations within the canvas are between 3% and 5% of the maximum intensity of the traps. However the traps themselves look significantly better. (1 pixel = 4.65 um) again diffraction limited. Spots larger than the diffraction size look significantly better than the GS algorithm, however the region of canvas has fluctuations in intensity, which for our experiment would be problematic and exhibit optical vortices.

1.2.3. Offset MRAF (OMRAF) algorithm

This algorithm is the present best in terms of very complex improved algorithms for design of arbitrary two-dimensional holographic traps for ultracold atoms. It builds on the MRAF algorithm.

OMRAF modifies the MRAF algorithm by a few changes. First, the canvas is expanded, such that the trapping region covers the maximum theoretical size, which is set by Nyquist's criterion (25% of the trapping plane). The diffraction limited spot size is of size 1 pixel again. In order to reduce the minimum pixel size by 50%, we would have to increase the area of the SLM twice, which means that 25% of the simulated "SLM plane" is in fact covered by the physical size of the SLM and therefore we can only control 25% of the "trapping plane", as discussed in detail in [10]).

Furthermore, we can provide an offset to the desired trapping region, where its zero reference is slightly shifted, which does not change the physics of the trap itself, but it reduces the number of optical vortices upon increase of trap size algorithmically. The vortices are again not completely removed, but rather floored to a minimal value.

Perhaps the best improvement to MRAF is the introduction of an efficient Helmholtz solver, solving the propagation and lens approximation to different than the Fourier transform [10]. The Helmholtz equation for light propagation in free space gives that the Fourier transform of a light field is modified by a phase factor. One way to include this in the computational portion of the algorithm is to decompose that into 3 stages: first, propagation from the SLM to the imaging lens and adding that particular computational phase estimate. Then applying a lens in Fourier space and finally propagating to the trapping plane. The resulting is a transform, which describes the behavior of the light field much better for light propagating from the SLM to the lens and trapping plane and back.

The results are striking because the Helmholtz estimate gives a 3% reduction of the RMS intensity fluctuations error across the trap, which totals about 20% reduction compared to MRAF [10] within perfect alignment.

One example of realization of the OMRAF for a complex trapping potential is (1 pixel = 4.65 um) shown in Figure 3.

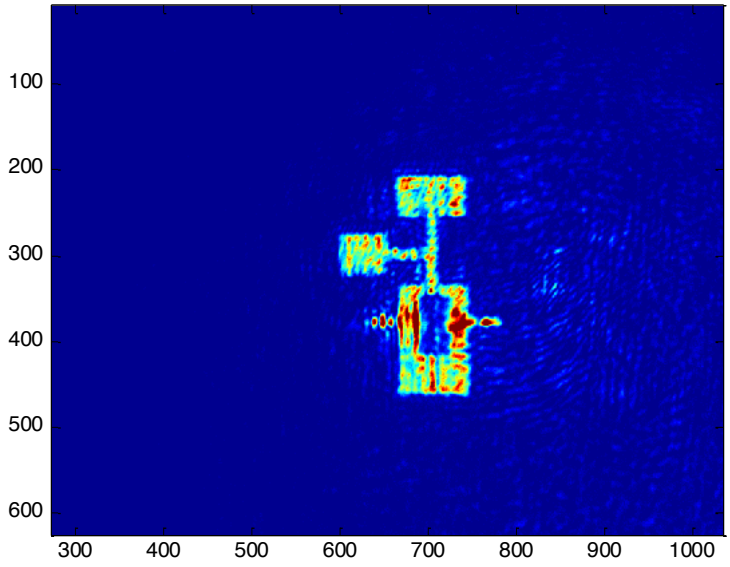

Figure 3. A complex potential implementation with the OMRAF algorithm, also known as the transistor potential: it was not implemented with the atoms; wavefront corrections were not implemented at this stage. It is however, close to what the authors of [10] obtain.

We have performed a test of adding the Helmholtz solver to the GS algorithm and using the GS on the fly. However, the results do not lead to a huge improvement in the spot quality. The algorithm that produces the top quality spots (as long as they don't overlap, which for our experiments considered is not important) is discussed in the next section.

1.2.4 "Vector" holography algorithm as the algorithm of choice and comparison

For our applications, this is algorithm of choice not only because of its simplicity and fastest execution time, but also because of the unbeatable quality of the traps produced. The only disadvantage is that it breaks down if the analytical patterns overlap.

A crude experimental comparison is shown in Figure 4.

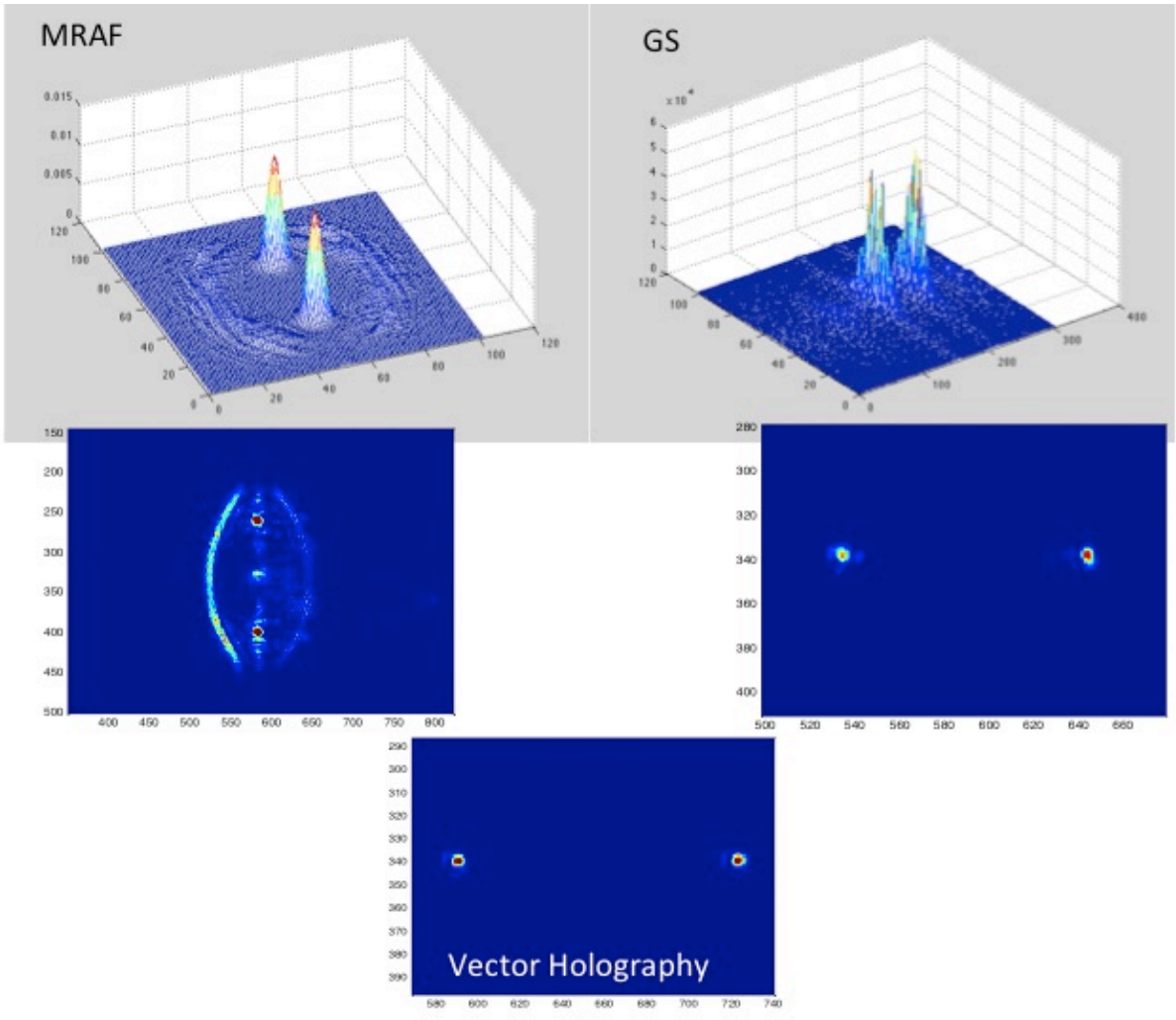

Figure 4. The MRAF algorithm shows better quality of the spots, compared to the GS. However, the canvas region shows relative fluctuations on the order of 5% of the intensity of the spots. The vector holography idea shows much better spots, as seen at the bottom and unbeatable quality of the spots, as long as they do not overlap. The problem of "ghost traps" is still present, which for our purposes is not a big concern, as long as the spots are projected at the two ends of the condensate.

Vector holography is very similar to how a standard computer's graphic processing unit in 2016 functions: it has a toolbox of comparatively simple shapes and a method of arranging them on some arbitrary real space canvas. These particular shapes in our case are any set of so called primitive shapes that can be mathematically produced, or analytical holograms of some sort. As

long as we can describe a real space object analytically, we can arrange it on the canvas, which widens our perspective of possibilities to a variety of patterns, namely LG beams, Gaussians, lines, circles and others. Arranging them with the SLM on different positions in space provides flexibility of arranging them even further with optical elements. This is a huge advantage to alignment, where alignment of the beams can be done with the click of a button (restricted within a region of course). Such examples are (f here is the focus length of the imaging lens, used to project the pattern on the condensate):

1. Gaussian spot of waist w_0, $\varphi_0 = 0$.

2. Line of width w_0 and height $\frac{2\lambda f^2}{F\pi w_0}$, $\varphi_0 = -\frac{ky^2}{2F}$ where y is the vertical direction defined on the shorter side of the SLM. (F here denotes the focal point of the pattern on the image plane, f is the frequency of the light used.)

3. Circle of radius R, $\varphi_0 = -\frac{kR}{f}r$, where r is the radial coordinate.

In our application, we are concerned with the first and simplest way, the Gaussian trap. Moreover, the speed of this algorithmic process is unmatched to other algorithms, in reference to the purposes of implementation of interest. In order to create two of them, we had to shift the position of the second spot, which in this case is simply an offset to a plane.

Adding a phase gradient on the SLM plane will shift the position of the diffracted pattern in the trapping plane. Gratings and lenses in general are often used to steer the light patterns on the image plane three-dimensionally. Altering the grading period leads to a lateral shift of the pattern, while changing the focal length of Fresnel lens causes axial shifts. The interesting thing about this is that this focus shift can be applied to any algorithm of any sort for producing any pattern on any SLM within unprecedented precision.

In order to composite the shapes together, we use the concept of phase dominance in the Fourier transform, described in [12-15]. Phase dominance generally refers to the loss of spectral phase

information of an image that leads to a less recognizable image compared to the loss of amplitude information. The implication is that the spectral phase carries more information than does the spectral amplitude, just like in graphics processing. That can be easily seen when replacing the Fourier amplitude or phase with that from another image.

Here is a clear example. If we take the following images (let's call them *A* and *B*)

A B

And then take the Fourier transform of both and create an image by the inverse Fourier transform (what could have appeared in the trapping plane namely) from the phase of the transform of image A and the amplitude of the transform of image B, and then take the inverse Fourier transform's amplitude, the following image is obtained:

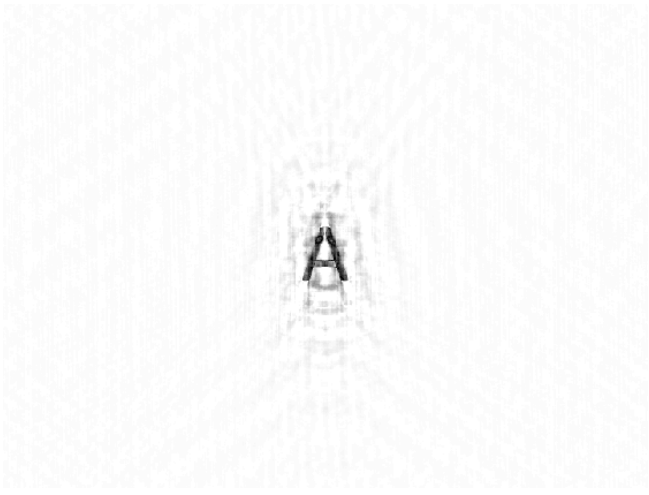

That resembles more the original image A, than B. And even the images overlap! Therefore, the amplitude of the inverse Fourier transform closely resembles the one, from which we took the phase information. This phenomenon has counter examples (mostly

processing unit color-based implementations), but it is very useful in almost all experimental cases in optics. Another explanation for this phenomenon is to compute the mean square error difference compared to the original image, described in detail in [15].

For any individual SLM hologram φ_n the light field at the SLM is $Ge^{i\varphi_n}$, where G is the incident Gaussian light beam. A light field then of shape $G\sum e^{i\varphi_n}$ will produce the desired shape of combined patterns, but since the phase-only Hamamatsu SLM cannot modulate the amplitude, the sum does not equal unity. (There are ideas to modulate both phase and amplitude [28], but the Vector holography idea performs better in terms of RMS error for our particular implementation demand.) Instead, to composite the n different shapes we simply apply the phase

$$\alpha = arg\left(\sum_{m=1}^{n} A_m e^{i\varphi_n + i\theta_m} + 2\pi v \cdot r - \frac{kr^2}{2F_m}\right)$$

Here the set of $\{A_m\}$ parameters controls the tunable relative intensity between individual shaped and the set of $\{\theta_m\}$ can be used to reduce the crosstalk between different shapes. There have been problems with the $\frac{kr^2}{2F_m}$ notion, since the shift focus is strongly dependent on the individual setup, discussed later. However, that is the basic idea of how the algorithm operates.

1.2.5. What do we actually send to the SLM?

$$\varphi_{final} =$$

$$uint8\left(Mod\left\{ \left[arg\left(\sum_{m=1}^{n} A_m e^{i\varphi_n + i\theta_m} + 2\pi v \cdot r - \frac{kr^2}{2F_m} \right) + X * k^x + Y * k^y + \mathrm{Exp}\left(-i\pi \frac{(X - m^x)^2 + (Y - m^y)^2}{\lambda f} \right) \right] * MASK + FACTORY\ CORR. + MODULATED\ WAVEFRONT\ CORR., 2\pi \right\}, [0, 255] \right)$$

That is what the kinoform sent to the SLM looks like. We apply a grating offset $X * k^x + Y * k^y$), needed to easily distinguish between the 0^{th} and 1^{st} order diffraction of the SLM. Note that this shifts the whole pattern with respect to the diffraction order of the SLM. The shift $2\pi v \cdot r$ is a shift related to the relative spacing among patterns. The 0^{th} order has some additional unwanted phase offset, while the first diffraction order is where the target pattern is. Then a lens (as in Fourier optics phase offset) is applied. Typically gratings lead to beam deviations and lenses control the beam convergence. Both are used to steer the trap three dimensionally. All of that is modulated by a mask setting, essentially the pattern is only displayed within a circle, since the incoming Gaussian beam is also such. We have noticed that improves the noise on the target pattern. The factory correction to correct for the surface roughness is applied and so is some wavefront correction (alignment based) since the wavefront hitting the SLM is not flat and there are also distortions due to the optics after the SLM. A wavefront distortion can be detected in a setup, where a test vacuum window is used and the only distortions that can happen will be anything within the vacuum chamber. The pattern is modulated finally as an 8-bit integer, since the SLM is a digital device, acting approximately as an external monitor.

There is a significant difference between what we obtain with the GS algorithm as a kinoform and with vector holography, described in Figure 5.

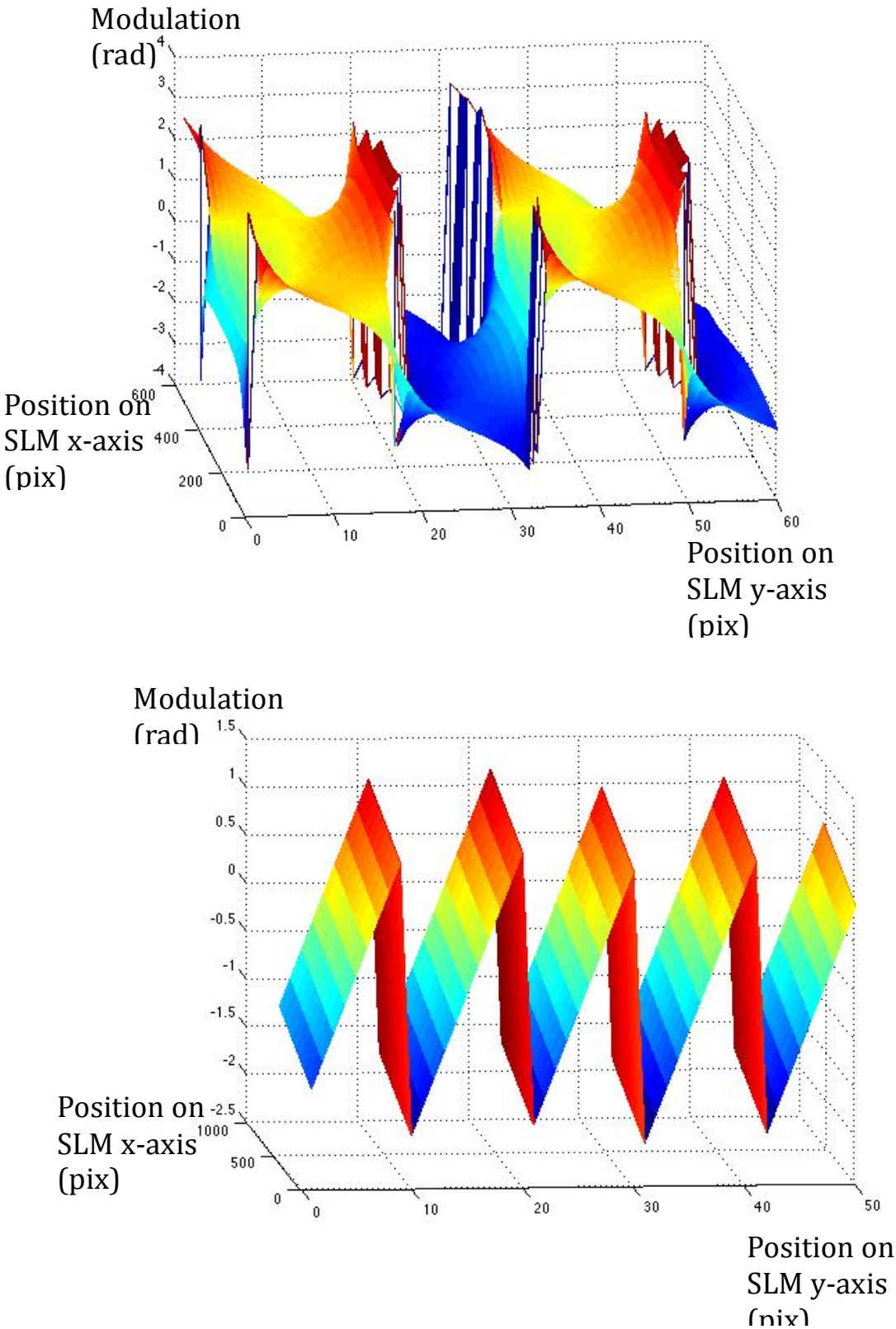

Figure 5. Top: Part of a kinoform from GS algorithm, Bottom: Kinoform from vector holography. The GS algorithm hologram looks very rough, where the vector holography idea looks much cleaner and leads to higher quality Gaussian spots.

1.2.6. Can the GS algorithm be reversely engineered for a pattern of 2 Gaussian beams?

We have also explored the idea of improving the hologram from the GS algorithm by fitting sine functions and offsets to it, in the idea of reverse-engineering the analytic description to figure out if we can improve by tweaking the kinoform in the GS algorithm. The improvement is not better than the vector holography idea, Figure 6 and 7. So the short answer is yes, but that does not provide us an advantage over vector holography.

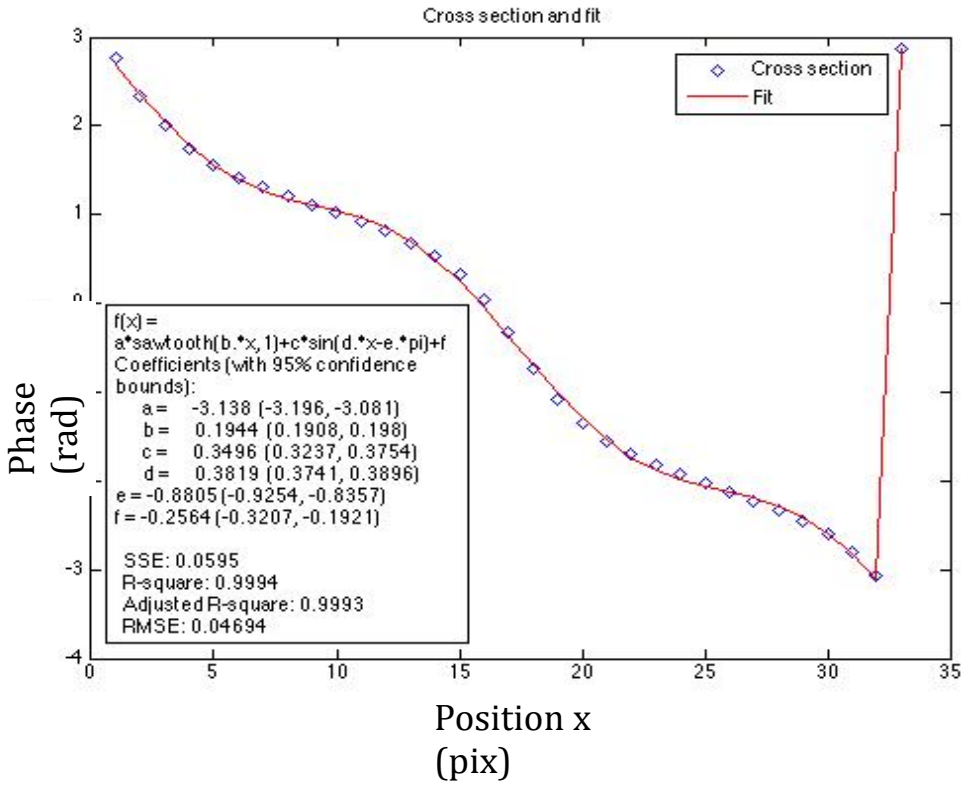

(a)

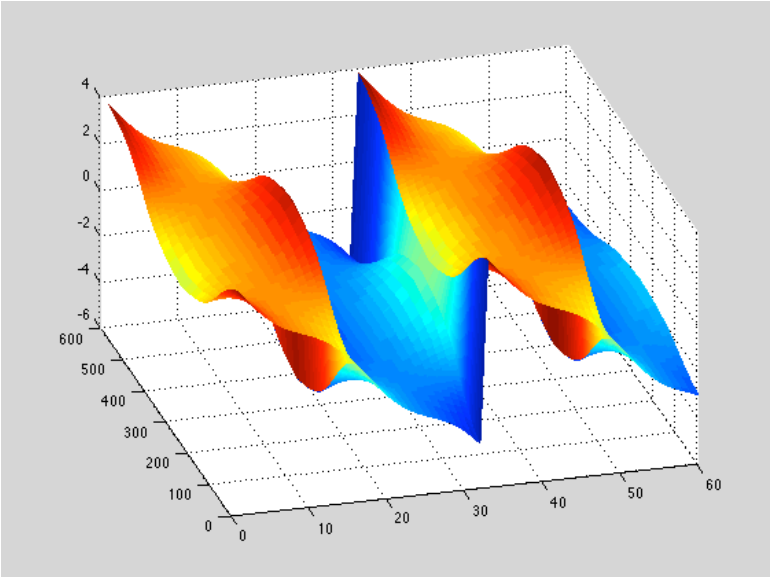

(b)

Figure 6. (a): A fit from sawtooth and sine functions to the kinoform obtained from the GS algorithm. (b):The reproduced smoothed kinoform.

We have also tried to vary different parameters related to that fit in order to see any experimental difference in the quality of spots. No improvement has been observed as seen on Figure 7.

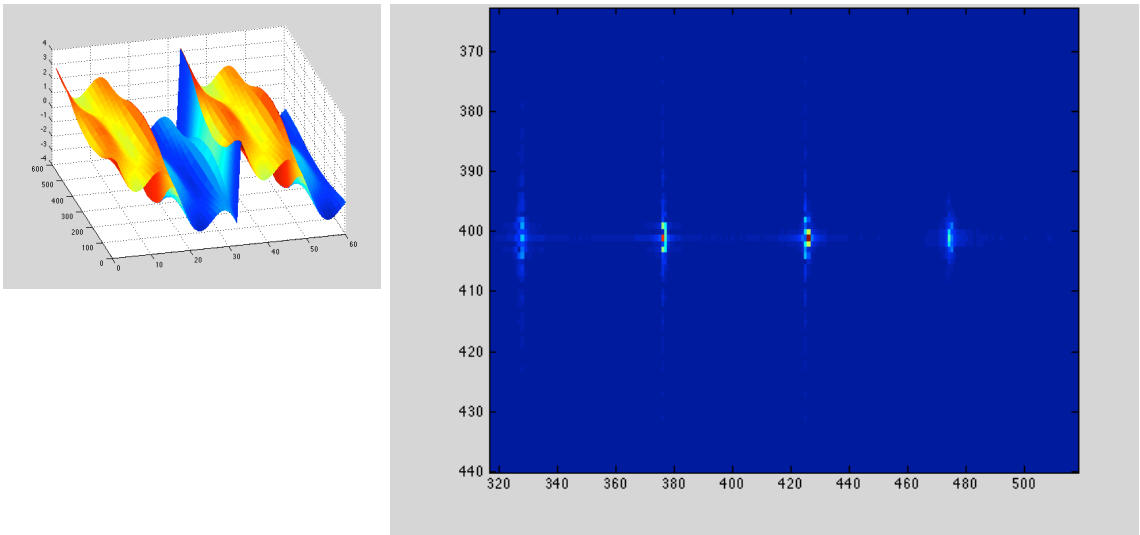

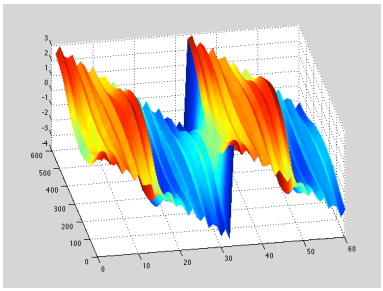

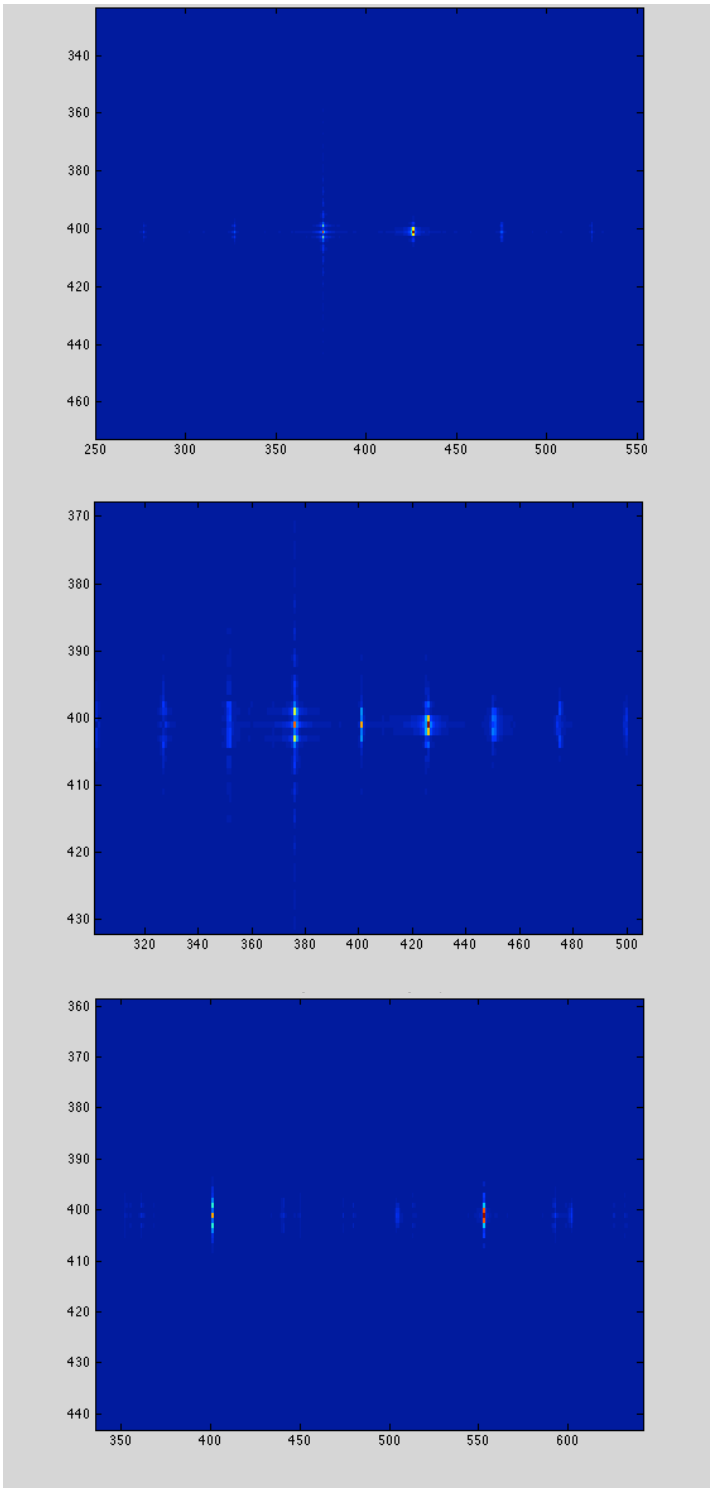
340
360
380
400
420
440
460
250
300
350
400
450
500
550
370
380
390
400
410
420
430
320
340
360
380
400
420
440
460
480
500
360
370
380
390
400
410
420
430
440
350
400
450
500
550
600

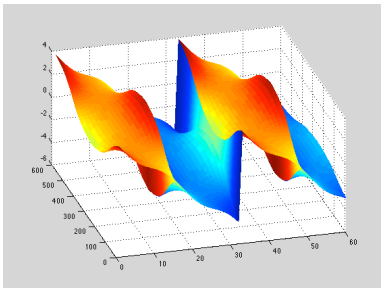

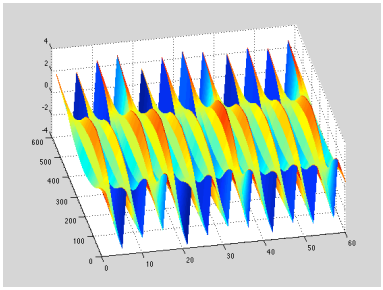

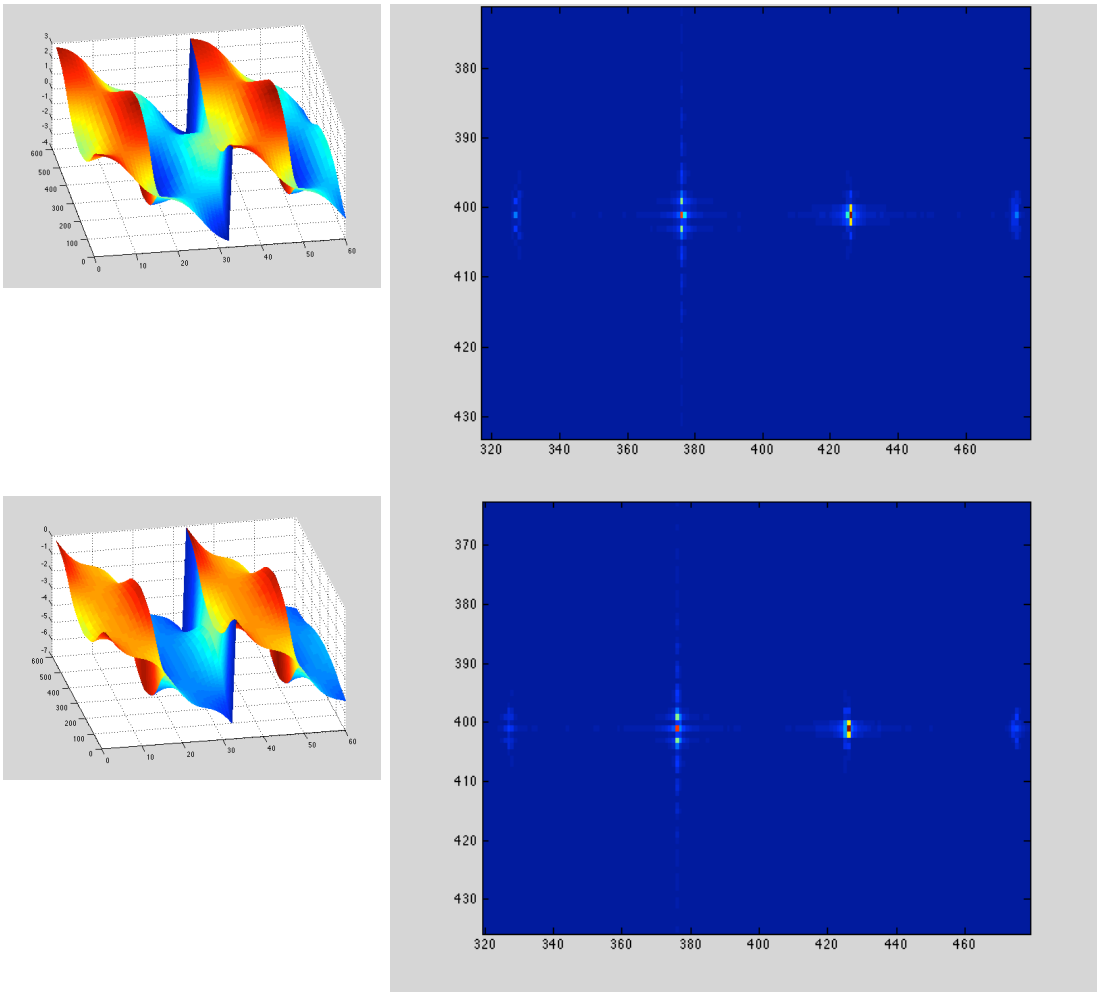

Figure 7. Varying a number of parameters to obtain a different kinoform similar to the GS hologram fit and the results seen. The conclusion is that the outcome is not better quality than the spots obtained with the vector holography idea. The Gaussian beams in the trapping plane actually looked worse than what was initially achieved with the GS algorithm.

1.3. Arising problems when composing patterns on any Spatial Light Modulator

1.3.1. Ghost traps

These are spurious shapes that resemble the desired trap but are severely distorted and placed somewhere else on the canvas (aliased), the magnitude of which increases with increasing symmetry of the kinoform. That is typically less than 2% of the intensity of the desired trap. That is a side effect of disregarding the amplitude in the computations and also the Fourier components of the discrete square pixels on the SLM, diverting light away from the desired potential. That reason is that the sum of exponential functions will have non-uniform amplitude. One way to reduce the amplitude of "ghost" traps is to multiply each grating term with an arbitrary amplitude pattern. Another method [29] is spatial multiplexing, where every hologram is displayed on a portion of the available pixels. Each fraction of pixels is then spread on the SLM randomly. However, with this method the diffraction efficiency decreases faster with increasing number of spots, as compared to vector holography or GS.

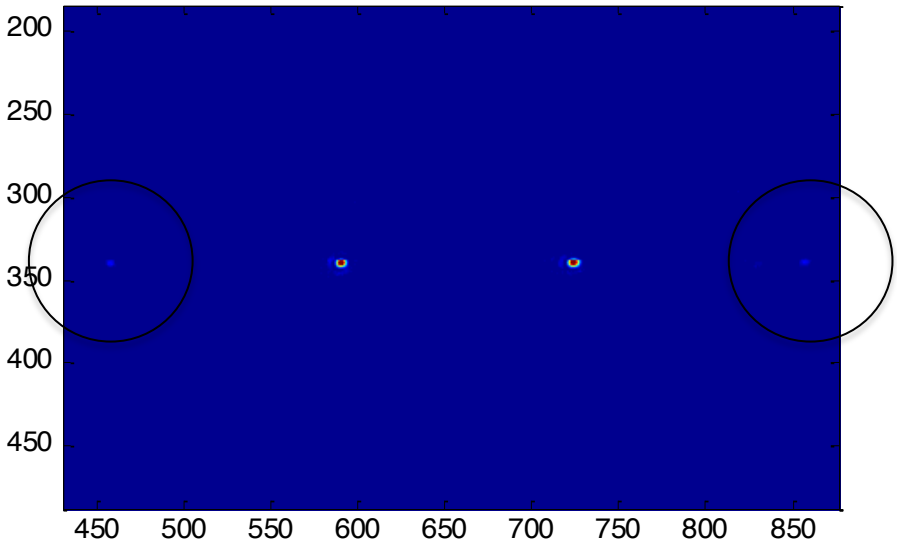

Figure 8. "Ghost" traps, as seen from the GS algorithm for producing two Gaussian beams. Ghost traps appear in every algorithm.

1.3.2. Surface roughness

The low diffraction efficiency of the SLM (around 33% in our case) causes two problems: a decrease in light intensity of the target intensity pattern and a disturbance, because the residual, non-diffracted light could superpose the so-called “productive” part of the light [30]. In order to avoid this, we superposed the original phase pattern with a blazed grating, which causes spatial separation of the first diffraction order from residual light. In order to separate the two orders before the chamber, we use a magnifying telescope before the imagining lens at the vacuum chamber. The liquid crystal layer absorbs some part of the incident light, which also defines a maximum illumination power (in our case (*Hamamatsu* PAL-SLM) between 3 and 5 Watts). Conditional to the manufacturing process, SLMs may show a slightly curved surface, which mainly introduces astigmatism to a beam reflected from the panel [16]. We are therefore utilizing a correction pattern to compensate for the roughness, shown in Figure 9.

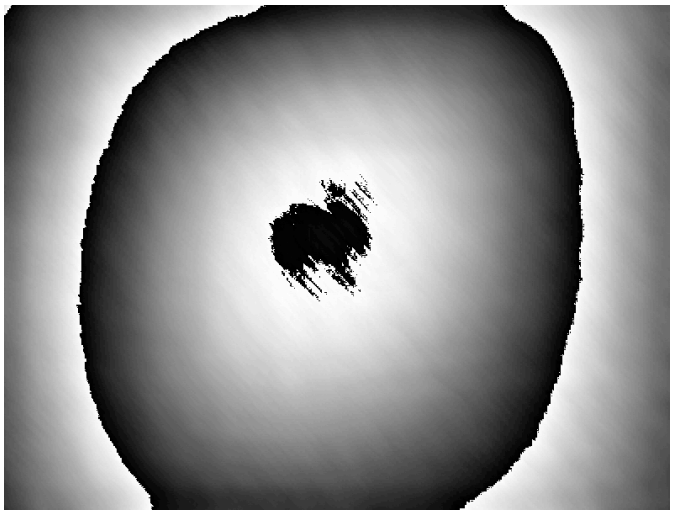

Figure 9. Factory compensation for surface roughness, the correction is in fact only applicable for laser light with wavelength of 1083nm

1.3.3. Relative phase fluctuations between Gaussian traps on the image plane

Also, the light diffracted from the phase patterns displayed on LC SLMs tends to show an oscillation in amplitude and phase, which may originate from relaxation movements of the LC crystals. We have examined what the dynamical phase oscillations for our needs are, that is when projecting a target pattern of two Gaussian traps. Then, by moving the lens out of focus and letting the spots interfere on the camera objective, we looked for slow movements of the fringe pattern and reduced visibility (Figure 10). The visibility result obtained for 48 hour measurements on average was between 0.86 and 0.91 (Figure 11), which would translate to a dynamical relative phase noise between the spots of around $2\pi/45$ (assuming uniform distribution of the relative phase fluctuations between 0 and the value obtained ($2\pi/45$). The way we calculated that is looking at what effect does a relative phase noise between the sources does have on the fringe visibility of a double slit interference experiment).

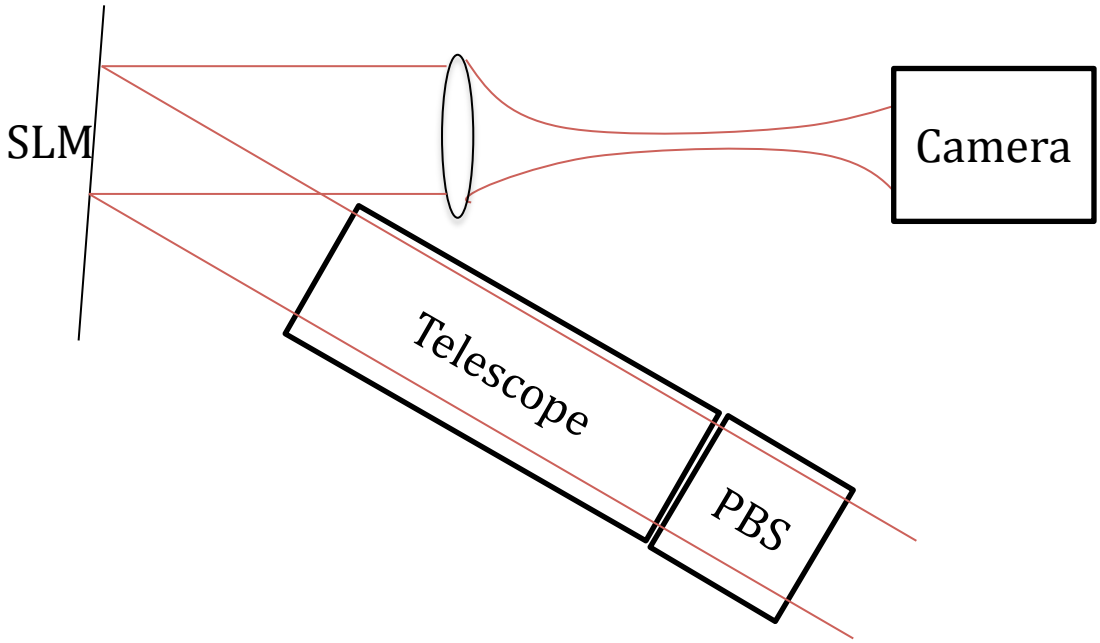

Figure 10. Setup used to obtain a dynamical phase instability measurement. The camera is moved off focus, such that the two Gaussian spots are allowed to interfere. PBS is polarizing beam splitter.

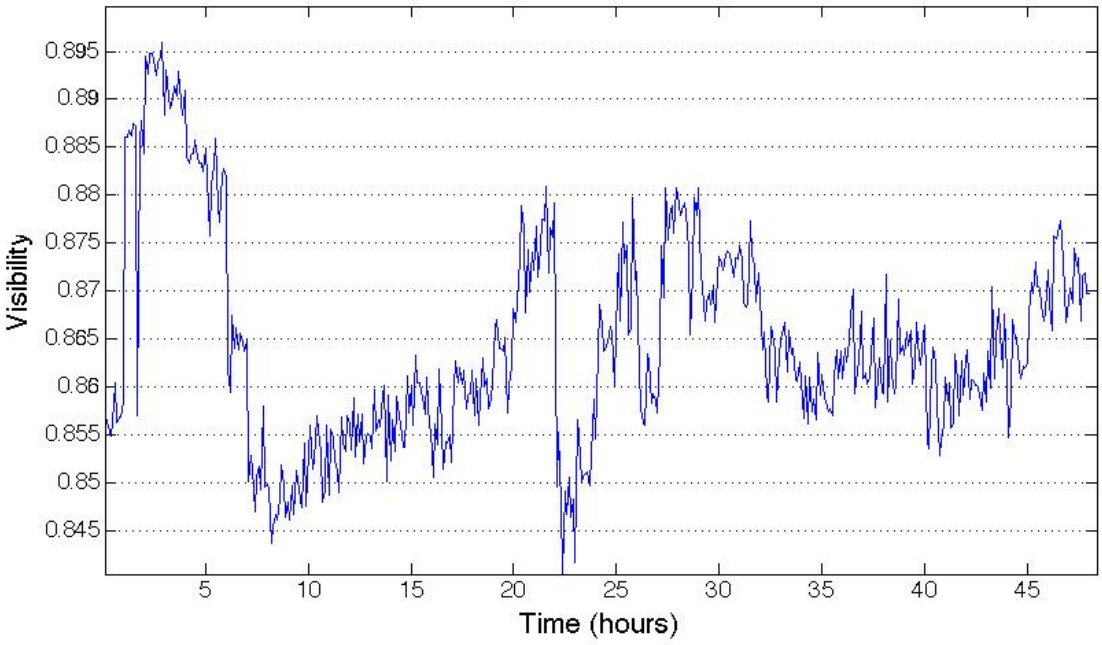

Figure 11. Visibility of the fringe pattern measured for 48 hours. The average is 0.86.

One method to analyze this is to look at the standard double slit interference experiment, which describes what is occurring (two Gaussian modes propagating in free space from two sources). Such situation is thoroughly described in [17].

The case to consider is interference with quasi-monochromatic light. The intensity of a point on the screen in the interference pattern can be written as

$$I(r) = I_1(r) + I_2(r) + 2\sqrt{I_1(r)}\sqrt{I_2(r)}|\gamma_{12}(\tau)|Cos[\alpha_{12}(\tau) - \delta]$$

where $\tau = \frac{s_2 - s_1}{c}$ and $\delta = \frac{2\pi}{\lambda}(s_2 - s_1)$, and the "s" parameters signify the distance from source to screen. $\gamma_{12}(\tau)$ is the degree of coherence. The intensity minima and maxima to a good approximation obey

$$I_{max} = I^1(r) + I^2(r) + 2\sqrt{I^1(r)}\sqrt{I^2(r)}|\gamma_{12}(\tau)|$$
$$I_{min} = I^1(r) + I^2(r) - 2\sqrt{I^1(r)}\sqrt{I^2(r)}|\gamma_{12}(\tau)|$$

One can therefore rewrite the fringe visibility as

$$V(r) = \frac{2\sqrt{I^1(r)}\sqrt{I^2(r)}}{I^1(r) + I^2(r)} |\gamma_{12}(\tau)|$$

Upon equal intensities, the visibility of the fringes is then equal to the degree of coherence. The degree of coherence has a relation to the mutual coherence function in the following way

$$\gamma_{12} = \frac{\Gamma_{12}}{\sqrt{I^1}\sqrt{I^2}} = \frac{\langle V_1 V_2 \rangle}{\sqrt{I^1}\sqrt{I^2}}$$

where the field description for "V" is used.

One can therefore think of the simple case where we have two fields

$$V_1 = V$$
$$V_2 = Ve^{-i\delta}$$

where the fields have the sample amplitude but a relative phase difference δ.

In order to take the time average of this, we need to be aware of the phase difference distribution. That would lead to an interesting result giving the visibility of the pattern introducing phase fluctuations up to some value for the phase difference.

$$Vis. = |\gamma_{12}(\tau)| = \int_0^x e^{-i\delta} \Pr(\delta) d(\delta)$$
$$= \left[\int_0^x e^{-i\delta} d(\delta) \right]_{for\ uniform\ distr.from\ 0\ to\ x}$$

By solving this for the visibility average obtained for the 48-hour measurement, we see that the visibility fluctuations correlate to a uniformly distributed phase difference of $2\pi/45$.

1.3.4. Pupil conjugation

When projecting the pattern into the vacuum chamber while generating off-axis traps, the beam diffracted by the SLM impinges on the lens off center, giving rise to clipping and field aberrations. We circumvent this problem using pupil conjugation (using the same telescope used to separate the first and zeorth diffraction order). The idea is described in figure 12.

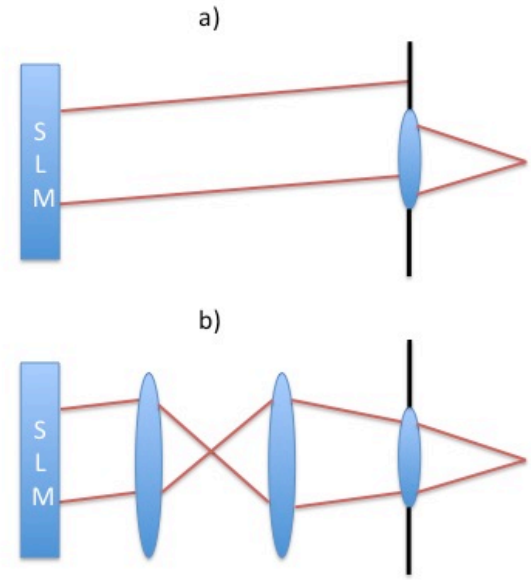

Figure 12. a) without the telescope, for a given field the beam is clipped and not centered on the imaging lens. b) the implemented in the setup telescope adjusts the size of the beam to the size of the pupil of the imaging lens by conjugating the SLM aperture to the entrance pupil, whatever the field. It is also used for removing the zeroth diffraction order by placing a knife-edge at the focus point of the telescope.

1.3.5. Wavefront estimation and correction

The wavefront impinging on the SLM and after the SLM on the atoms is not flat. The absolute and relative trap depth is then decreased [18] whatever the algorithm. The quality of the spots is

also significantly reduced if no wavefront correction is applied. We can however correct for the relative trap depth algorithmically, but in order to correct for the absolute trap depth imperfection, we may need to buy a wavefront sensor provided we have some form of closed loop feedback that measures the wavefront on the fly. The relative trap depth imperfections would arise from a distorted wavefront impinging on the atoms. Measuring the wavefront of the beams at the position of the atoms is a cumbersome task, since we don't have the option to place a sensor at that position. However, we can place one immediately before the entrance window of the chamber and correct the distortions up to that point. The correction patterns we utilize are based on measuring the wavefront after a test vacuum chamber window.

In general, the wavefront distortions can be decomposed into Zernike distortions, Zernike polynomials, which span the space of distortions over a circular region. By introducing the negative of the normalized estimate of polynomials on the phase space, one can control the wavefront within the limitations of the sensor. We have several methods to achieve this. One, we have built our own Wavefront sensor (30x30 microlenses), which operates like all other wavefront sensors and developed an algorithm to compute the initial distorted wavefront and afterwards apply a correction. These types of sensors need great precision when assembled, which is why we also tested several other sensors, which have much better resolution.

The basic idea is to measure the spots displacements from the lenslet array, once we calibrated it with a relatively large Gaussian beam (6 times the size of the SLM), approximating a flat wavefront, and intensities, which then algorithmically we can decompose into Zernike moments in order to describe the wavefront distortions.

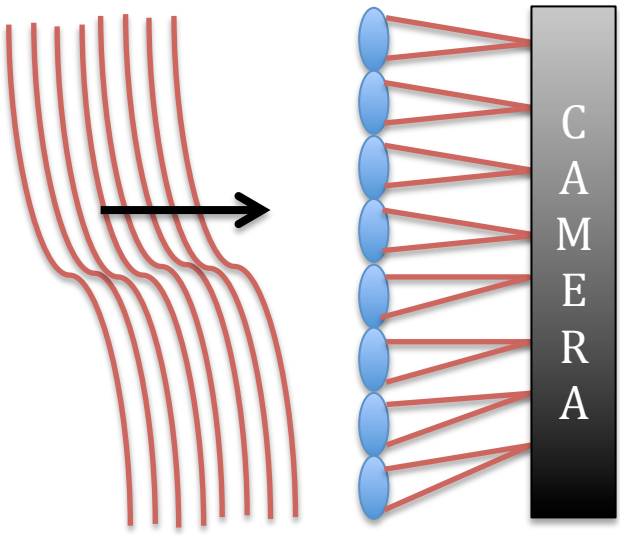

Figure 13. The basic structure of a wavefront sensor, composed of a lenslet array and a CCD camera

The selected sensors are of Shack-Hartmann type. That consists typically of a lenslet array and a camera. When a wavefront hits the lenslet array, a spot field is created on the camera surface, where each spot is analyzed in terms of location and intensity. That can be also dynamically measured providing the technology for adaptive-optics techniques based on the refresh rate of the camera in place. The sensors must be calibrated with a beam of an extremely flat wavefront in order to record the original positions of the spots produced by the lenslet array within high precision.

We were able to build our own wavefront sensor and estimate the wavefront of the beam reflected off the SLM by finding the locations of the focal spots, produced by a lens array programmatically (Figure 14 and 15). We were then able to produce a correction pattern, taking the inverse of the wavefront and compare the quality of light pattern on the image plane of the SLM with some commercial wavefront sensors. The commercial sensors showed larger improvement of the quality of light patterns compared to our home-built sensor. Then I show what results can be obtained with a single iteration feedback loop of wavefront correction of various commercial sensors. In the end, we apply two feedback loops to get the best quality of wavefront improvement.

a

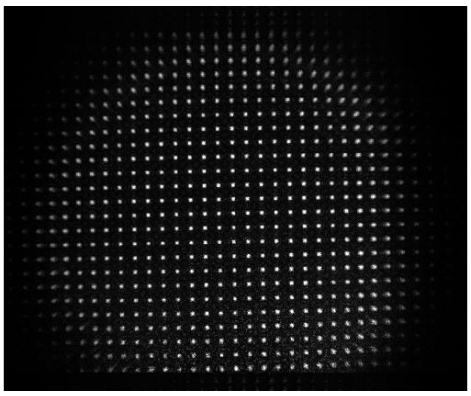

b

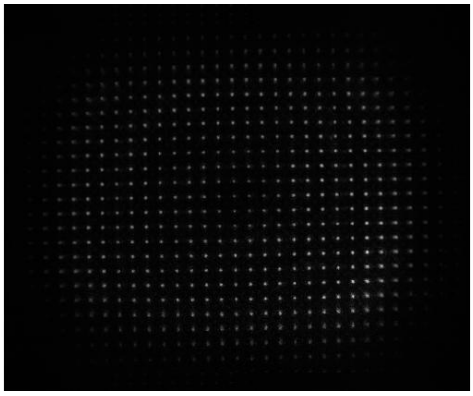

c

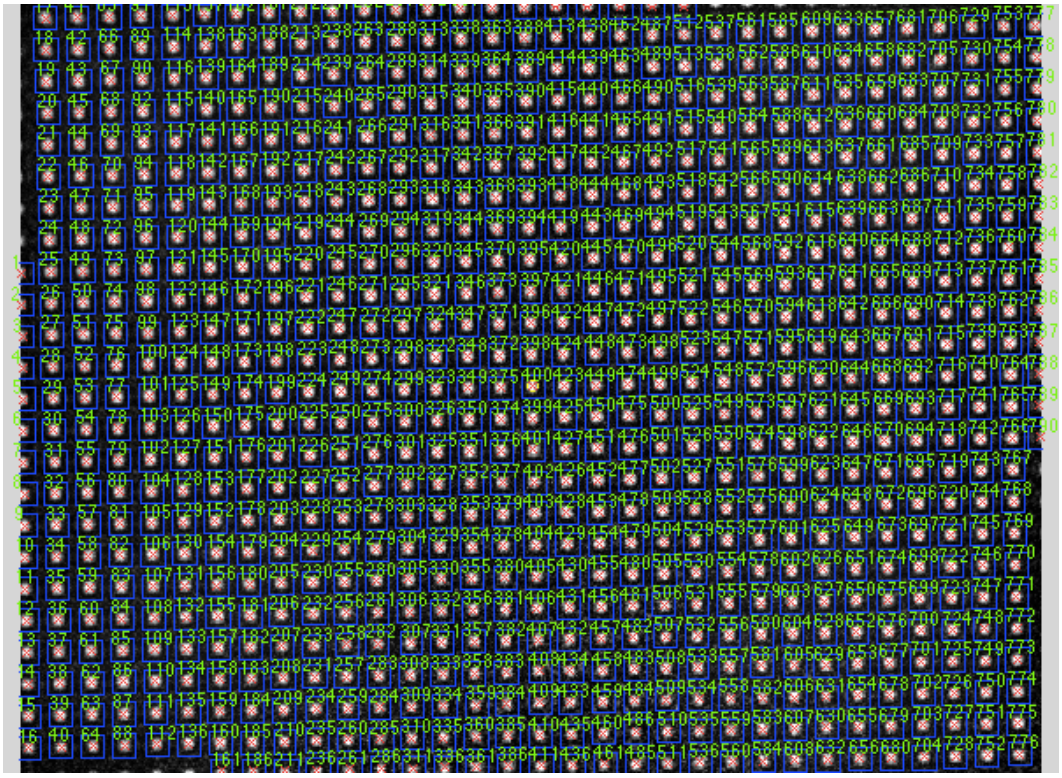

Figure 14. a) the spots obtained from a Gaussian beam 6 times the size of the SLM. b) the spots obtained from the SLM beam c) the relative dislocations of the focal spots produced by the lens array with respect to the large Gaussian reference beam are found algorithmically

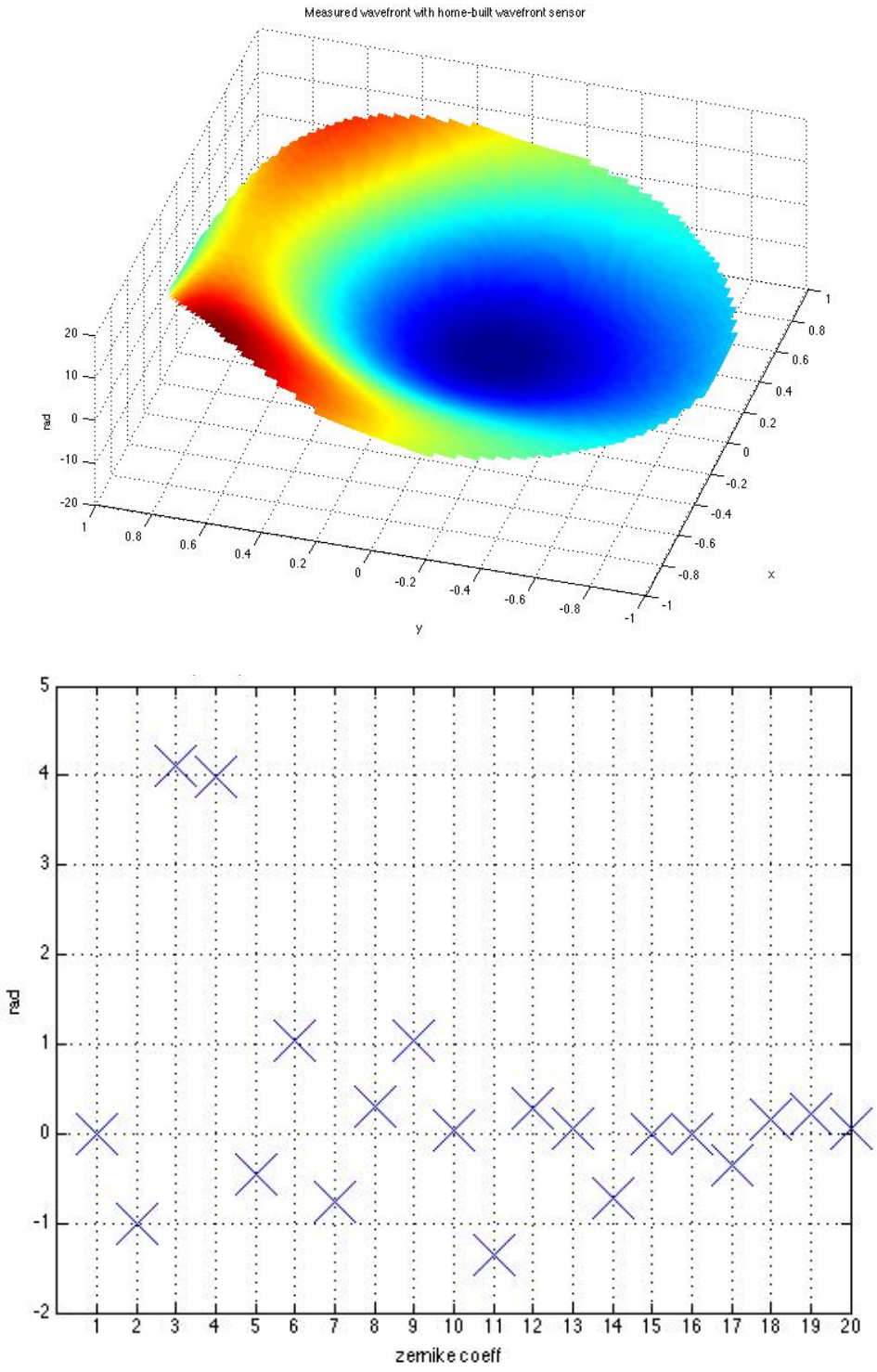

Figure 15. Top: Measured wavefront with home-built sensor. Bottom: Zernike decomposition of that wavefront

For the purpose of improving the quality of correction, we also tested the ability to correct the wavefront with three types of commercially available sensors: SHSLab HR-150-GE-PRO (55x44 microlenses and 8.98x6.71 mm sq. detection area) available from Optocraft, HASO 3 128 GE2 (4.9x6.1 mm sq. detection area and 32 x 49 microlenses) and HASO128 GE2 (128 x 128 microlenses and 15x15 mm sq. detection area) available from Acal Bfi. Our conclusion is that the Optocraft sensor behaves most appropriately at the given price and would be our wavefront sensor of choice.

The results after correcting for the wavefront with those devices can be summarized as follows:

Optocraft

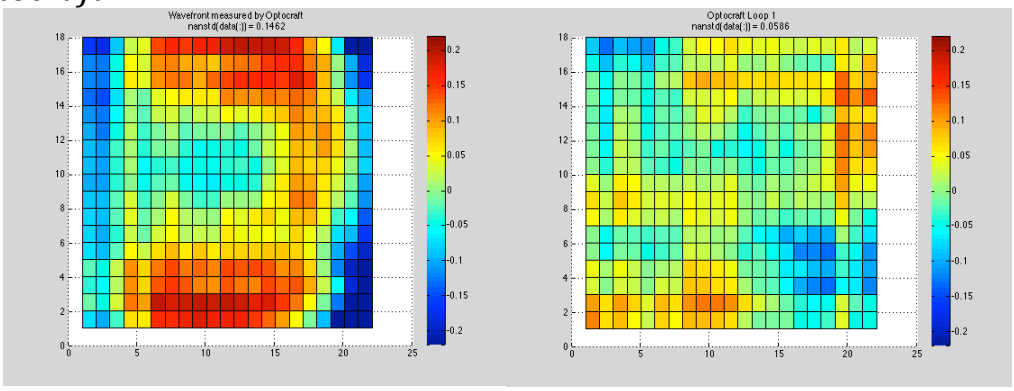

Measured Wavefront (left), Corrected wavefront after a single feedback loop (right)

HASO 32

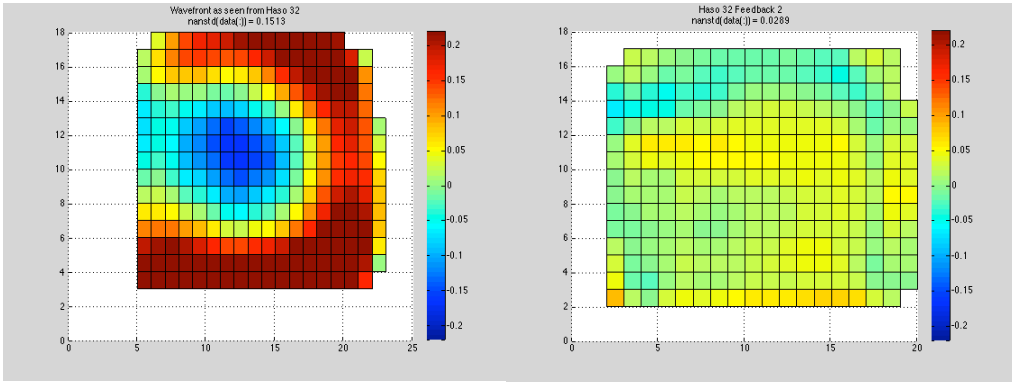

Measured Wavefront (left), Corrected wavefront after single feedback loop (right)

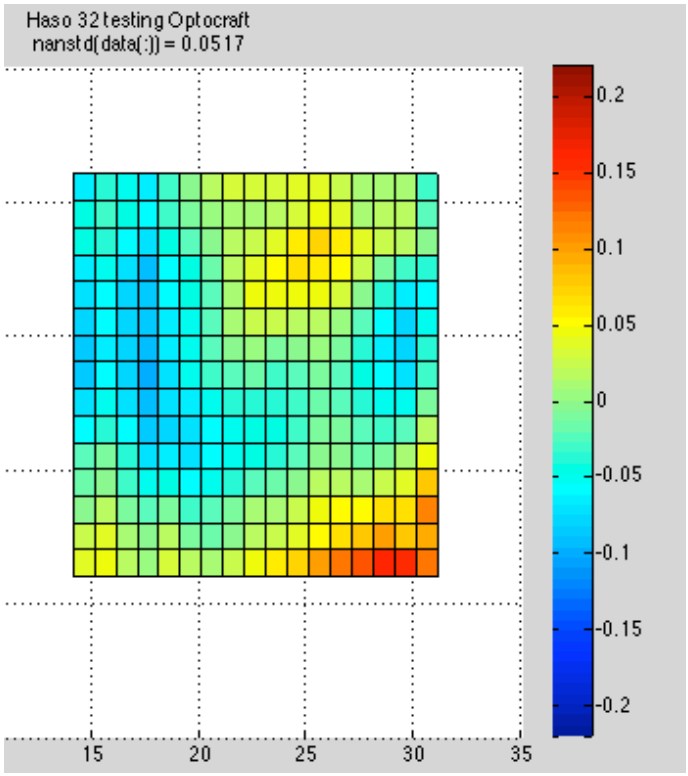

Looking at wavefront with the HASO 32 with the Optocraft correction applied

HASO 128

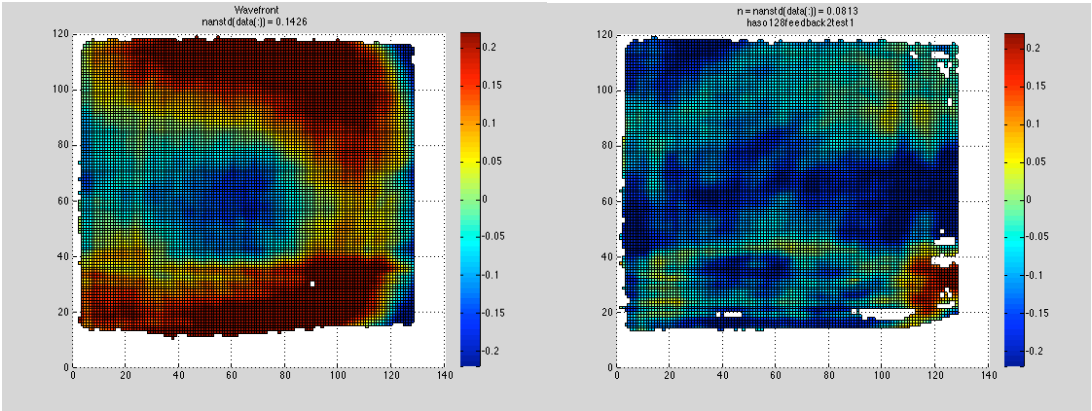

Measured Wavefront (left), Corrected wavefront after single feedback loop (right)

Figure 16. Measured wavefront with commercial sensors and measurement after a correction is applied.

In conclusion, we can control the wavefront to 0.5% of the wavelength (1083 nm in this case) in units of wavelength with two feedback correction loops. That improved on the quality, obtained from applying a single feedback iteration loop. In order to achieve

such a good quality, we take another measurement of the wavefront after a single feedback is applied and apply a new correction. That showed improvement in the wavefront, making the standard deviation from 5.1% down to 0.5% in units of wavelength.

1.3.6. Controlling the focal length of individual spots or patterns

Controlling the focal length of independent patterns on the image plane is not trivial. That depends on the present SLM setup, where each optical element contributes to some aberration. We have, however, devised an algorithm to accompany that and control the focus point of each spot with great precision (a tenth of a millimeter resolution measured via a translation stage).

One can see how this is done with ABCD matrices (or Ray-transfer matrix methodology). Applying a lens operation on the SLM is similar to adding a lens on the surface of the SLM. Simply put, the setup after the SLM would have the following configuration (Figure 17).

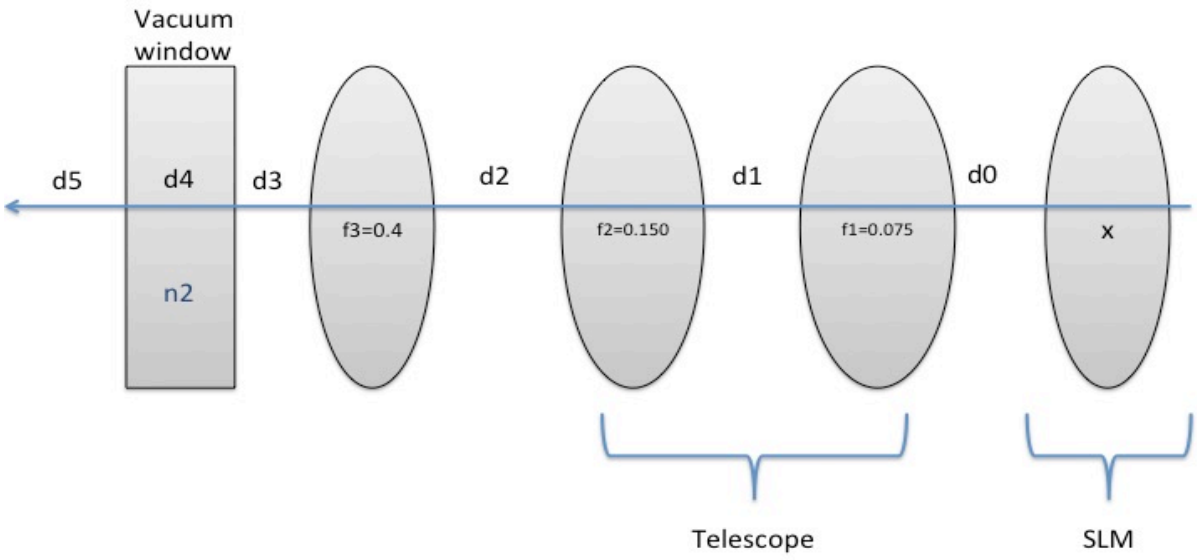

Figure 17. The setup of lenses after the SLM. Focal lengths are in meters.

Essentially an optical element can be described as matrix operation acting on the incoming field to produce an outgoing field. This is a standard approach of ray transfer matrices. Where the *y*-s signifiy distance from the optical axis and thetas the angle from the optical axis.

$$\begin{matrix} y_{out} \\ \theta_{out} \end{matrix} = \begin{pmatrix} A & C \\ B & D \end{pmatrix} \begin{matrix} y_{in} \\ \theta_{in} \end{matrix} = M \begin{matrix} y_{in} \\ \theta_{in} \end{matrix}$$

Where in this case

$$M = \begin{pmatrix} 1 & d_3 \\ 0 & 1 \end{pmatrix} \begin{pmatrix} 1 & 0 \\ -\frac{1}{f_3} & 1 \end{pmatrix} \begin{pmatrix} 1 & d_2 \\ 0 & 1 \end{pmatrix} \begin{pmatrix} 1 & 0 \\ -\frac{1}{f_2} & 1 \end{pmatrix} \begin{pmatrix} 1 & d_1 \\ 0 & 1 \end{pmatrix} \begin{pmatrix} 1 & 0 \\ -\frac{1}{f_1} & 1 \end{pmatrix} \begin{pmatrix} 1 & d_0 \\ 0 & 1 \end{pmatrix} \begin{pmatrix} 1 & 0 \\ -1/x & 1 \end{pmatrix}$$

$$f_2 = 0.150m, f_1 = 0.075m, d_1 = 0.225m$$

The boundary conditions would have to be set such that $y_{out} = 0 = Ay_{in} + C\theta_{in}$, the spots are on focus. θ_{in} can be set to a small value close to 0, while θ_{out} can have a small value close to zero, due to alignment imperfections for example.

For the parameters for lenses and vacuum window used (index of refraction of the window is 1.51 from datasheet) we obtain the following model:

$$d_5 = -\frac{0.00175}{0.0386 - 0.571x[m]}\ [m]$$

where “x” is the focus length of the lens that is imprinted on the SLM. This is a very nice model, because upon every change in the actual setup, we can feed in the new parameters and obtain a new model that will describe the situation correctly.

The data measured for the focus point change looks like the following

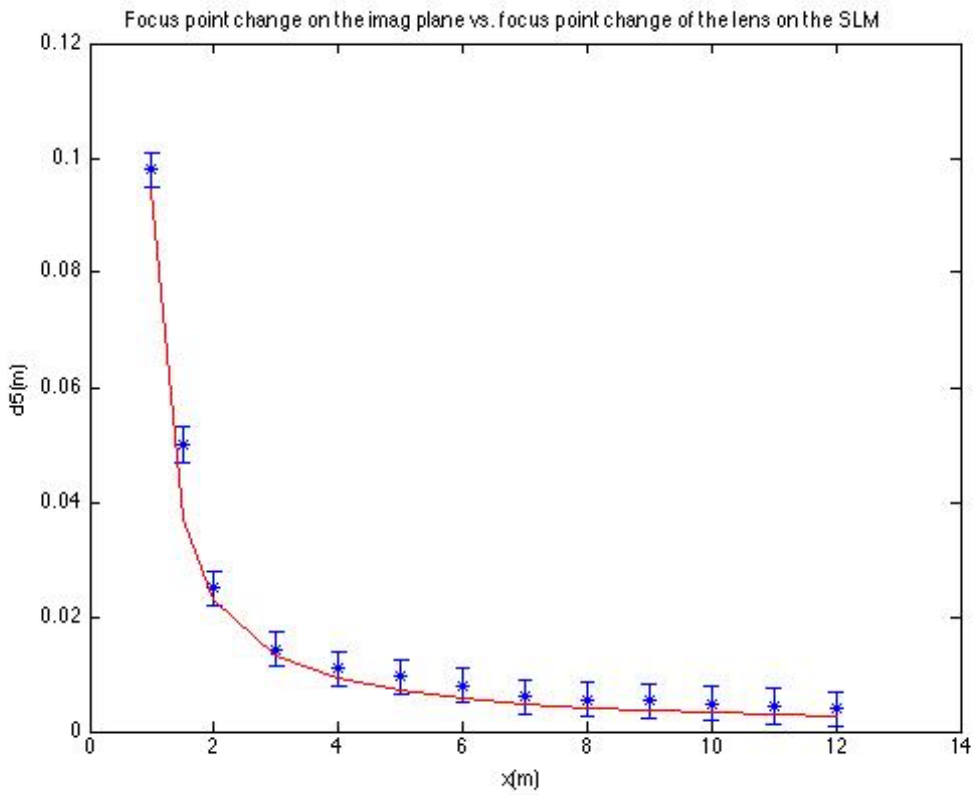

Figure 18. The distance d_5 to the focal plane of the imaging lens versus the focal length of the lens coded on the SLM and corresponding equation.

There is another problem related to this section. If we change the focus point of the trapping plane, the relative distance between the traps also changes. We can overcome this problem again with ABCD matrices.

1.3.7. Controlling the relative distance between spots on a different focal plane

That is related to the change of the final angle θ_{out}. However, this has to be normalized with respect to the angle, when the focal length of the lens imposed on the SLM is infinity. Clearly $\theta_{out} = By_{in} + D\theta_{in}$. Therefore, for the parameters that we have, the model obtained is

$$\frac{\theta_{out}}{\theta_{out,\ x\to\infty}} \sim Relative\ distance =$$
$$= -Const * \frac{0.0571x}{0.0386 - 0.571x[m]}\ [\mu m]$$

The final angle change is proportional to the change in relative distance between the traps. That agrees very well with the data (we measured the dataset by fitting two Gaussians to the data obtained with the camera and calculating the relative distance between the fits, and obtained the constant of proportionality is 100 from a fit) (Figure 19).

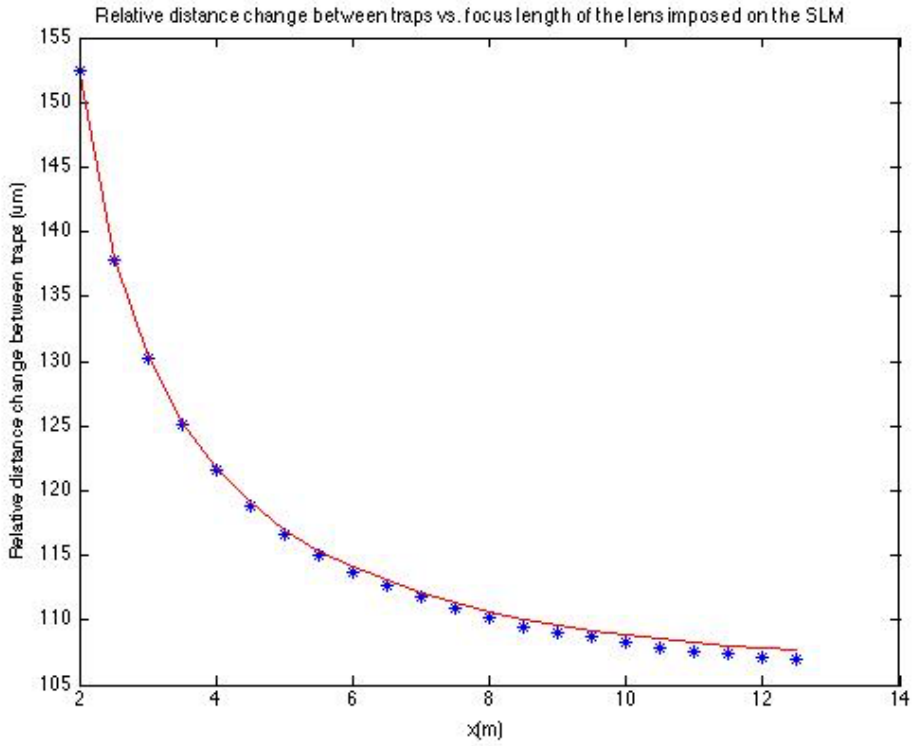

Figure 19. The relative distance between Gaussian spots in um with respect to the focal length of the lens, encoded on the SLM. The corresponding equation and data agree very well within 2 um.

Therefore, we can control very well the focal point of each individual pattern and relative distance between patterns within 2 micrometers; project analytic patterns on the trapping plane and shuffle them around easily. The way that we measured the relative distance is by taking the data of the two spots and fitting two

Gaussian functions on a cross section at the middle of the spots and taking the distance between the centers of the Gaussians.

1.3.8. The problem of optical vortices

Optical vortices are topological features of the light field that are related to a phase winding around a point of zero intensity. Also known as phase singularities or branch points [19]. Unwinding a vortex would require global change of the hologram, which is difficult to achieve in the later stages of any algorithm. The reason for the imperfections in the MRAF algorithm for example in the extended canvas regime is the formation of large populations of vortices during the early iterations of the algorithm.

Once the hologram becomes more complicated, it is no longer analytical. The problem then arises from a steep change in the phase from 0 to close to 2π, which is why the offset was added in the OMRAF algorithm. That however, does not remove the vortices completely [10]. The vortices occur mainly because the hologram that we are projecting on the SLM with the OMRAF, MRAF or GS algorithms becomes non-analytical. With the "vector" holography algorithm, we only control the diffraction-limited position and focal length of the holograms but not their size. Another method one can exploit is to design an Adaptive Optics system, featuring a Shack-Hartmann sensor to inverse the phase of the measured beam onto the SLM in order to correct for distortions.

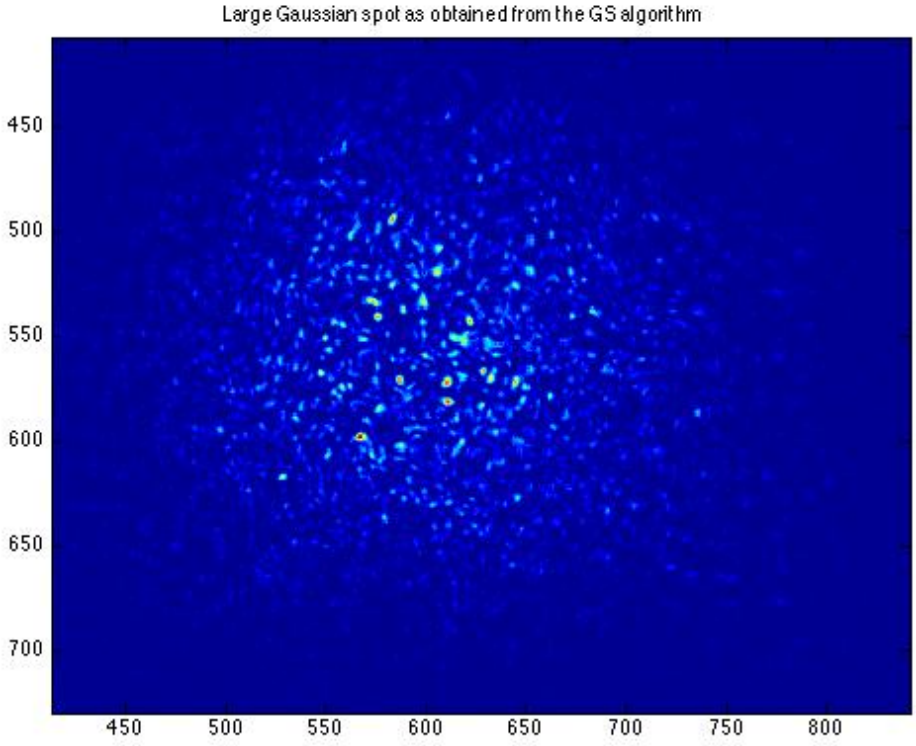

Figure 20. An example of optical vortices by attempting to obtain a large Gaussian spot (500 times the diffraction limit) with the GS algorithm

1.3.9. Polarization fluctuation in the setup

We measured the varying power of a single Gaussian beam, created with the SLM right after a polarizing beam splitter. The result (shows a standard deviation of about 6.2uW or 0.31% fluctuation of the power after the polarizer over a 6-hour measurement. Therefore, any polarization fluctuations induced by the SLM are insignificant (Figure 21).

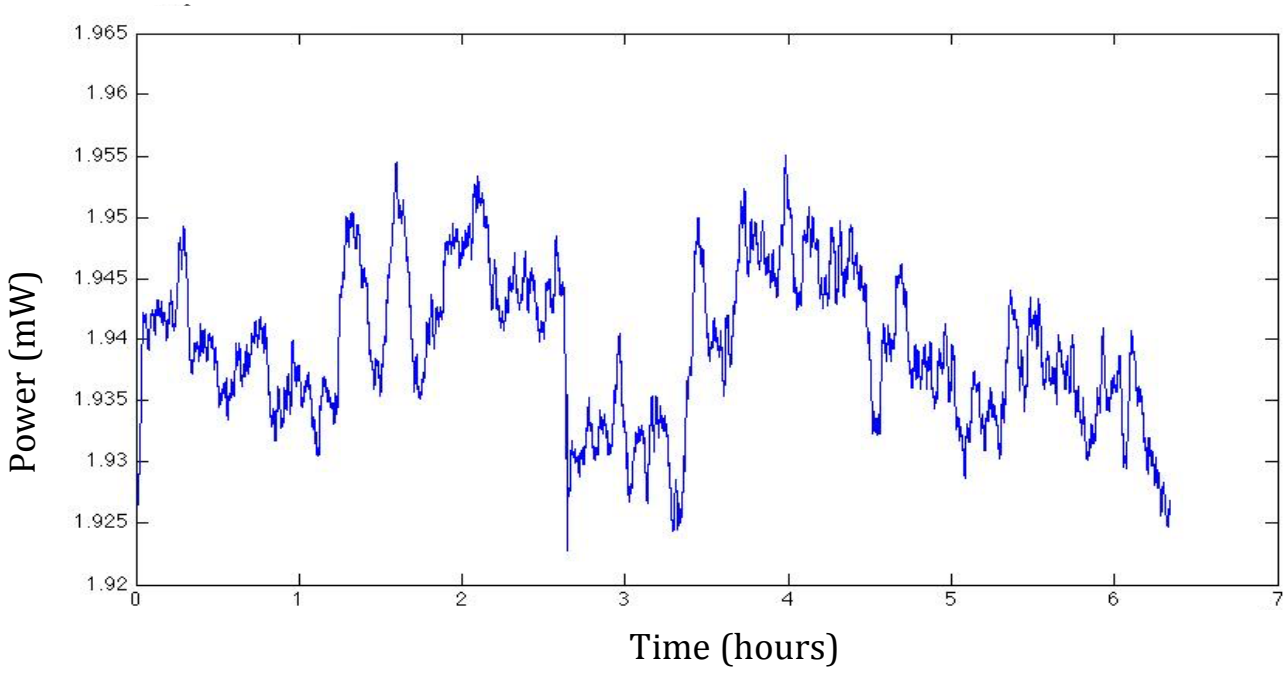

Figure 21. Power measured after the SLM and a polarizing beam splitter.

2. The experiment devised to demonstrate momentum entanglement

2.1. Discussion of the experiment

Interference plays a significant role in fundamental physics. At the quantum level, interference is a witness of quantum superposition. Interference of entangled particles is of main significance to the study of nonlocal correlations of spatially separated entangled particles [21]. Quantum interference of momentum-entangled photons has been studied in various experiments such as double double slit and ghost interference experiments [22-24]. Via a light pulse atoms can be given precise momentum recoil and can also be put in a superposition of opposite momenta. Additionally, the recoiled atoms can be simultaneously out-coupled from the trap to a magnetically insensitive state. The atoms having opposite momenta collide with each other and are scattered spherically. Moreover, we can detect

entangled atom pairs in a four-quadrant delay line detector (micro-channel plate type) with the four quadrants running independently with high time resolution. In the detection scheme, a fixed detector can detect one atom from a pair and the probability of finding the other one measured at different locations corresponds to a conditional interference pattern only if there are multiple sources of origin.

Consider a BEC trapped in a double well potential (Figure 22) with a well separation d. Bragg diffraction is realized with two σ polarized laser beams propagating in the opposite direction along the x-axis and a π polarized beam propagating on the y axis [25]. There is a finite probability that the atoms will collide with opposite momentum along the x − direction, scattering thereafter in all directions isotropically. After that, a detector D_1 at P_1 detects one atom. The second atom of the same pair is detected by the detector D_2. For a momentum entangled pair the joint probability of detecting the first atom and the second atom exhibits a conditional interference pattern.

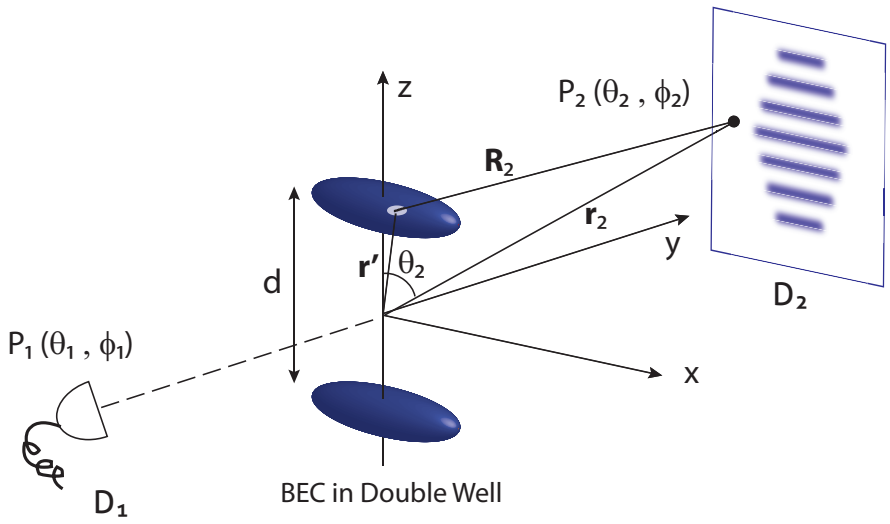

Figure 22. A BEC trapped in a double well potential

The pair creation rate should be small enough such that there is one pair in the detection window and the BEC is dilute enough such that no multiple collisions of individual atoms would occur. In order to find out the probability amplitude of finding two scattered atoms in space, each point in the BEC can be treated as a source of two spherical waves (for each particle from the pair). Similar

approach has been done in [26]. There, the authors showed that for a SPDC source the correlations in forward direction could be obtained by integrating over the source region with spherical waves as Green's functions. The BEC coherence makes it possible to follow the same approach for the case of four-wave mixing, where just the scattering is discussed and not the dynamics.

Weighted by the density of the single particle wave function $\phi(r')$, the wave function in the far field can be written as

$$\psi(R_1, R_2) = \iiint |\phi(r')|^2 \frac{e^{ik_1 R_1}}{R_1} \frac{e^{ik_1 R_2}}{R_2} dx'dy'dz'$$

where $R_j = |r_j - r'|$ and $r_j \gg r'$ in the far field

The Fourier transform of the density profile would then be

$$\psi(k_a, k_b) = \iiint \frac{1}{(2\pi)^{3/2}} |\phi(r')|^2 e^{-i(k_a + k_b)r'} \, dx'dy'dz'$$

Similar approach can be found in the results in [27].

So, using the spherical wave approximation (SWA) can be used to calculate the correlations of two particles scattered from the BEC into an entangled state of two counter-propagating waves. One way to achieve multiple collision zones is having the "slits" as source by splitting the BEC into two parts. The Raman laser beam propagating in the vertical direction can be shaped with the SLM as a double well.

The SLM imprints a pattern of two "slits" with Gaussian shape in a distance d onto the BEC (Figure 23). The source size in the z-direction is given by the Thomas-Fermi radius of the BEC and for reasons of simplicity, the integration of the distribution is calculated as a Gaussian distribution in the other two directions.

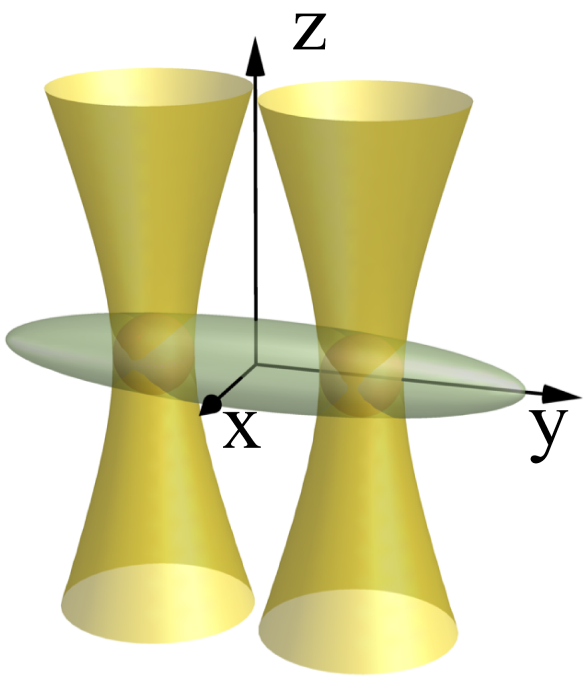

Figure 23. An illustration of two Gaussian beams imprinted on the BEC with the help of the SLM

That would lead to, as discussed in the Thesis of Maximilian Ebner (past member of our group) the following result for $\phi(r')$,

$$|\phi'(x')| = \frac{1}{\sqrt{2\pi}s_x} Exp\left(-\frac{x'^2}{2{s_x}^2}\right)$$

$$|\phi'(z')| = \frac{1}{\sqrt{2\pi}s_z} Exp\left(-\frac{z'^2}{2{s_z}^2}\right)$$

$$|\phi'(y')| = \frac{1}{\sqrt{8\pi}\, s_y}\left\{Exp\left[-\frac{(y' + {}^{d}/_{2})^2}{2\,{s_y}^2}\right] + Exp\left[-\frac{(y' - {}^{d}/_{2})^2}{2\,{s_y}^2}\right]\right\}$$

Further calculations on obtaining the EPR-like entanglement fringes with those density profiles are discussed more in Ebner's thesis. I am making use of $\phi'(y')$ in the next chapter.

2.2. Monte Carlo simulation for varying the amplitude of one of the spots for outcoupling

Here, this integration region is redefined, such as to incorporate different densities of atoms in the two regions where atoms are outcoupled, namely different densities in between sources.

$$|\phi'(y')|^2 = \frac{A}{\sqrt{8\pi}\, s_y}\left\{X\, Exp\left[-\frac{\left(y' + {}^{d}/_{2}\right)^2}{2\, {s_y}^2}\right] + (1-X)Exp\left[-\frac{\left(y' - {}^{d}/_{2}\right)^2}{2\, {s_y}^2}\right]\right\}$$

The only difference is adding a relative density profile with proper normalization constant A. Here is an example of the result obtained from a Monte Carlo simulation where the amplitude of the density of one of the spots in y direction is varying as a Normal distribution of values with mean of 0.5 and standard deviation of $\frac{0.5}{3}$.

Performing the calculation over 1000 runs leads to interesting results. Figure 24 shows what is fed for the amplitude of one of the Gaussian spots density, a Gaussian distribution varying between 0 and 1.

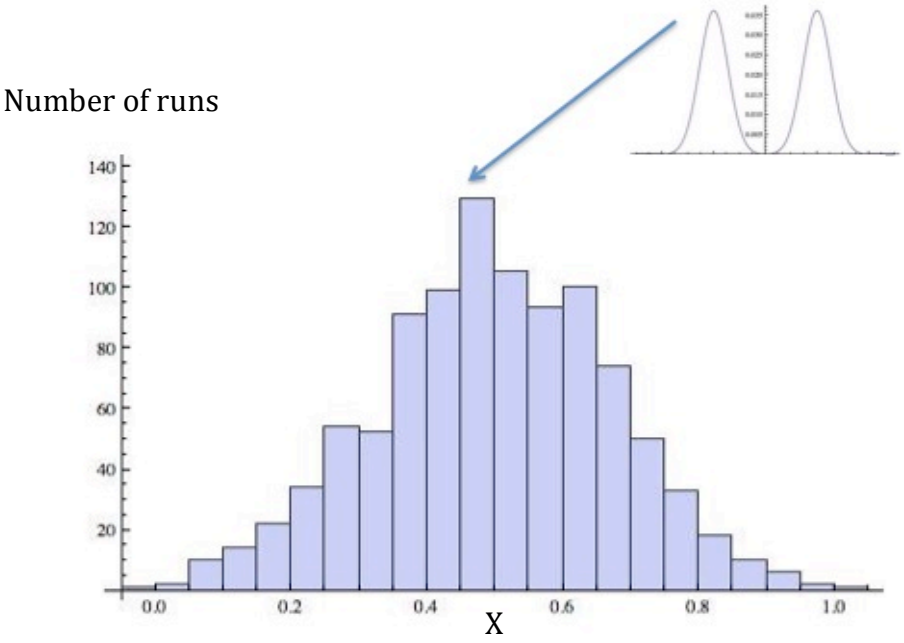

Figure 24. Amplitude of the density of one of the spots for outcoupling, at the midpoint that corresponds to a relative density profile of the same bin size. Mean = 0.5, Standard Deviation = 0.17

That would mean the amplitude of the density of one of the spots could be varying in a Gaussian across all region [0,1] to accompany standard noise characteristics.

Such varying density profile can be attributed to relative intensity or relative phase fluctuations of the beam hitting the atoms, or density instabilities in the condensate. Either way, this can easily accompany all noise factors that would lead to a worst-case scenario relative outcoupling. That approach does not take detector imperfections in to account, the assumption is perfect detected pairs and no false counts.

The fringe visibility is thereby affected and has an expected value that can be calculated (Figure 26). Here even the worst cases are taken into account, for example when the relative density difference between sources is 99%, corresponding to a very low value in the fringe visibility. The numerical simulation takes into account the density fluctuations between sources varying as a Gaussian distribution centered at 50% with a standard deviation of 17%.

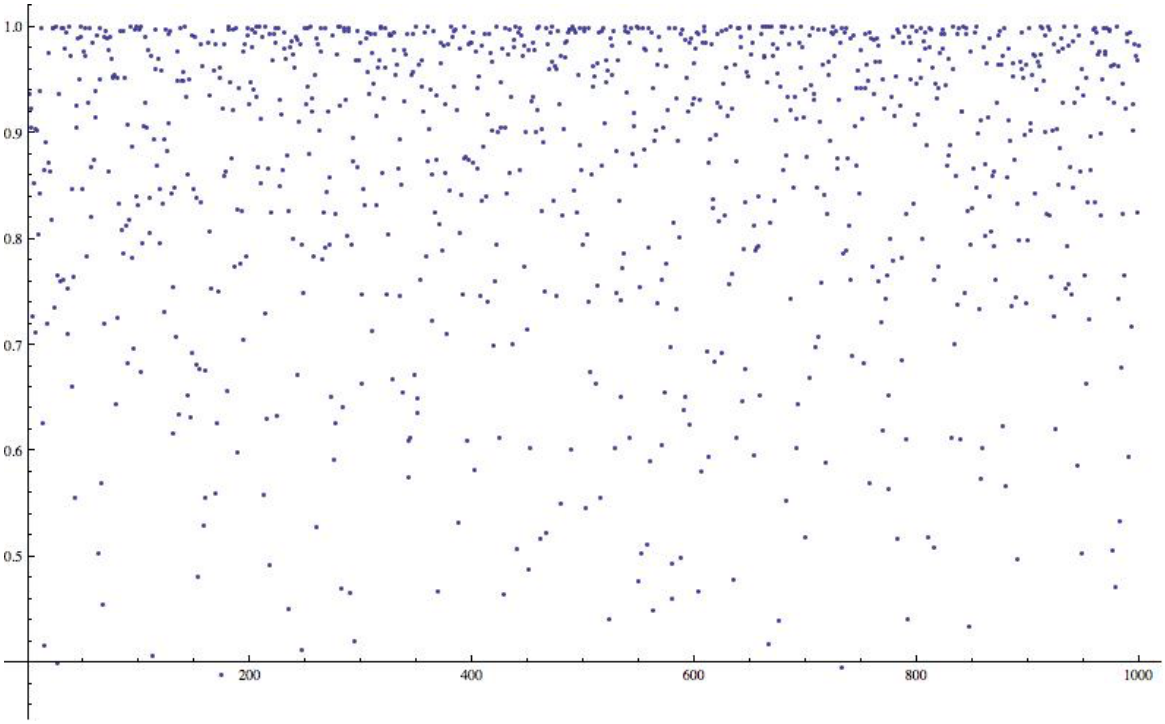

Figure 25. Fringe visibility estimate as a function of the runs

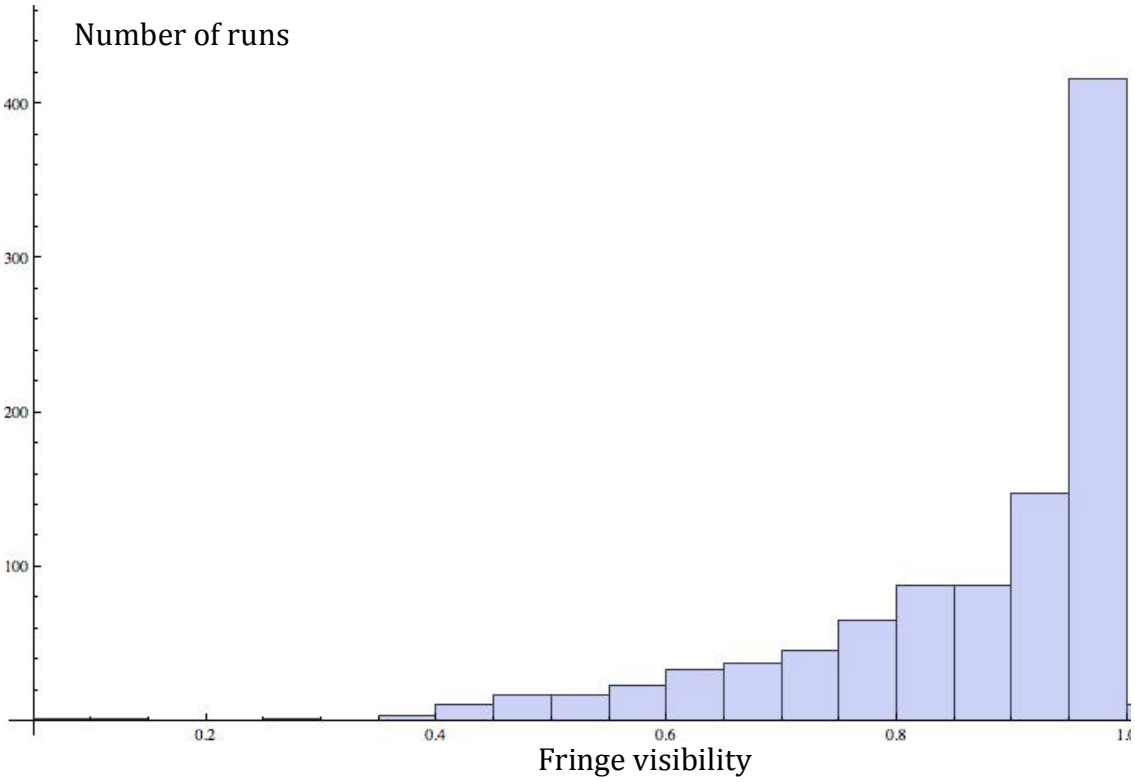

F*igure 26. The fringe visibility plotted also as a distribution*

To conclude we could expect a visibility (not taking detector imperfections into account) of 0.868 ± 0.149.

It is also interesting to note that this result is in fact similar to a previous calculation, essentially found in Wolf's book on different intensities per slit on a double slit from a coherent source. The visibility there is defined in terms of the correlation function (Gamma) and a factor

$$V = \frac{2\sqrt{I_1}\sqrt{I_2}}{I_1 + I_2}|Gamma|$$

It is interesting to compare this equation to the results for the Fringe visibility taking different source densities into account. For making use of the idea, we can define the intensities in a double slit scenario as the densities of the sources here. It works comparatively well down to a ratio of the densities of 95 to 5, where larger ratio leads to a Gaussian in the conditional interference pattern, no fringes visible (Figure 27).

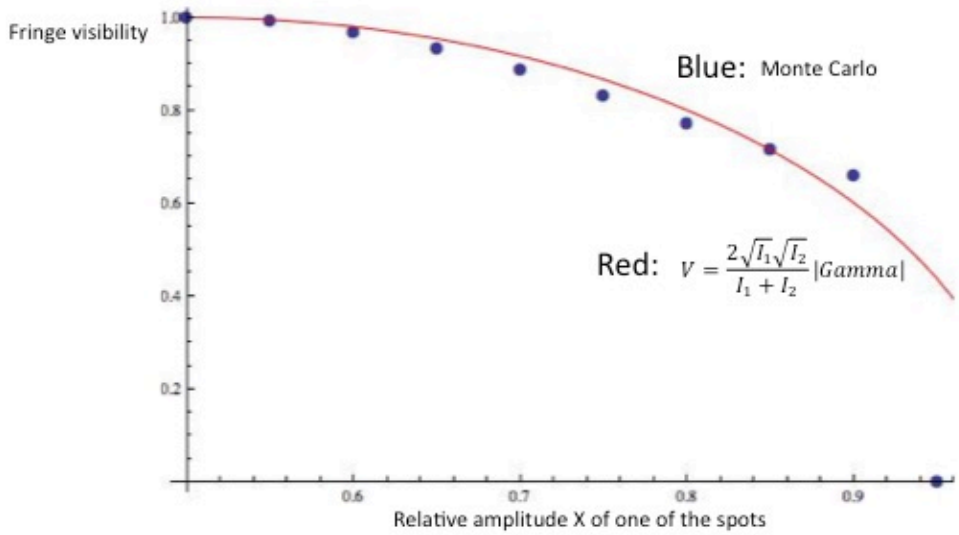

Figure 27. Comparison of different intensities on a double slit and Monte Carlo result; (At the ratio of around (0.95, 0.05) of relative density amplitudes, there are no fringes, only a Gaussian seen at the detector and I define the visibility as 0.)

An example of what the pattern could look like is the following in Figure 28.

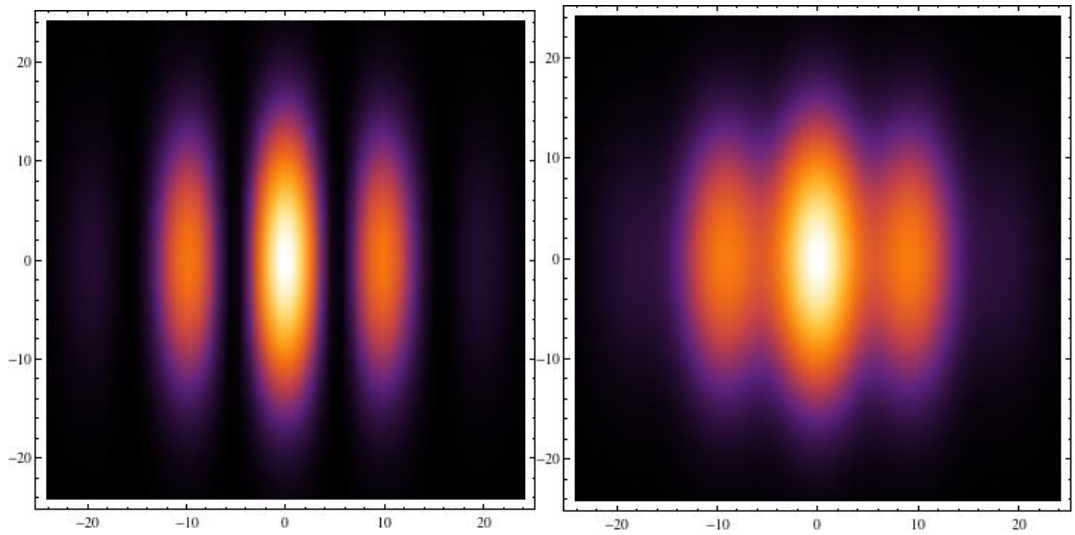

Figure 28. Left: Relative density amplitudes of (0.5, 0.5). Right: Relative density amplitudes of (0.8, 0.2). The idea here is to show that with an imbalance at the source densities, the fringe visibility suffers.

This approach shows a worse case scenario, when the relative density between sources fluctuates in a Gaussian way, but still the fringe visibility is high enough.

3. Optical dipole trap

3.1. Basic idea of dipole traps

Methods to trap charged and neutral particles have very often served as the experimental ingredient for great scientific advances, covering a wide range of physics in ultracold atomic quantum matter and even elementary particles. The ultralow-energy region developments became accessible in the field as a result of dramatic improvements in the field of laser cooling and trapping, which have taken place over the last three decades [72-78].

Historically, the optical dipole force, acting as confining mechanism in a dipole trap, was considered the first time from Askar'yan [79] in connection with plasmas and neutral atoms. The possibility of trapping atoms with this force was considered by Letokhov [80]. Ashkin [81] demonstrated trapping of micron-sized particles in laser light based on the combined action of the dipole force and radiation pressure for the first time. The dipole force on neutral atoms was first demonstrated by Bjorkholm [82]. As a great breakthrough the group of Chu exploited this force to realize the first optical dipole trap for neutral atoms [83]. After the enormous progress in laser cooling and trapping much colder and denser atomic samples were made in a different variety of trap configurations. Even the SLM was included in an experiment to produce the first box potential that could successfully trap atoms [84]. This three dimensional optical box is simply one of the many advantages the SLM offers to produce interesting experimental phenomena in relation to the Bose-Einstein condensate. It opens new possibilities for fundamental and many- body physics.

When atoms are placed in an oscillating electric field, they obtain an induced electric dipole moment that oscillates with the driving frequency of the field. The optical dipole force arises from the dispersive interaction between the induced atomic dipole moment with the intensity gradient of the light field [31-33]. Since the force is conservative, it can be derived from a potential, the minima of which can be used for trapping of atoms. The absorptive portion of the dipole interaction in far-detuned light leads to residual photon scattering, setting limits on dipole traps. The ratio between the magnitude of the electric field and the amplitude of the induced dipole moment is given by the complex polarizability [34]. Here w_0 signifies the eigenfrequency of an electron bound elastically to the core of an atom and w the driving frequency of the electric field.

$$\alpha = 6\pi\epsilon_0 c^3 \frac{\Gamma/w_0^2}{w_0^2 - w^2 - i\left(\frac{w^3}{w_0^2}\right)\Gamma}$$

The potential energy is related to the induced dipole moment by the real, dispersive part of the complex polarizability, which

describes the magnitude of the in-phase oscillation of the dipole moment and the magnitude of the out-of-phase oscillation is related to the imaginary part of the polarizability, associated with the rate at which photons are absorbed and spontaneously re-emitted:

$$U_{dip}(r) = -\frac{1}{2\epsilon_0 c} Re(\alpha) I(r)$$
$$\Gamma_{sc}(r) = -\frac{1}{\hbar \epsilon_0 c} Im(\alpha) I(r)$$

In the far-off resonant regime, when the detuning is large, the evaluation of these relations result in the following expressions for the dipole potential and the scattering rate [35], where Γ is the damping rate

$$U_{dip}(r) = -\frac{3\pi c^2}{w_0^2 (w_0^2 - w^2)} \Gamma\, I(r)$$
$$\Gamma_{sc}(r) = \frac{6\pi c^2 w^3}{\hbar} \left(\frac{\Gamma}{w_0^2 (w_0^2 - w^2)} \right)^2 I(r)$$

In the case of red detuning, irradiating the atoms, the dipole potential has a minimum value when the intensity is at a maximum, thereby producing a trapping potential for the atom. In the case of blue detuning, the real part of the polarizablity is negative (the induced dipole moment is lagging behind the electric field) – the dipole minimum is when the light intensity is at a minimum.

In this case of red detuning, the equations further simplify to (Δ here is the detuning)

$$U_{dip}(r) = -\frac{3\pi c^2}{2 w_0^3} \frac{\Gamma}{\Delta} I(r) \propto \frac{\Gamma}{\Delta}$$

$$\Gamma_{sc}(r) = \frac{3\pi c^2}{\hbar 2 w_0^3} \left(\frac{\Gamma}{\Delta} \right)^2 I(r) \propto \left(\frac{\Gamma}{\Delta} \right)^2$$

These are the key equations at interest. Therefore, optical dipole traps usually use large detunings and high intensities to keep the scattering rate as low as possible at a certain potential depth.

3.2 Our first dipole traps

3.2.1. One beam trap

Optical dipole traps allow experimenters to employ a wide range of geometries. The first configuration is the single focused, red detuned, Gaussian beam. The potential is given by (propagating in the "z" axis)

$$U_{dip}(r,z) = -U_o \left(\frac{w_0}{w(z)}\right)^2 Exp\left[\frac{-2r^2}{w(z)^2}\right]$$

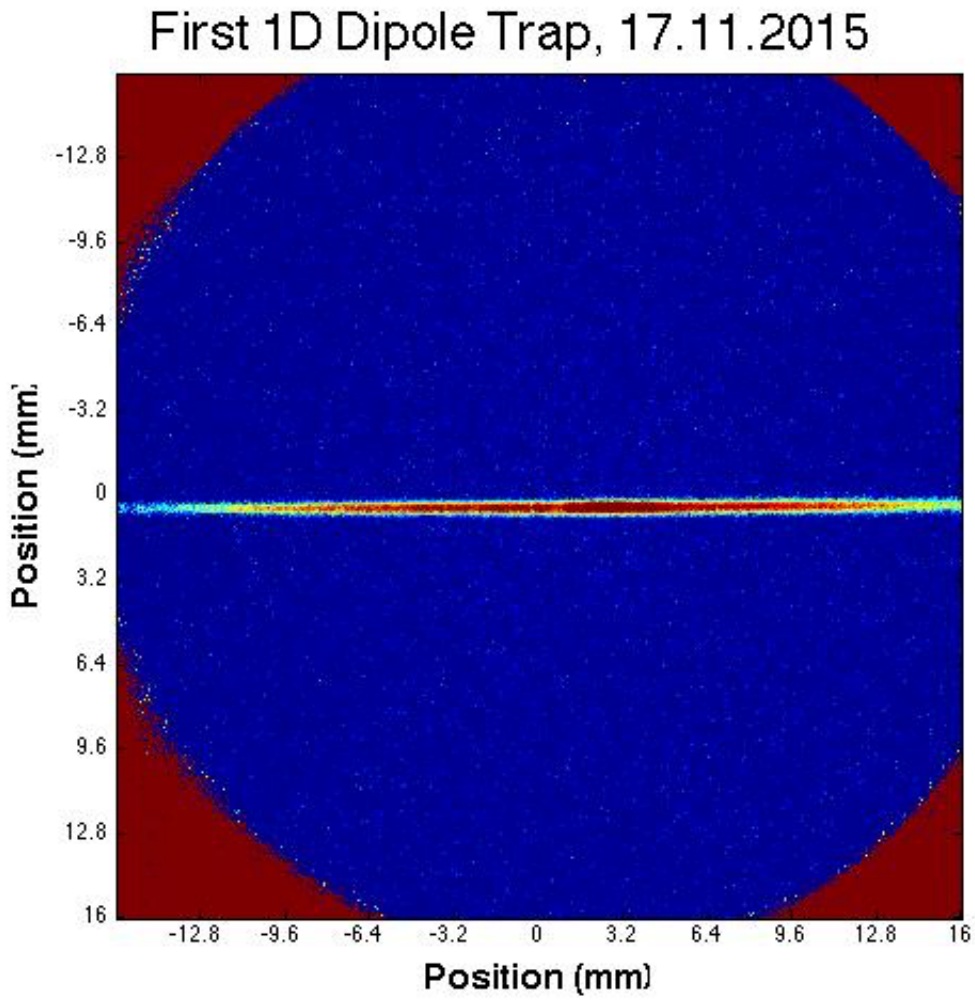

Figure 29. Absorption image of helium atoms in a one-beam optical dipole trap

where z_R is the Rayleigh range and w_0 the beam waist

$$w(z) = w_0\sqrt{1 + \left({}^{z}/_{z_R}\right)^2}$$
$$z_R = {}^{\pi {w_0}^2}/_{\lambda}$$

The radial confinement is stronger than the axial one by a factor of ${}^{\sqrt{2}\pi {w_0}^2}/_{\lambda}$, with a beam waist of about 115 um and wavelength of 1.557 um.

3.2.2. Crossed beam trap

In order to increase the strength of the axial confinement, a crossed beam trap is realized. The way it is done is by crossing two single-beam dipole traps (ideally of equal intensity, we are retro-reflecting the 1D trapping beam to obtain the cross trap) such that the foci match at some angle. Where the foci meet and the trapping beams intersect, the AC Stark shift doubles and a dipole potential arises. The trapping frequency in the direction orthogonal to the plane of the two beams is

$$\omega_z = \sqrt{4U_0/m{w_0}^2}$$

And

$$\omega_x = w_z \cos\left(\frac{\theta}{2}\right)$$
$$\omega_y = w_z \sin\left(\frac{\theta}{2}\right)$$

Consider the situation where we have initial power Pin, and powers P1 and P3 hit the atoms. T here is the transmission coefficient of a vacuum window

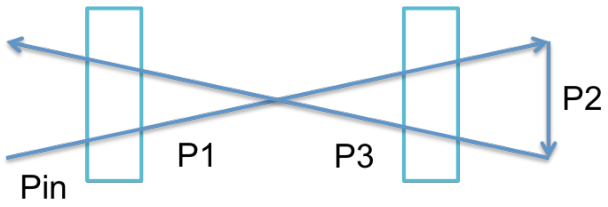

$$P1 = T\ Pin, P3 = T\ P2 = T^3\ Pin, P(atoms) = P1 + P3 = Pin\ T\ (1 + T^2)$$

The efficiency of the AOM (with which we control the power of the beam being sent to the atoms) is 43%, so with 10W output from the fiber amplifier there will be 4.5W-5W available as Pin. That leads to 6.5W power that the atoms would receive at the crossed trap.

There will be additional loss due to efficiency of mirrors and lenses, where for silver mirror the loss could reach 2.5% and 1% for a lens. For that particular setup used the total losses are about 18%, which leaves the atoms with about 5.3W of power P1+P3.

Since we were going to update the setup shortly within a month, no trap frequencies were measured. The way it is normally done is by exciting atoms into a dipole oscillation mode in one direction by applying a magnetic field gradient in the corresponding direction. Then, the atoms are held for a variable amount of time after which the trap is switched off. After a short TOF, absorption imaging is performed and the position measured. Fitting sine functions to position with respect to holding time reveals the desired trap frequency measurements. However, we could clearly observe a BEC and perform a short set of experiments on that.

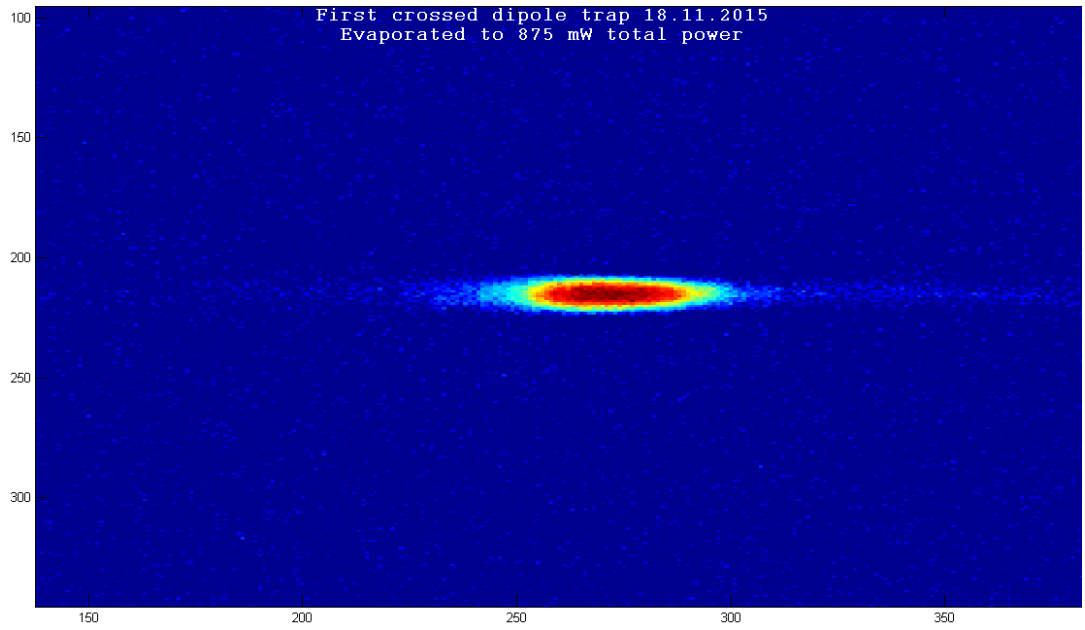

Figure 30. Absorption image of helium atoms in a crossed beam optical dipole trap

At full power, we measure a lifetime of in between 670ms and 930ms, when the two beams P1 and P3 had orthogonal polarizations and when they both the recycled and initial beams had horizontal polarizations, we measured a lifetime of about 1.64s at full power.

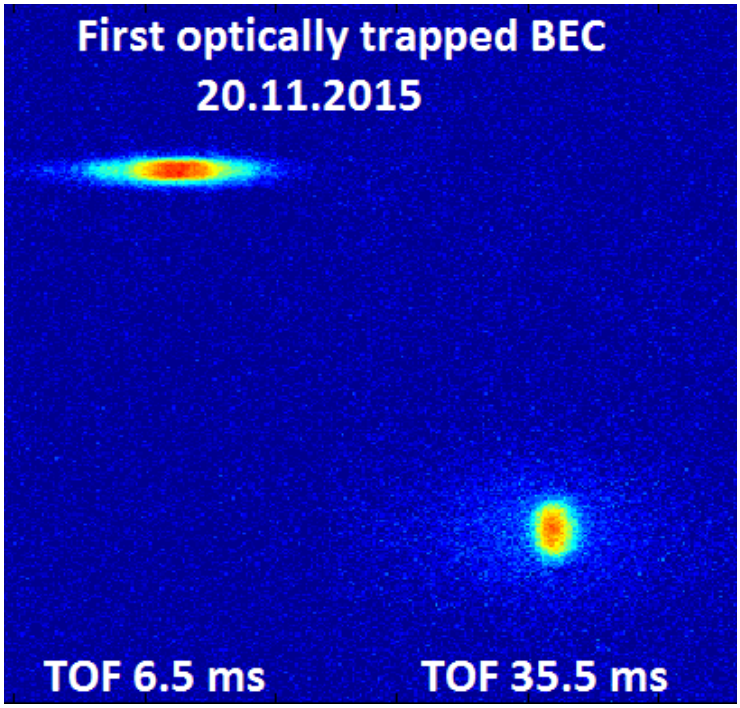

Figure 31. A time of flight measurement with the crossed beam trapped BEC. The inversion of cloud dimensions is consistent with the presence of a BEC

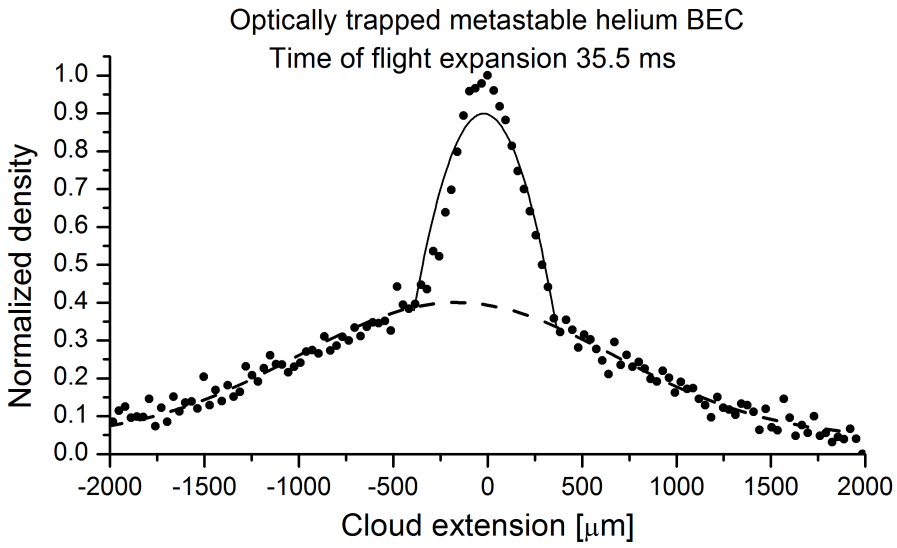

Figure 32. Normalized density of a partly condensed atomic cloud versus cloud extension as measured from the ODT BEC after TOF of 35.5ms. The black solid line represents the fit of the bimodal distribution and the dashed line the thermal component

3.3. Evaporation trajectory

Far-off resonance optical dipole traps are well known to provide nearly state-independent potentials to confine atoms [36]. The way evaporative cooling in an optical dipole trap is done is by lowering the trapping depth, producing a BEC in a few seconds. It is known that the evaporation rate of a gas from an optical trap of fixed depth stagnates as the temperature decreases [38].

The typical idea of evaporative cooling is to increase the number of atoms that reach a quantum degeneracy level. Atom losses via three-body recombination and background collisions limit the attainable efficiency for most experimental efforts in evaporative cooling techniques. In principle, if the evaporation proceeds too slowly, two-body losses become the major loss mechanism and limit the efficiency and if it is too fast, three-body losses become dominant affecting the efficiency [95]. In the experiments that led to the creation of quantum degenerate gases the trap depth was lowered using a series of linear ramps of various duration. We have also employed such a tactic in order to achieve evaporation from the optical dipole trap. However, since the evaporation trajectory we were employing was inefficient, some changes had to be made. We can optimize the evaporation with a total evaporation time of about at least 0.6s. In order to overcome the effect of gravitational sagging, which compromises the confinement, another tool to control the direction of the magnetic offset coils was further developed.

The relation between expected particle number at various trap depths forms a scaling law [36] (particle number N and trap depth U)

$$\frac{N}{N_i} = \left(\frac{U}{U_i}\right)^{\frac{3}{2(\eta'-3)}}$$

where $\eta' = \eta + \frac{\eta-5}{\eta-4}$ and η is the ratio of the trap depth U to thermal energy $k_B T$

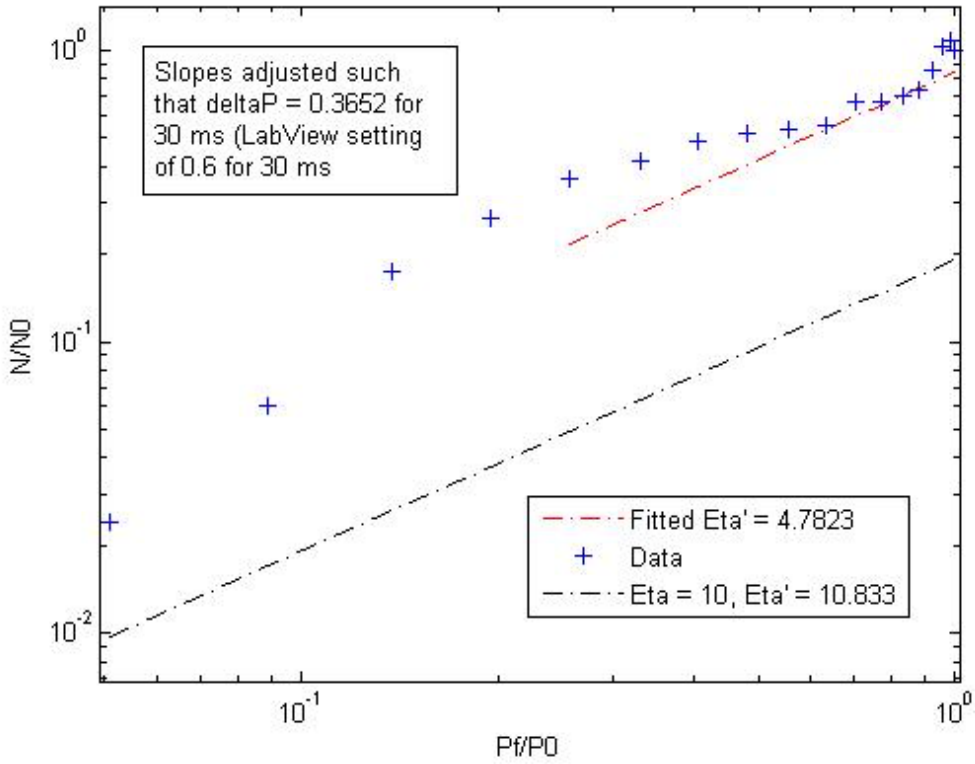

Figure 33. Particle number as a function of crossed optical dipole trap power (i.e., trap depth). The typical efficient evaporative cooling techniques in optical dipole traps employ a η=10. The measurement provides a η=4.8, so further work needed to be done to optimize the evaporative cooling technique at use. N0 here signifies the initial atom number in the trap before evaporation

In order to improve on the evaporation efficiency, a program was written using linear spline interpolation in order to find the best (minimum average offset error) linear splines to a particular exponential model, which we want to follow up with a ramp as close as possible. We could go even lower than 1s or even a bit lower based on the atom number in the BEC and lifetime tradeoff we wanted to achieve. The code has a GUI and it computes the interpolation within at most 125ms computational time. Settings are also printed in the GUI. One can then get the output (provided input that characterizes the ideal exponential evaporation) and log it directly into LabView. The GUI looks like the following:

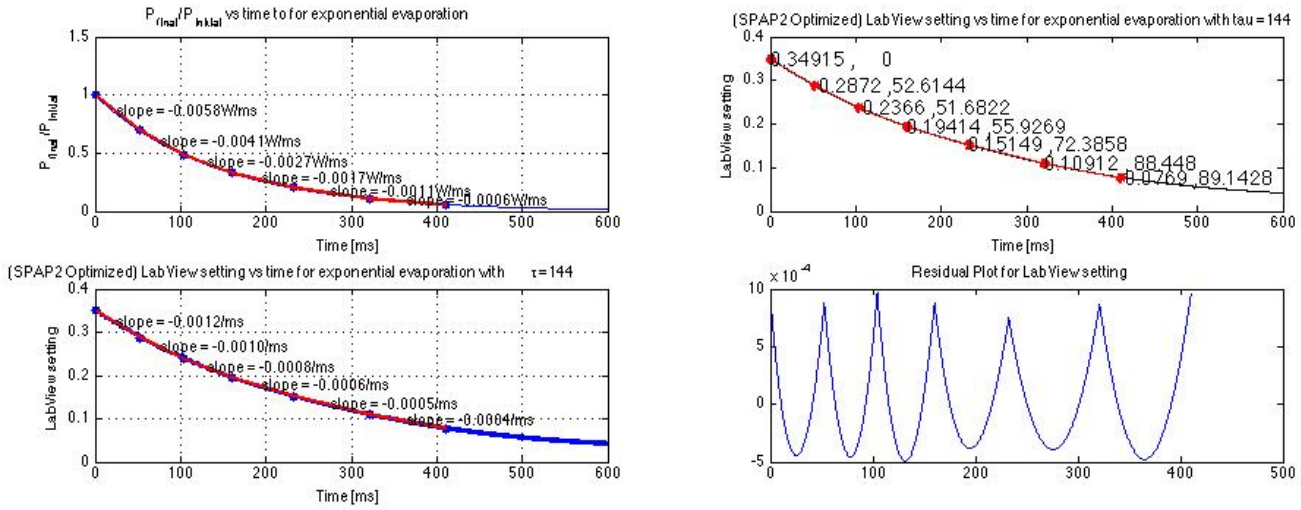

	initial time [ms]	final time [ms]	duration [ms]	final power[P_final/P_initial]	slope [W/ms]
1	0	52.6144	52.6144	0.6956	-0.0058
2	52.6144	104.2966	51.6822	0.4815	-0.0041
3	104.2966	160.2235	55.9269	0.3284	-0.0027
4	160.2235	232.6092	72.3858	0.2020	-0.0017
5	232.6092	321.0572	88.4480	0.1067	-0.0011
6	321.0572	410.2000	89.1428	0.0550	-5.7988e-04

	initial time [ms]	final time [ms]	duration [ms]	final labview setting	slope [per ms]
1	0	52.6144	52.6144	0.2881	-0.0012
2	52.6144	104.2966	51.6822	0.2376	-9.7718e-04
3	104.2966	160.2235	55.9269	0.1950	-7.6093e-04
4	160.2235	232.6092	72.3858	0.1522	-5.9093e-04
5	232.6092	321.0572	88.4480	0.1100	-4.7774e-04
6	321.0572	410.2000	89.1428	0.0779	-3.6051e-04

Figure 34. The evaporation trajectory GUI that can be used for estimating the spline interpolation needed to do efficient ODT evaporation

3.4. Intensity lock for the ODT laser

In order to make the ramps proper without any fluctuations, an intensity lock for the dipole trap is desirable. Such way, an analog signal is sent and the PID follows the ramps, rather than the power values for the trap bottom changing suddenly.

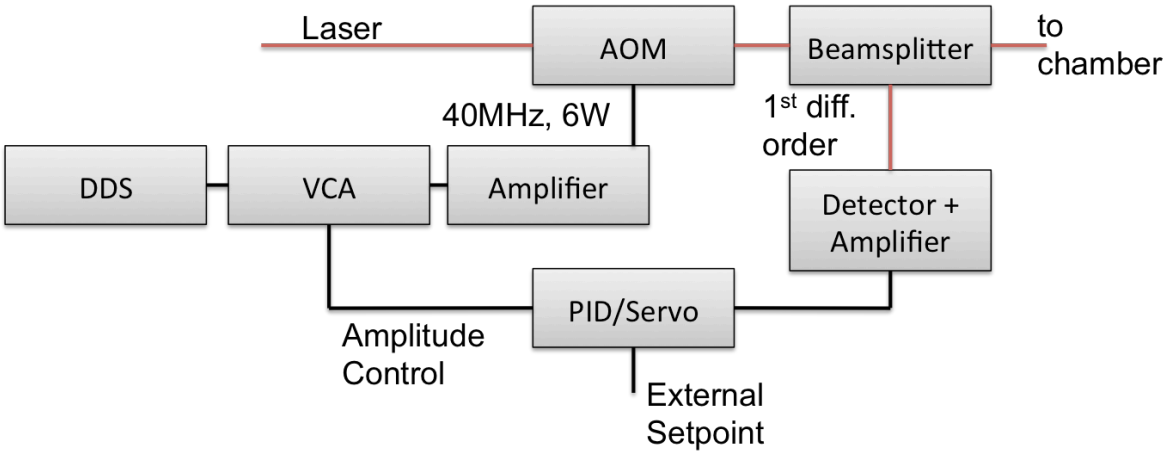

Figure 35. We take off some light from the 1^{st} diffraction order of the 1550 laser, used for the ODT. After providing an external set point by an analog output from the LabView control, we are able to change the amplitude of the voltage signal that goes into the AOM, such that the power level of the laser at the 1^{st} diffraction order is adjusted. This way we can vary the power level of the trap bottom to high precision. Some additional electronics and attenuators were needed to adjust the proper clipping of signals and power values needed for the DAC from LabView, providing the set point and the voltage controlled attenuator (VCA) with which we control the amplitude of the power signal.

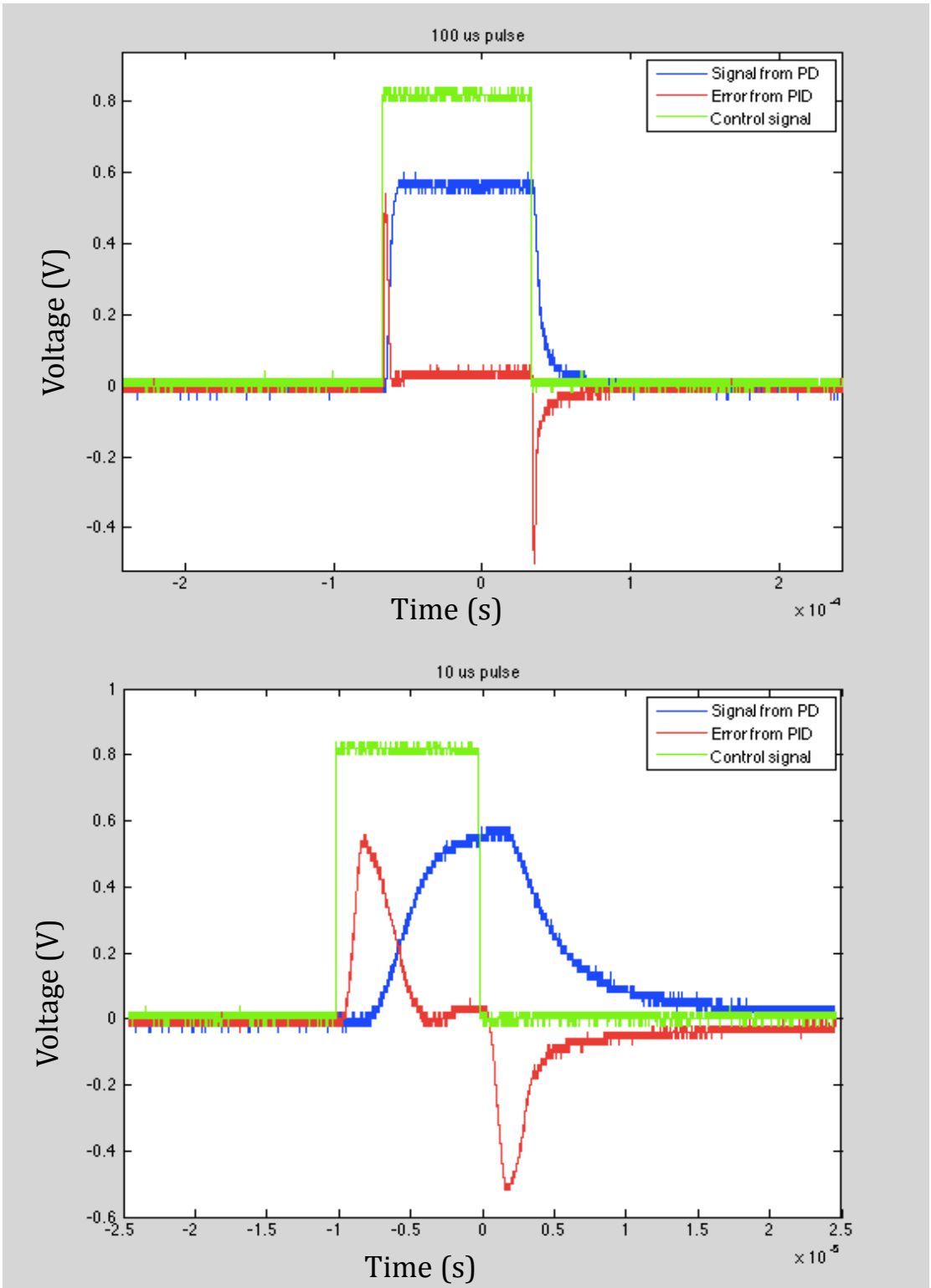

Figure 36. The pulse behavior of the PID

An example from evaporation follows (note: PID parameters were not perfectly optimized for this measurement, which is why there is a lag in the output. The point I am making is that the signals follow ramps from one value to the next, rather than sudden

switching)

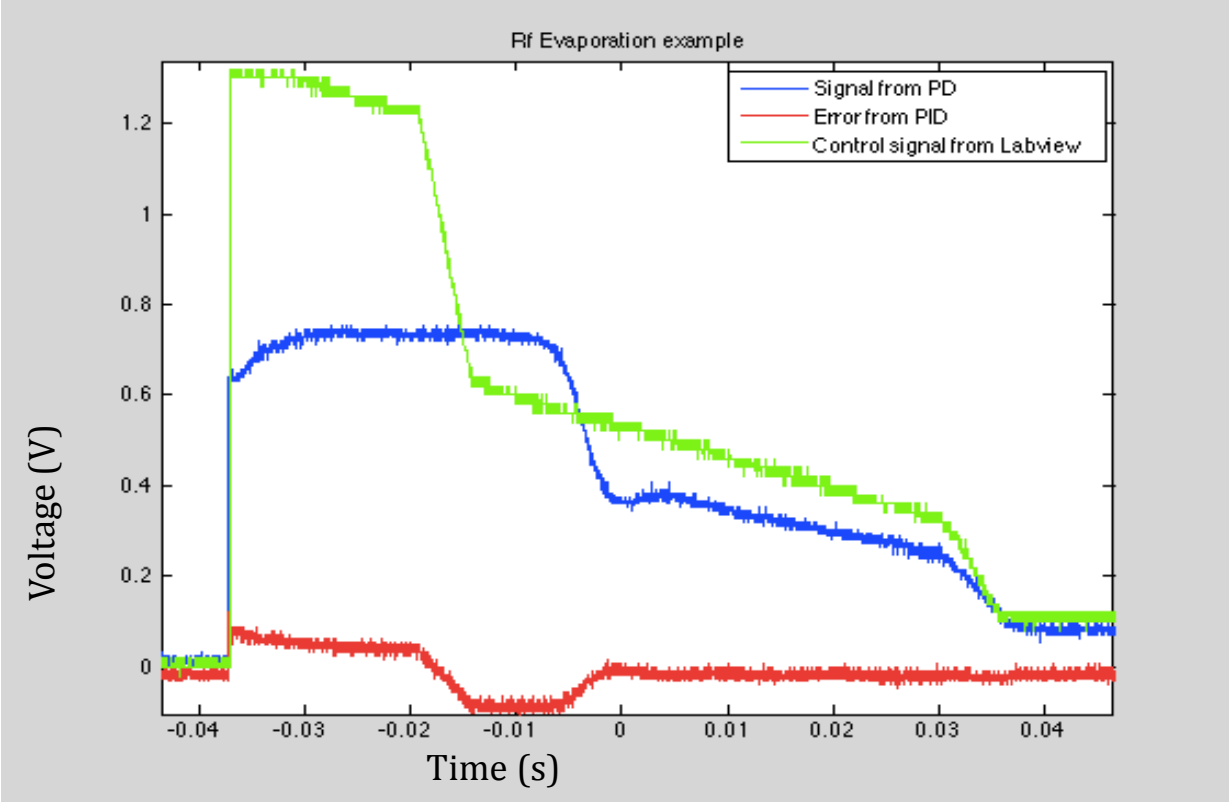

Figure 37. An example of evaporation sequence and corresponding signals from the PID error and PID output signals. The point to make is that the signals follow each other and with proper fine-tuning of the PID parameters even better results and error minimization can be obtained. The point here is that the PID is able to follow a ramping sequence, since the sampling rate is 5us.

The advantage of using the PID instead of applying a ramp to the VCA directly is improved stability of the intensity signal coming out of the AOM used for the dipole trap. The ramp could have also been applied to the VCA directly equally well; the only difference is when the VCA has single set value the intensity signal right after the AOM used for the ODT is more stable. Initially, the fluctuations were on the order of 30%. The PID feedback loop reduced the long-term stability fluctuations. The bandwidth of the used control circuit allows the damping of noise up to approximately 120kHz.

3.5. Current switching circuit used to adjust MOT position

Fine adjustments of the MOT position to optimize its overlap with the CODT are essential for efficient transfer of atoms to the dipole trap and are done by adding a small homogeneous magnetic field that shifts the magnetic quadrupole center. In order to do that, we needed to be able to reverse the direction of current and control it with an IGBT, insulated gate bipolar transistor circuit (which is used primarily because it is more convenient than switching cables). The current control of coils was already in place, but the reversibility needed to be extra implemented.

The way to do this is the same way current is reversed in cars, since we are dealing with high currents on the order of 10A. We can use an H-bridge modulated circuit to do so. The H-bridge is a circuit containing a switching element with the load at the center in an H-like configuration (Figure 38).

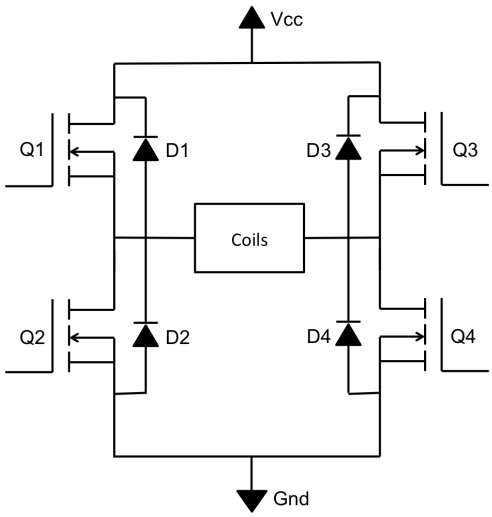

Figure 38. This is an example H bridge configuration with the coils in place of the motor

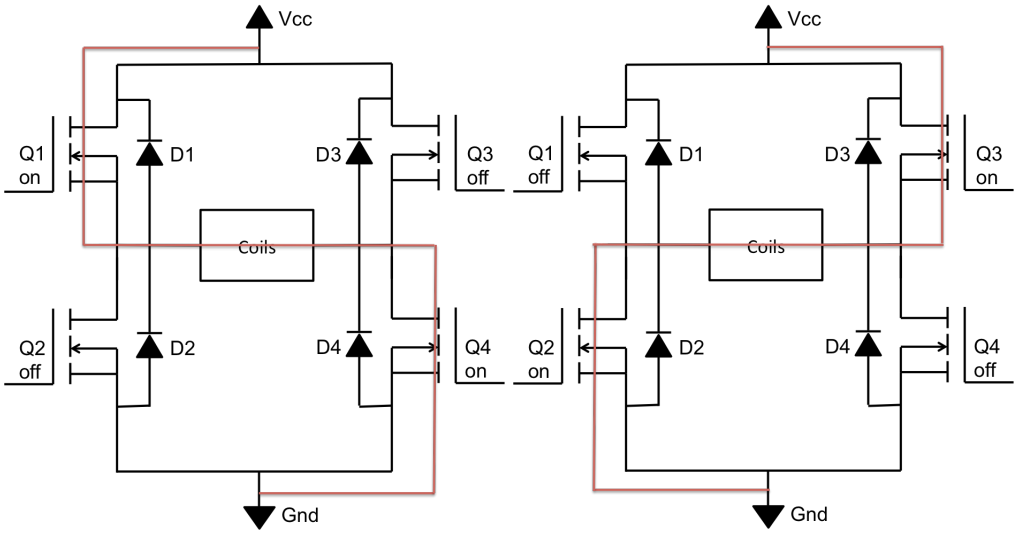

Figure 39. Possible useful configurations of the bridge; proper rerouting is needed in order to achieves these in order that the bridge does not burn out

Two configurations possible (Figure 39): If Q1 and Q4 are on, the left lead of the coils will be connected to the power supply and the right lead to ground. If Q3 and Q2 are on, the right lead will be connected to the power supply and the left lead to the ground. However, Q1 and Q2 or Q3 and Q4 should never be turned on simultaneously, because the H-bridge would burn. Therefore, those are the only two possibly useful configurations allowed. So, in order to overcome the issue of making sure we do not burn the materials, we connected an inverter to allow only those two possible configurations (schematic on Figure 40).

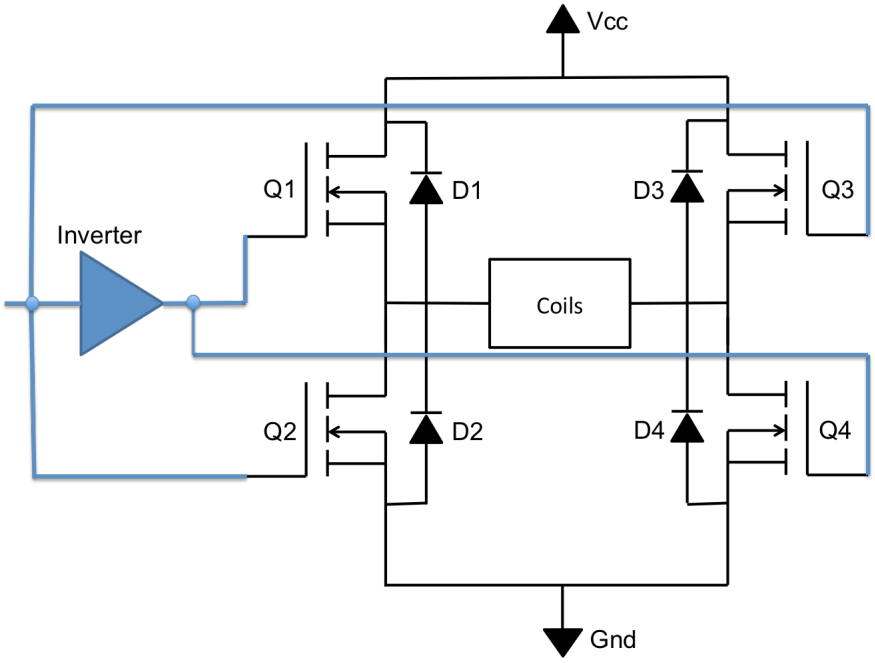

Figure 40a. A schematic of the circuit implemented

Figure 40b. The actual look of the current inverter. Note the heat sink hast to be big, in order to handle up to 20A of current.

The H-bridge used is the APTGF50H60T3G. We had to use a heat sink as well; the maximum power dissipation of the part itself is 250W at 25 degrees Celsius. A logical one (5V) is enough to turn on a particular IGBT on in that configuration. It successfully changes the direction of current in a set of coils, which in this case includes also the current control IGBT.

3.6. Diffracting atoms on a lattice

The lattice in consideration was the dipole trap itself. What we did then is to keep the atoms in the optical dipole trap for a while and then turn it off, after which we pulsed it. The lifetime of the BEC, when running this experiment was about 5s. And the dipole trap is in fact an optical lattice because the beams cross at about 172 degrees angle and have the same horizontal polarization. Therefore, the atoms feel a lattice potential with a periodicity of about 780nm.

When after 500ms hold time for the ODT, the lattice was turned off for 20us and then turned on for 25us, we could observe diffraction of matter waves on an optical grating. More importantly, the diffracted orders collide and we can see scattering waves. Now, this is nothing new here, experiments diffracting atoms on a lattice have been performed earlier [for example 56]. However, the advantage we have here is that we can observe that with the MCP detector and look precisely at the scattering halos in 3D. More importantly, diffracted orders collide and one can see scattering halos. The shells one can see have a diameter corresponding to the relative momentum of the colliding diffraction orders, so we could expect to see shells with radii of approximately

$$\hbar K_G, 2\hbar K_G, 3\hbar K_G, 4\hbar K_G$$

where K_G is the wave vector of the optical grating

$$K_G = \frac{2\pi}{\lambda_G} = 1.99 K_L$$

and K_L is the wave vector of the laser forming the grating. One can clearly see scattered atoms due to collisions of atoms in different momentum states and the scattered atoms are due to collisions between atoms diffracted on the optical lattice. However, these spheres were in a magnetically sensitive state therefore what was detected was strongly distorted.

In Figure 41a one can notice the result after the following procedure. A half wave plate was put in the path of one of the beams. The BEC is not very well visible on absorption imaging, but it looks

relatively fine on the micro channel plate detector (exactly like Figure 41a). Evaporation followed by turn off and then turn on of the dipole trap (basically the sequence as it was performed to obtain the scattering halos) and when the atoms are released after 500ms hold time following the evaporation without any pulsing sequence yield the same result (41a1 for the dipole trap just released after the evaporation without the diffraction sequence and 41a2 with the diffraction sequence). As expected, in both cases, there is no visible influence on the atoms because with the wave plate there should be no lattice (the polarizations are namely orthogonal).

Figure 42 represents the observation of the scattering halos with the micro channel plate detector and equivalently 3D reconstruction. The atoms are held in the optical dipole trap, which was pulsed for 25us. It is key to note here that our dipole trap itself was a lattice during the tests of Figure 42 and 43.

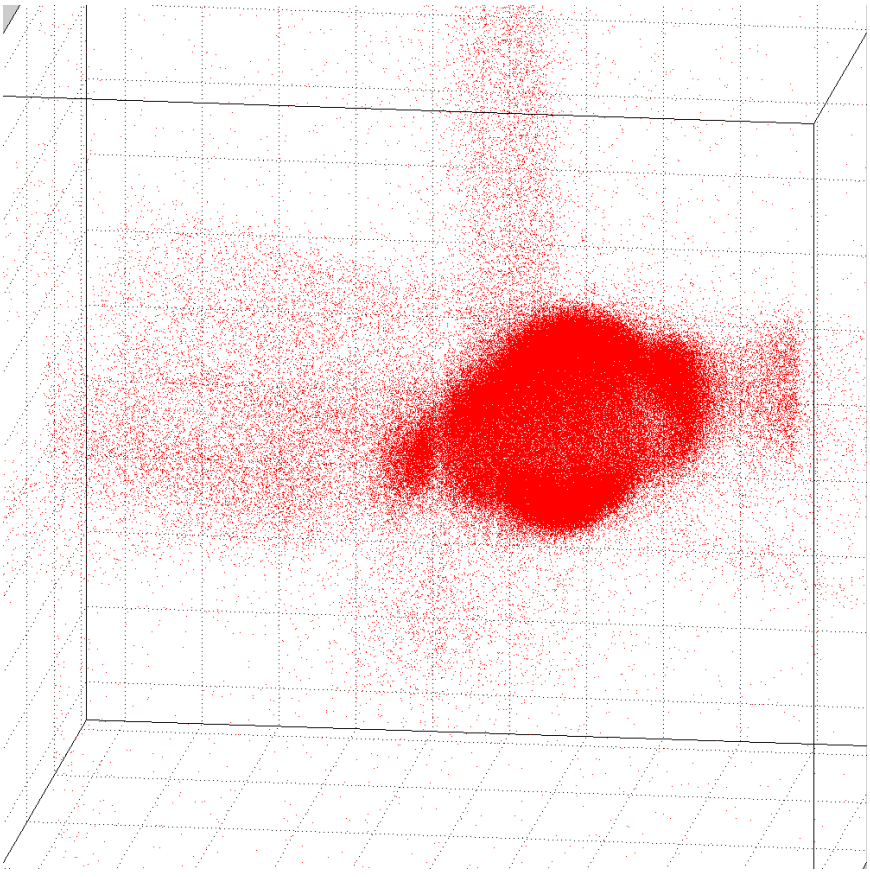

Figure 41a1. When we release the BEC from the dipole trap right after evaporation and there is no lattice involved, the 3D reconstruction looks like the following. (Here no diffraction sequence is performed, just releasing the BEC onto the detector).

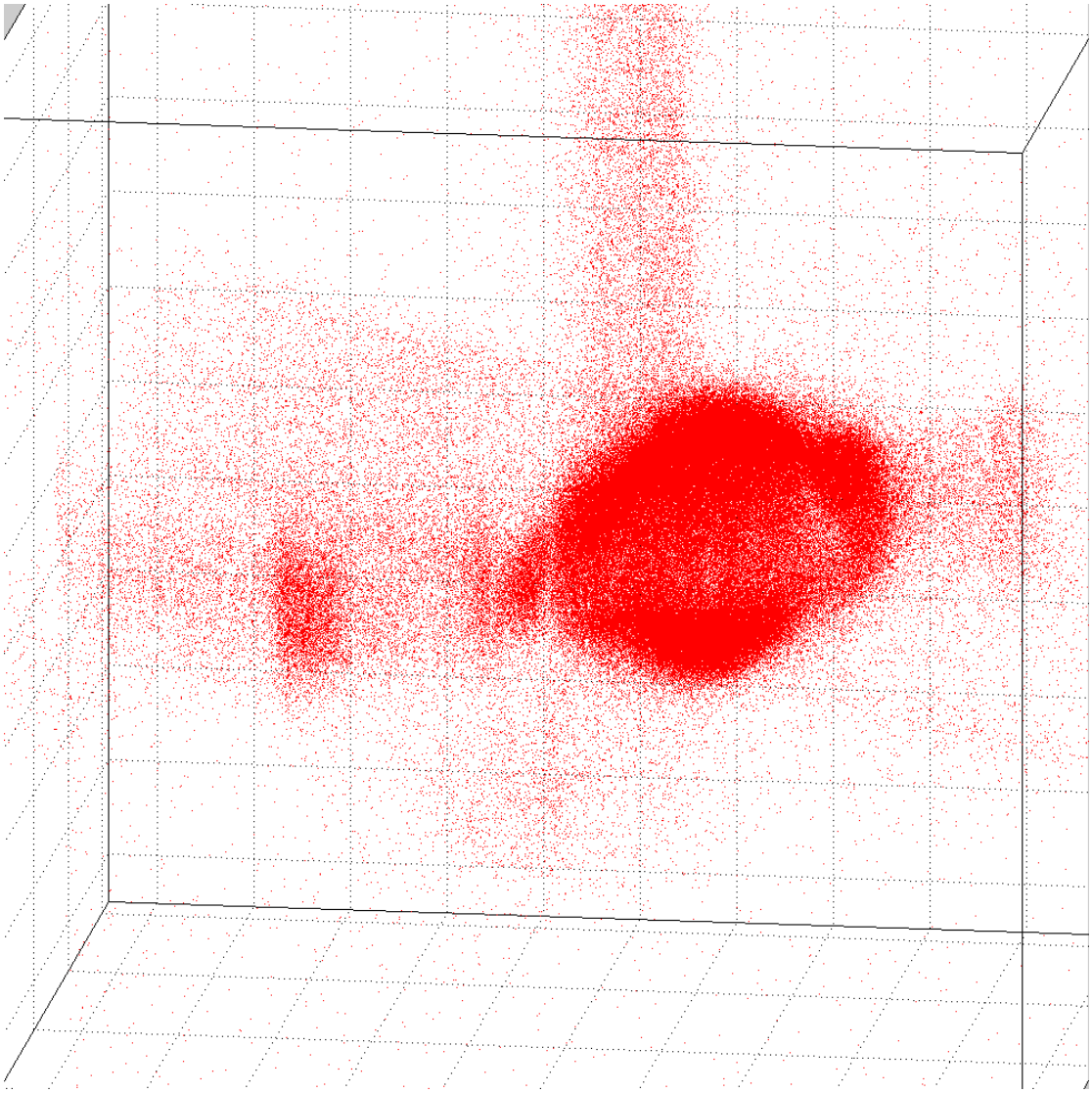

Figure 41a2. We release the BEC from the optical dipole trap with an evaporation sequence. Diffraction halos are not expected because we put a half wave plate in place of one of the beams.

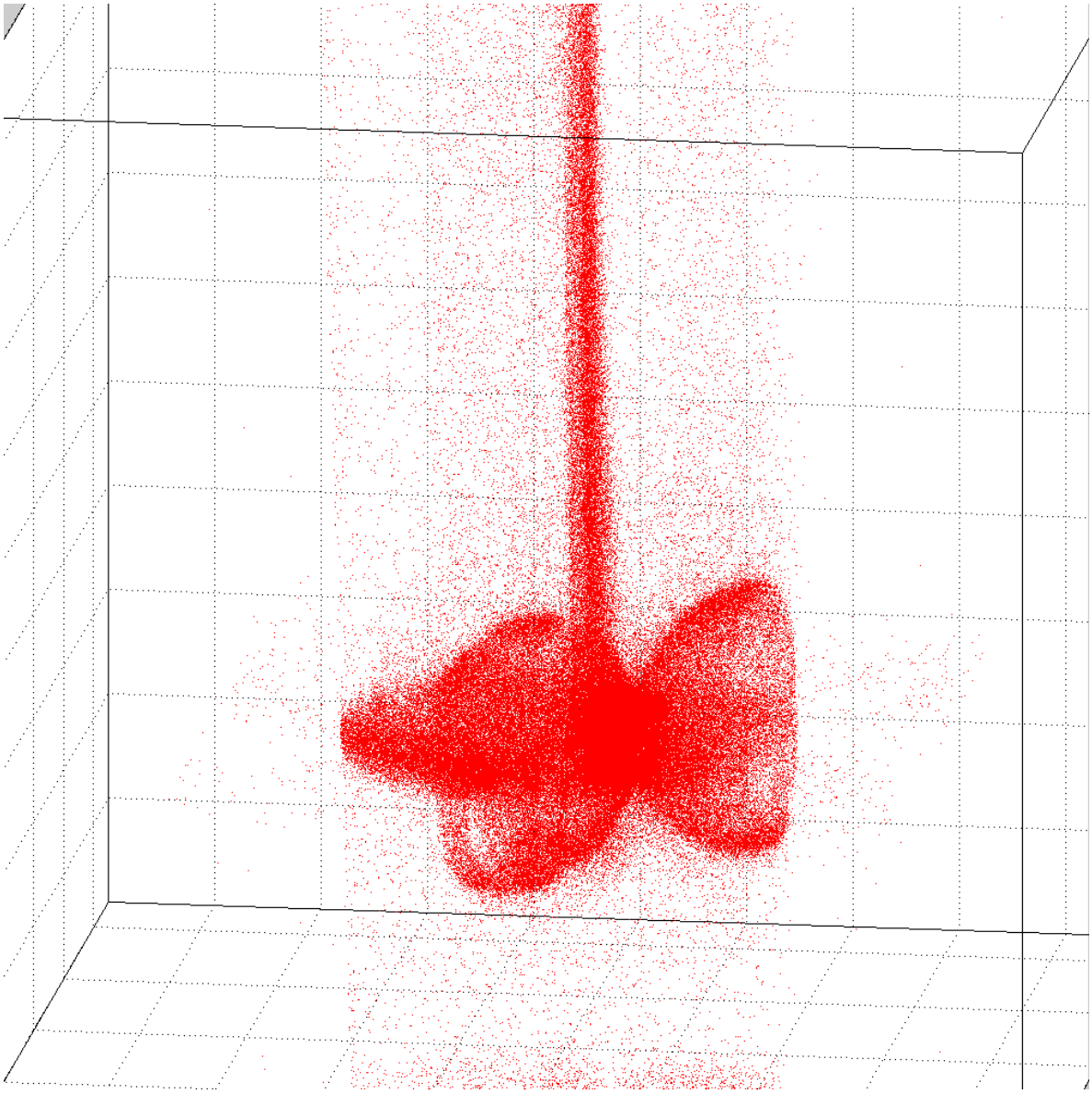

Figure 41b. After holding the BEC in the optical lattice at the lowest power for 500ms and releasing the BEC, the 3D reconstruction looks like the following. Half wave plate was removed. The BEC is therefore falling from an optical dipole trap, which was in fact a lattice.

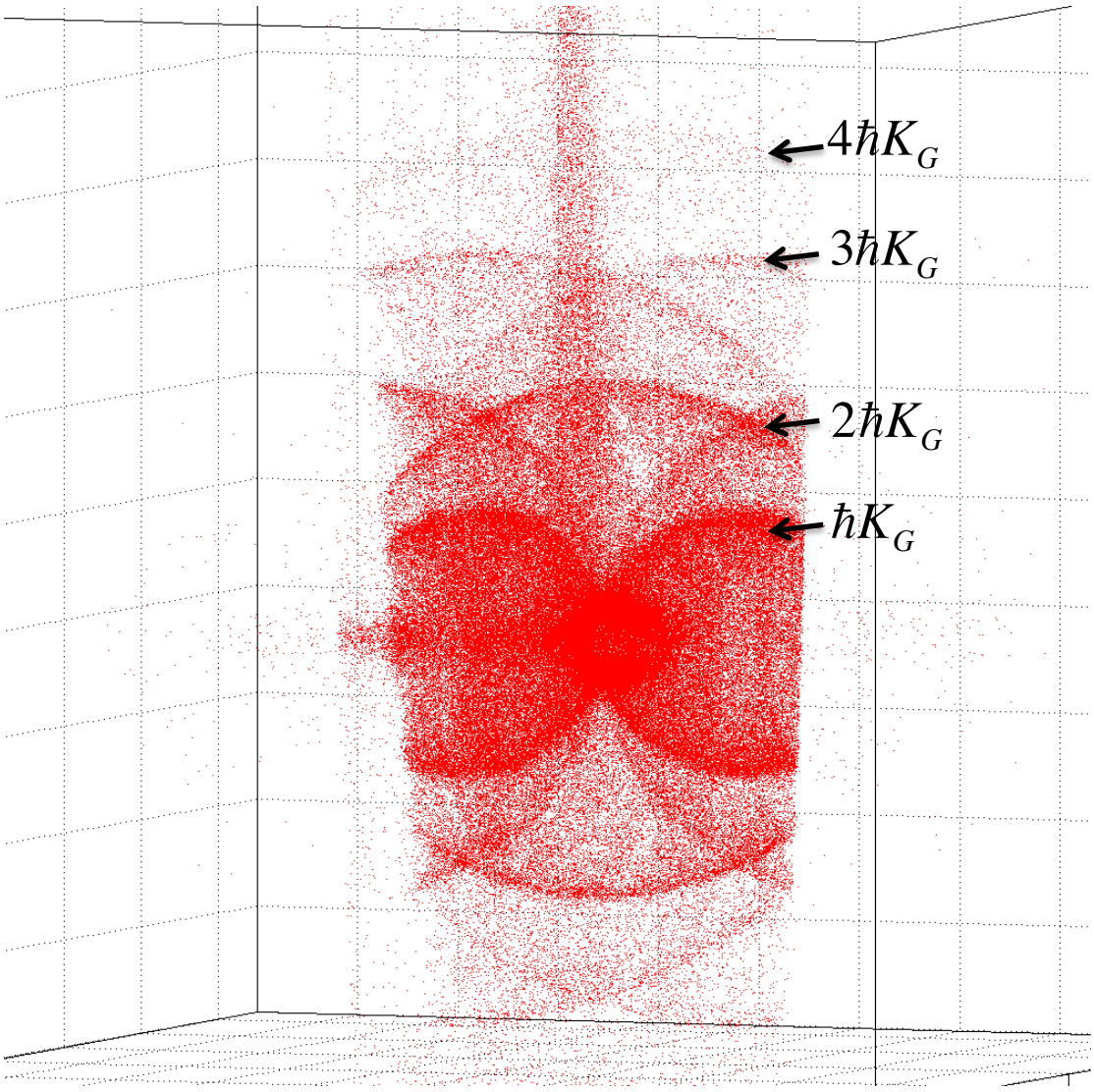
$4\hbar K_G$
$3\hbar K_G$
$2\hbar K_G$
$\hbar K_G$

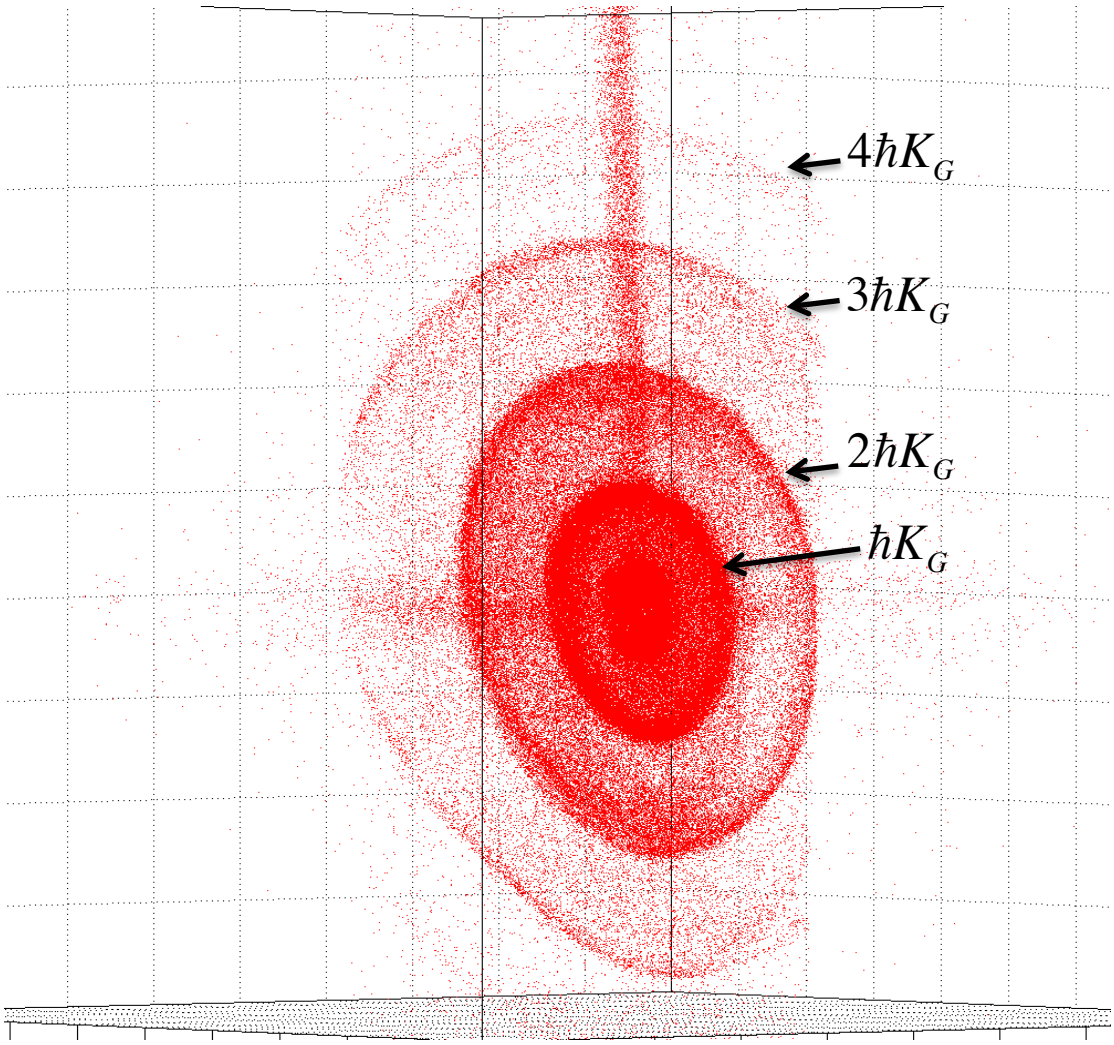

Figure 42. 3D reconstruction with the MCP detector of the scattering spheres at different angles; note the diffraction orders can be easily recognized. There is no half wave plate involved here.

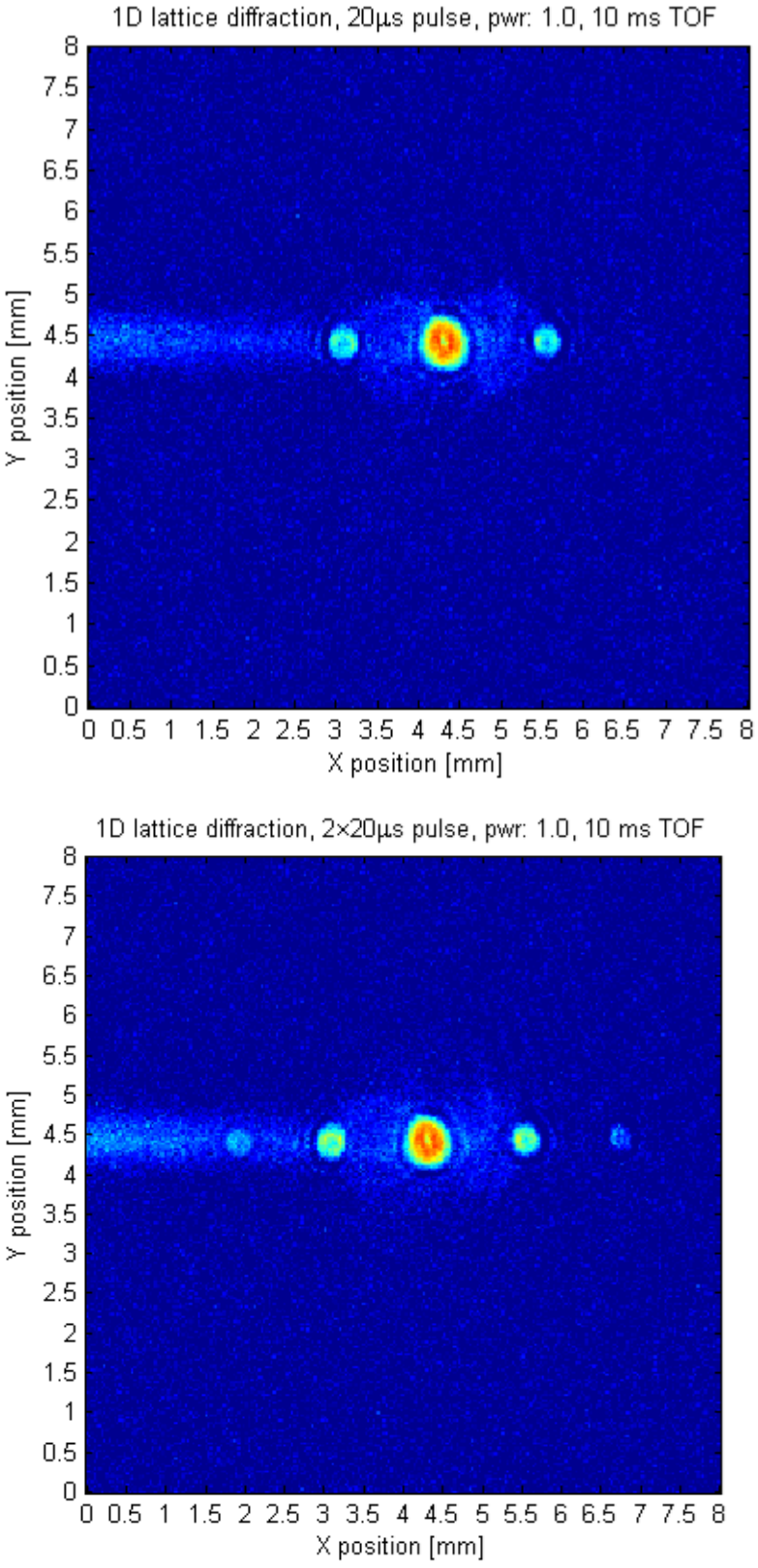

Figure 43. Diffracting atoms on the optical lattice used for trapping. Atoms diffracted on the optical lattice and then colliding. Each picture is average of 20 images. Top: one pulse after the hold time. Bottom: Two pulses after the hold time.

4. Outcoupling atoms with Raman pulses

To obtain the statistics due to entanglement in the external degree of freedom of matter waves well above the statistics within the coherent state of the BEC, the atoms need to be outcoupled from the group of atoms in the BEC. In order to obtain correlated atom pairs, as in the proposed experiment, we use a scheme analogous to the setup presented at [39]. Three laser beams of wavelength 1083nm induce two stimulated Raman transitions in the BEC. These transitions in particular transfer atoms in the BEC from a magnetically sensitive to the magnetically insensitive state creating two condensates with different momenta (since the beams are two from the side and one from the top and each side beam with the top one is producing a momentum kick). This outlook has been well described in detail in the thesis of Maximilian Ebner, former member of our group. We just recently managed to realize this scheme in our laboratory managing to outcouple up to about 10% of the atoms in our BEC into counter-propagating condensates. The anisotropic expansion can be seen, only to be able to be verified with the single atom detector. However, one can observe from absorption imaging that the clouds being outcoupled are indeed BECs as well.

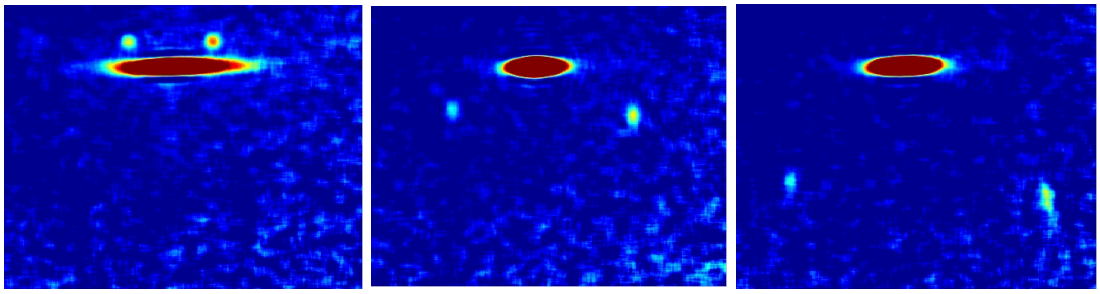

Figure 44. First results of outcoupling of atoms from the BEC with Raman pulses; The two outcoupled condensates can be seen falling and expanding under gravity while the main condensate is kept in place and only undergoes fixed time of flight from switching off the magnetic trap until absorption imaging of all three clouds.

We could also observe this phenomena with the BEC trapped in the

optical dipole trap and equivalently the 3D reconstruction from the micro channel plate detector (Figure 45).

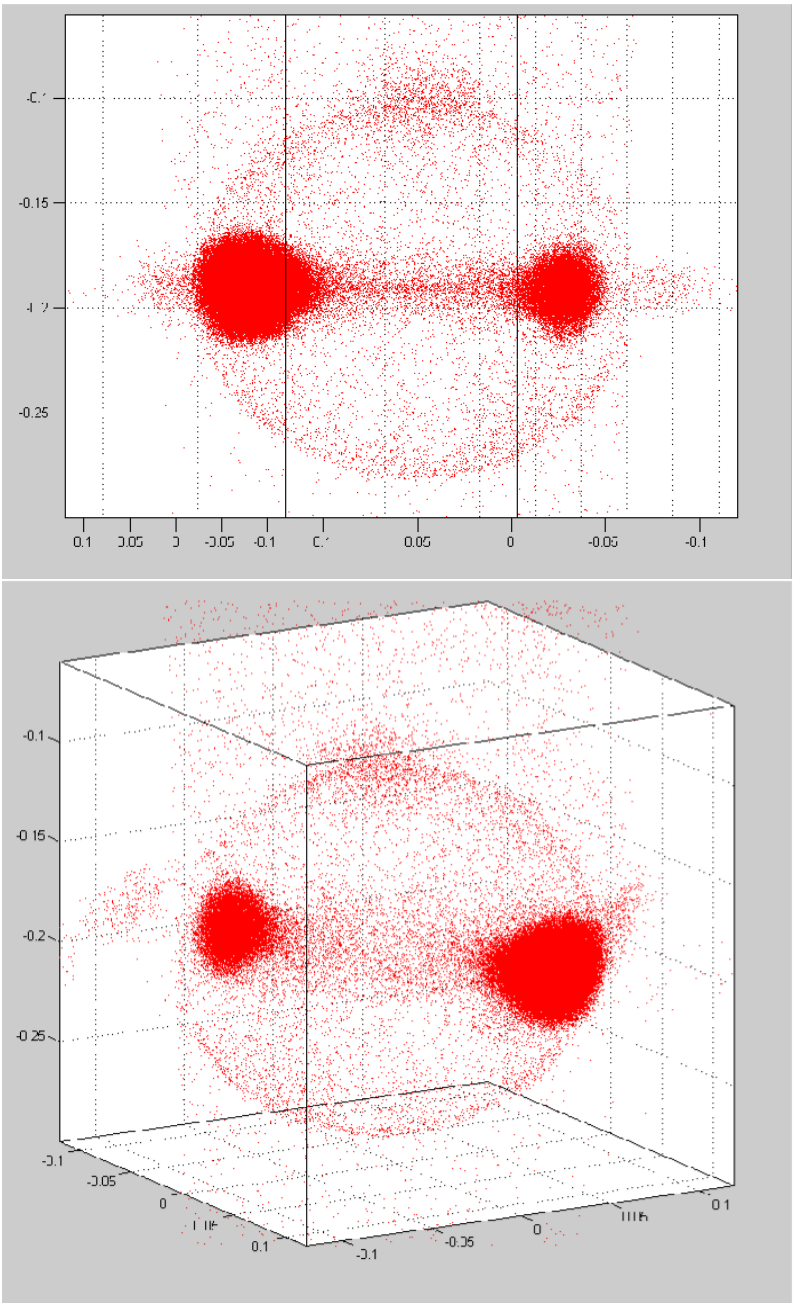

Figure 45. 3D reconstruction of the Raman scattering sphere observed with the micro channel plate detector.

5. Further experiments we can do

5.1. Born's rule test

Quantum mechanics computes probabilities from the absolute squares of complex amplitudes, and resulting interference violates the (Kolmogorov) sum rule expressing the additivity of probabilities of mutually exclusive events. Born's rule predicts that quantum interference, as shown by a double-slit diffraction experiment, occurs from pairs of paths. Deviation from the rule would allow for higher-order (multipath) interference and would require modification of the Schrödinger's equation e.g. in the form of nonlinear extension to quantum mechanics [42], [43].

Following the approach demonstrated for photons by Sinha et al. [41] we can use Bose-condensed metastable helium atoms and outcouple them from the magnetic trap or the optical dipole trap in a configuration corresponding to three slits created by light beams. The slits can be created with a spatial light modulator (SLM) which will allow for their independent control, both in terms of their separation (slit distance) and their size (slit width via an iris and proper algorithmic compensation for the power degradation), with restrictions imposed by the focusing optics and the size of the condensate (~300 micrometers along weak axis).

One possible realization of the experiment is shown in Figure 46. Here, the atoms are outcoupled from the condensate by driving Raman transitions between $m_F = 1$ and $m_F = 0$ Zeeman sublevels in the 2^3S_1 manifold via an intermediate level 2^3P_0. The beam L_2 produced by the spatial light modulator can be linearly polarized along the magnetic field B driving π-transitions. The beam L_1 is also linearly polarized but with the polarization oriented perpendicular to the magnetic field such that, effectively, it can drive σ^- transitions. In such an arrangement there is no net momentum transfer to the atoms, but since the internal state is changed to $m_F = 0$ (which is not trappable) the atoms leave the trap under the influence of gravity. Outcoupled clouds expand as they fall and they overlap producing an interference pattern on the single atom detector located at about 80 cm below the cloud.

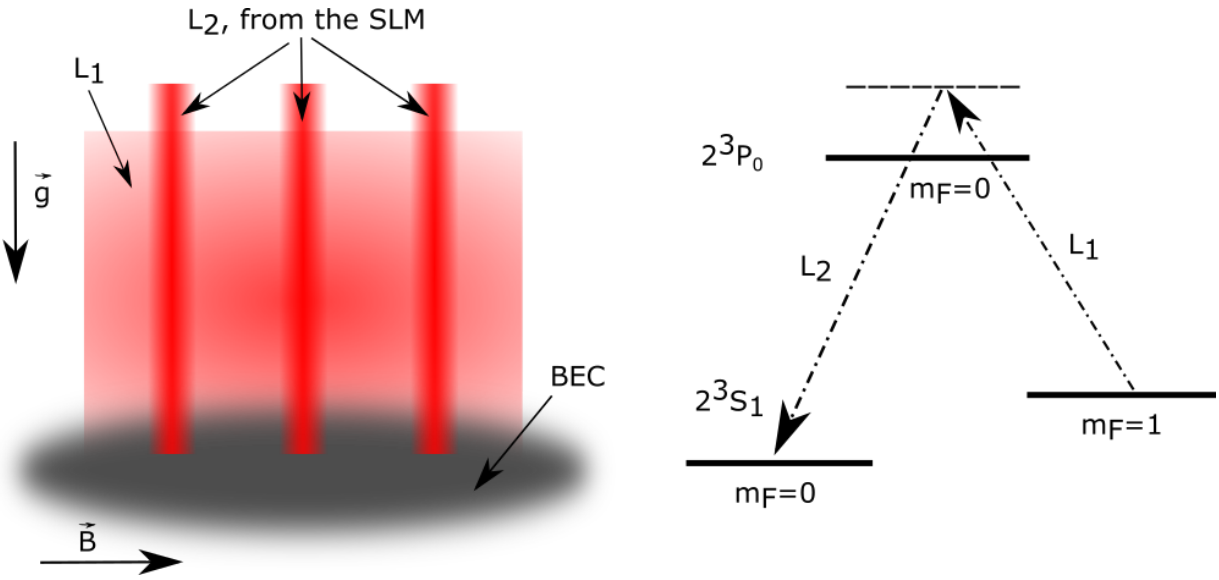

Figure 46. (left) proposed scheme to outcouple atoms from the Bose-Einstein condensate using Raman transitions. The slits are created by shaping one of the Raman beams with a spatial light modulator, providing well-defined regions where the Raman transitions can occur. Here, the gravity is pointing down and the quantization axis is set by the bias field of the magnetic trap; (right) atomic levels used to drive Raman transitions. The beams can blue detuned from the 2^3P0 transition by about 400MHz.

The validity of the Born's rule can be tested by measuring the difference of interference patterns produced by three, two and a single slit:

$$I_{ABC} = P_{ABC} - P_{AB} - P_{BC} - P_{AC} + P_A + P_B + P_C - P_0$$

Here P_{ABC} is the interference pattern when three slits are open, P_{ij} – when pairs (i, j) are open and P_i – when a only a slit i is open. P_0 accounts for the detector and background noise when all slits are off. A non-zero value of the above sum would indicate the presence of higher-order interference.

The Born's rule test would require high shot-to-shot stability of producing BECs over many thousands experimental to get enough counts.

The experiment would serve as a tabletop demonstration of the complete scope of the Feynman path integral formalism where not

only straight-line paths are important but also looped paths that can make sizeable contribution [44]. Those effects could be used to model nonclassical paths and decoherence mechanisms in interferometer-based quantum computing applications.

The proposed experiment would be interesting in fundamental physics applications as this would be the first test of Born's rule with massive particles (as opposed to photons) and influence of gravity on quantum paths might play a role here.

5.2. Vortices and angular momentum

As a consequence of superfluidity of Bose Einstein condensates, adding angular momentum to a BEC (e.g. by 'stirring' it with a laser beam) leads to the creation of vortices. [66] It has been shown that vortices in a BEC can be created in a 2-photon stimulated Raman process where one of the Raman beams poses orbital angular momentum, which can be then transferred to the atoms. [67]

Generally, experiments involving quantized vortices in a Bose-Einstein condensate using optical vortices have become very important since the experimental endeavors over the last decade [85, 86]. The coherent superpositions among vortices of different circulation numbers yield interesting experiments [86, 87] and interference effects, which can find interesting applications [88, 89], such as controlling the chirality of twisted metal nano structures [90]. One can use multiple optical vortices in order to create multiple circulations of a BEC [91-93] or even a single optical vortex pulse [69]. The authors of [69] show that matter-wave vortex superposition from single optical vortex is possible for a focused beam, where the spin angular momentum and orbital angular momentum of light are coupled [94].

Entangled orbital angular momentum states of light have many quantum information and communication advantages, which have been demonstrated by the Zeilinger group. It has also been shown that one can construct a quantum memory for a photonic entanglement for realizing quantum communication and network [68]. Building on the experience of our group with high orbital angular momentum beams and their entanglement an attempt can be

made to generate lattices of 1000's singly charged vortices or vortices with very large charge for example. The latter ones are unstable as the energy of the system with n vortices of charge k is lower than that of a single vortex of charge $n*k$. Single atom sensitivity and superior temporal resolution of the delay line detector can enable us to take on experiments with vortices like aspects of their formation and dynamical behavior.

High-dimensional quantum entanglement can be stored in a BEC efficiently with orbital angular momentum modes of light, resulting in a coherent superposition of vortex states [69], but this has never been looked at a single atom level as most of the experiments relied on absorption imaging.

We also have the advantage of easily creating orbital angular momentum beams with a Spatial Light Modulator and the setup already employs Raman beams for the transfer of linear momentum to atoms, used to outcouple atoms from the BEC. Furthermore, the SLM can generate a light sheet or other more complex optical potentials such that the BEC can be split into two (or more) and the correlations between them can be examine with the aid of orbital angular momentum beams.

The combination of high orbital angular momentum light beams and single photons with a BEC opens up promising variety of experiments including entanglement between photonic OAM and topological charge in a BEC for example or the study of collisional entanglement creation within a BEC carrying orbital angular momentum. Another interesting fact is that the intensity distribution of Laguerre-Gauss modes is proportional to $r^l\ Exp\ [-r^2]$, where r is the radius of the beam and l is the winding number, which describes the helical structure of the wave front. Therefore with high enough orbital angular momentum of light one could realize an almost perfect box potential. Entangling photons with vortices or the BEC as a whole would require modifications to the experimental chamber to facilitate single photon detection but this is a relatively straightforward upgrade.

7. Summary and outlook

This thesis was written to report on the methods to derive an experimental procedure to obtain a setup to produce arbitrary light potentials with the aid of a spatial light modulator. The technical specifications and technical difficulties to employ such a device in order to reach our goals were discussed. The up-to-date algorithms being used were presented, as well as the experimental challenges we faced over the past three years in order to make the setup fully reliable. The algorithm of choice was the "vector holography" algorithm, since it produces the best quality spots, namely with the least standard deviation of the intensity fluctuations in the trapping/image plane of the SLM. For more complex patterns, other algorithms can be easily implemented, such as MRAF and GS algorithm. The analytical functions, which have to be fed to the SLM via a VGA port, were also presented, which includes correction patterns, gratings, lenses etc. The problems arising the utilization of such a device to produce arbitrary controllable light patterns were also discussed. That includes "ghost" traps, correction for the surface roughness of the SLM, relative phase fluctuations when projecting a pattern of two Gaussian beams onto the image plane, the idea of pupil conjugation, wavefront estimation and correction algorithms and devices needed in order to obtain such (we have reached the conclusion that our home-built wavefront-correction device does not perform as well as the commercially available products), controlling the focal length and individual position of either or both of the patterns projected, controlling the relative distance between desired patterns, the problem of optical vortices, which arise upon desire of a larger Gaussian spot or more complex potential on the image plane and finally the outcome of polarization fluctuation between individual patterns on the image plane was discussed. Moreover, the main experiment, we are interested in performing, was discussed form a broader perspective, as well as a Monte Carlo simulation of the effect on fringe visibility result of the main experiment upon varying the intensity amplitude of one of the desired Gaussian spots or different relative density in the outcoupling regions was introduced. Such amplitude variation can come from various noise factors, but they all lead to a different density in the outcoupling regions, which was the core of the Monte Carlo simulation implemented. Entanglement then would be observed upon fringe visibility on the conditional interference pattern higher than 50%.

Taking into account a Gaussian noise distribution on the noise intensity fluctuations between spots upon a worst-case scenario does not inhibit the viability of observing entanglement in our main experiment. Furthermore, some experimental results of achieving our first optical dipole traps were discussed, as well as the main experiment we are looking at in relation to the utilization of optical dipole traps to trap a Bose Einstein condensate in a ODT rather than a magnetic trap. We have achieved a single beam optical dipole trap, as well as a crossed beam and provided proof we have a BEC in the crossed trap. Experimental verification of the trapping frequencies would be our next step. The wavelength used for the ODT was 1550nm. Outcoupling of atoms from the BEC with Raman beams was also achieved and the experimental results presented, as atom clouds were outcoupling from the BEC trapped in the ODT. Furthermore, we have also looked at diffracting atoms on an optical lattice with the 3D delay line detector, where one can easily distinguish the scattering spheres. Plus, the further work on modification of the evaporation trajectory in ODT was presented, increasing the control over evaporation of a BEC from an ODT and decreasing the time needed to do so. Time is not the only factor we were interested in improving. Also, via the linear spline interpolation functions we were able to provide flexibility to achieve a fast evaporation sequence at any trapping power and time constant. Further experiments that we could do are presented at the end, as two suggestions of what we can achieve with this setup in the next few years. Those experiments include a Born's rule test by implementing a third slit into the setup, which can be easily achieved programmatically and no further alignment procedure would be needed once we have the main experiment running. The steps to transition to such an experiment are comparatively easy therefore. Another interesting direction we could seek is the interplay between vortices and angular momentum in relation to the BEC. It is known that angular momentum beams induce quantized vortices in a BEC, and hence we could look at the condensate in relation to entangled orbital angular momentum beams.

Appendix

Appendix 1

A small note on the micro channel plate detector

This is a delay-line type detector (DLD) that consists of four quadrants with independent delay lines and read-out electronics. Some of the potentiometers responsible for the sensitivity of each line may have to be adjusted for top performance (in our case we had to do that due to a need of repair) with a stable source of atoms across all quadrants, such as the magneto optical trap. When an atom hits the detector, it creates an electron avalanche that propagates across the wires and is amplified. The pulse is then discriminated in time via time-to-digital conversion electronics (TDC), the arrival times are recorded and the 3D information calculated. Each sector of the four quadrants has 2 wires that send 4 signals to detect the position of one atom. However, because of how it is constructed, there is a region of about 5mm in between the quadrants that is practically not usable.

Appendix 2

A note on the lifetime of the condensate

It is important to have a lifetime of the condensate significantly longer than the time needed to run an experiment. The measurements were performed by holding the atomic cloud in the trap with the evaporation sequence turn on at the final evaporation power of the trapping laser until the trap was switched off, basically a similar procedure followed the lifetime measurements described in the thesis of Mateusz Kotyrba. Then, an absorption image was taken, from which the number of condensed atoms is extracted. Fitting exponential decay, assuming one-body losses of the condensate, the

lifetime can be determined.

Appendix 3

A further note on the similarity of the BEC to a down-conversion crystal

Fundamental quantum optics experiments with a BEC would be of significant interest. It has been shown that coherent four-wave mixing in sodium-BEC matter waves of different momenta mix to produce, by means of atom-atom interactions, a fourth wave with new momentum [40]. Once one solves the Schrodinger equation for matter waves, it is evident that the nonlinear term contribution of the wave function is similar to the third order term in the wave equation for electric field describing optical four wave mixing in a nonlinear medium. Therefore, four-wave mixing of coherent matter waves is analogous to four-wave mixing in quantum optics; in a sense, the BEC acts like a nonlinear crystal. This property makes the BEC efficient as a platform for fundamental quantum optics experiments done with atoms similar to the fundamental quantum optics experiments done with light.

Collisional interactions between atoms, however, happen in the BEC all the time among the millions of atoms. The interesting thing though is that since the total momenta of the atoms compared to the momenta created by collisions within the BEC are on the same order, the signature of entanglement is practically untraceable within the BEC. The first experiment on four-wave-mixing of matter waves was performed by the group of William Phillips [70] and the benchmark experiment for characterizing single atom correlations in the four-wave-mixing process was performed using metastable helium and the delay-line micro channel plate detector by the group of Alain Aspect [71].

References

[1] Uehlinger T, Jotzu G, Messer M, Greif D, Hofstetter W, etal. Artificial grapheme with tunable interactions. arXiv: 13084401 (2013)

[2] Brantut JP, Meineke J, Stadler D, Krinner S, Esslinger T. Conduction of ultracold fermions through a mesoscopic channel. Science 337, 1069-1071 (2012)

[3] Lee JG, McIlvain BJ, Lobb C, Hill III W. Analog sof basic electronic circuit elements in a free-space atom chip. Sci Rep 3 (2013)

[4] N. schlosser, G. Reymond, and P. Grangier, "Collisional blockade in microscopic optical dipole trap," Philos. Trans. R. Soc. London, Ser. A 361, 1527-1536 (2003)

[5] D. Frese, B. Ueberholz, S. Kuhr, W. Alt, D. Schrader, V. Gomer, and D. Meschede, "Single atoms in an optical dipole trap: towards a deterministic source of cold atoms," Phys. Rev. Lett. 85, 3777-3780 (2000)

[6] S. Bergamini, B. Dariquie, M. Jones, L. Jacubowiez, A. Browaeys, and P. Grangier, "Holographic generation of microtrap arrays for single atoms by use of a programmable phase modulator," J. Opt. Soc. Am. B, 1889-1894 (2004)

[7] Gerchberg, R. W. and Saxton, W. O., A practical algorithm for the determination of phase from image and diffraction pictures, Optik, 35, 237-246 (1972)

[8] Pasienski, M. & DeMarco, B., A high-accuracy algorithm for designing arbitrary holographic atom traps, Opt. Express 16, 2176-2190 (2008)

[9] J. W. Goodman, Introduction to Fourier Optics (McGraw-Hill, 1998)

[10] A. L. Gaunt and Z. Hadzibabic, "Robust digital holography for ultracold atom trapping", Sci. Rep. 2, 721 (2012)

[11] Gabor D. A new microscopic principle. Nature 161, 777-778

(1948)

[12] Kozma A, Kelly DL. Spatial filtering for detection of signals submerged in noise, Appl Optics 4, 387-392 (1965)

[13] Huang T, Burnett J, Deczky A. The importance of phase in image processing filters. IEEE T Acoust Speech 23, 529-542 (1975)

[14] Oppenheim AV, Lim JS. The importance of phase in signals. P IEEE 69, 529-541 (1981)

[15] Millne R. P., Hsiao W. H. The basis of phase dominance, Opt. Letters, Vo.34, 2607-2609 (2009)

[16] Jesacher A., Schwaighofer A., F'urhapter S., Maurer C., Bernet S., and RitschMarte M., Wavefront correction of spatial light modulators using an optical vortex image, Opt. Expr., 15:5801-5808 (2007)

[17] Max Born, Emil Wolf, et al, Principles of Optics (1999)

[18] F. Nogrette, H. Labuhn, S. Ravets, D. Barredo, L. Beguin, A. Vernier, T. Lahaye and A. Broweys, Single atom trapping in holographic 2D arrays of microtraps with arbitrary geometries, Phys. Rev. X 4 021034 (2014)

[19] P. Coullet, L. Gil, and F. Rocca, "Optical vortices," Opt. Commun., vol. 73, no. 5, pp. 403–408, Nov. 1989.

[20] J. Kofler, M. Singh, M. Ebner, M. Keller, M. Kotyrba & A. Zeilinger, Phys. Rev. A **86** (2012) 032115 [21] A. Zeilinger, Rev. Mod. Phys. 71, S288 (1999)

[22] D. V. Strekalov, A. V. Sergienko, D. N. Klyshko, and Y. H. Shish, Phys. Rev. Lett. 74, 3600 (1995)

[23] B. Dopfer, PhD Thesis, University of Innsbruck (1998) [24] P. H. S. Ribeiro and G. A. Barbosa, Phys. Rev. A. 54, 3489 (1996)

[25] A. Perrin, H. Chang, A. Krachmalnicoff, M. Schellekens, D. Boiron, A. Aspect, and C. I. Westbrook, Phys. Rev. Lett. 99, 150405 (2007)

[26] M. Horne, Two-particle diffraction in: Experimental Metaphysics, edited by R. S. Cohen, M. Horne, and J. Stachel (Kluwer Academic Publishers, Experimental Metaphysics, Vol-1, BSPS Vol-193 (1997)

[27] A. Perrin, R. Bücker, S. Manz, T. Betz, C. Koller, T. Plisson, T.

Schumm, and J. Schmiedmayer, Hanbury Brown Twiss correlations across the Bose- Einstein condensation threshold, *Nature Physics* (2012)

[28] E. G. van Putten, I. M. Vellekoop, A. P. Mosk, Spatial amplitude and phase modulation using commercial twisted nematic LCDs, Applied Optics, Vol. 47, Issue 12, pp. 2076-2081 (2008)

[29] M. Montes-Usategui, E. Pleguezuelos, J. Andilla, E. Martin-Badosa, Fast generation of holographic optical tweezers by random mask encoding of Fourier components, Optics Extress, Vol. 14, Issue 6, pp. 2101-2107 (2006)

[30] A. Jesacher, Application of spatial light modulators for optical trapping and image processing, Thesis

[31] Askar'yan, G. A. Sov. Phys. JETP 15, 1088 (1962)

[32] Kazantsev, A. P. Sov. Phys. JETP 36, 861 (1973), ibid. 39, 784 (1974)

[33] Gordon, J. P., Ashkin, A. Phys. Rev. A 21, 1606 (1980)

[34] R. Grimm, M. Weidemüller, and Y. Ovchinnikov, "Optical dipole traps for neutral atoms," Adv. At. Mol. Opt. Phys. Vol. 42, pp.95-170, 2000

[35] Rob van Rooij, PhD thesis, Frequency metrology in quantum degenerate helium

[36] K. M. O'Hara, M. E. Gehm, S. R. Granade, and J. E. Thomas, Scaling laws for evaporative cooling in time-dependent optical traps, Phys. Rev. A. 64:051403, Oct 2001

[37] J. D. Miller, R. A. Cline, and D. J. Heinzen, Phys. Rev. A, 47, R4567 (1993)

[38] O. J. Luiten, M. W. Reynolds, and J. T. M. Walraven, Phys. Rev. Lett. 74, 3577 (1995)

[39] A. Perrin, H. Chuang, V. Krachmalnicoff, M. Schellekens, D. Boiron, A. Aspect & C. Westbrook, Phys. Rev. Lett. 99, 150405 (2007)

[40] L. Deng, E. W. Hagley, J. Wen, N. Trippenbach, Y. B. Band, P. S. Julienne, J. E. Simsarian, K. Helmerson, S. L. Rolston and W. D. Phillips, Nature (London) 398, 218 (1999)

[41] U. Sinha, C. Couteau, T. Jannewein, R. Laflamme and G. Weihs,, Ruling out multi-order interference in quantum mechanics, Science 329, 418 (2010)

[42] R. Gahler, A. G. Klein, and A. Zeilinger, "Neutron optical tests of nonlinear wave mechanics," *Phys. Rev. A,* vol. 23, no. 4, pp. 1611-1617, 1981.

[43] Iwo Białynicki-Birula and Jerzy Mysielski, "Nonlinear Wave Mechanics," *Annals of Physics,* vol. 100, pp. 62-93, 1976.

[44] Rahul Sawant, Joseph Samuel, Aninda Sinha, Supurna Sinha, and Urbasi Sinha, "Nonclassical Paths in Quantum Interference Experiments," *PRL,* vol. 113, no. 12, p. 120406, 2014.

[45] M. A. Rowe, D. Kielpinski, V. Meyer, C. A. Sackett, W. M. Itano, C. Monroe, and D. J. Wineland, Experimental violation of a Bell's inequality with e cient detection, Nature 409 (2001), no. 6822, 791–794

[46] R. Blatt and D. Wineland, Entangled states of trapped atomic ions, Nature 453 (2008), no. 7198, 1008–1015

[47] M. Ste↵en, M. Ansmann, R. C. Bialczak, N. Katz, E. Lucero, R. Mcdermott, M. Nee- ley, E. M. Weig, A. N. Cleland, and J. M. Martinis, Measurement of the Entangle- ment of Two Superconducting Qubits via State Tomography, Science 313 (2006), no. 5792, 1423–1425

[48] C. Gross, H. Strobel, E. Nicklas, T. Zibold, N. Bar-Gill, G. Kurizki, and M. K. Oberthaler, Atomic homodyne detection of continuous-variable entangled twin-atom states., Nature 480 (2011), no. 7376, 219–223

[49] J. G. Rarity and P. R. Tapster, Experimental Violation of Bell's Inequality Based on Phase and Momentum, Physical Review Letters 64 (1990), no. 21, 2495–2498

[50] A. J. Ferris, M. K. Olsen, E. G. Cavalcanti, and M. J. Davis, Detection of continu- ous variable entanglement without coherent local oscillators, Physical Review A 78 (2008), no. 6, 060104–1–060104–4

[51] A. J. Ferris, M. K. Olsen, and M. J. Davis, Atomic entanglement generation and de- tection via degenerate four-wave mixing of a Bose- Einstein condensate in an optical lattice, Physical Review A 79 (2009), no. 4, 043634–1–043634–11

[52] J. Kofler, M. Singh, M. Ebner, M. Keller, M. Kotyrba, and A. Zeilinger, Einstein-Podolsky-Rosen correlations from colliding Bose-Einstein condensates, Physical Re- view A 86 (2012), no. 3, 032115–1–032115–5

[53] Z. Y. Ou, X. Y. Zou, L. J. Wang, and L. Mandel, Observation of Nonlocal Interference in Separated Photon Channels, Physical Review Letters 65 (1990), no. 3, 321–324

[54] Z. Y. Ou, S. F. Pereira, H. J. Kimble, and K. C. Peng, Realization of the Einstein- Podolsky-Rosen Paradox for Continuous Variables, Physical Review Letters 68 (1992), no. 25, 3663–366

[55] F. M. Penning, Über Ionisation durch metastabile Atome, Die Naturwissenschaften 15 (1927), no. 40, 818

[56] A. Günther, S. Kraft, M. Kemmler, D. Koelle, R. Kleiner, C. Zimmermann, and J. Fortagh, Diffraction of a Bose-Einstein Condensate from a magnetic lattice on a microchip, Phy. Rev. Lett. 95, 170405 (2005)

[57] A. Zeilinger, Rev. Mod. Phys. 71, S288 (1999)

[58] D. V. Strekalov, A. V. Sergienko, D. N. Klyshko, and Y. H. Shih, Phys. Rev. Lett. 74, 3600 (1995).

[59] B. Dopfer, PhD Thesis, University of Innsbruck (1998) [60] P. H. S. Ribeiro and G. A. Barbosa, Phys. Rev. A. 54, 3489 (1996).

[61] P. G. Kwiat, K. Mattle, H. Weinfurter, A. Zeilinger, A. V. Sergienko, and Y. Shih, Phys. Rev. Lett. 75, 4337 (1995)

[62] L. Deng, E. W. Hagley, J.Wen, M. Trippenbach, Y. Band, P. S. Julienne, J. E. Simsarian, K. Helmerson, S. L. Rolston, and W. D. Phillips, Nature 398, 218 (1999).

[63] J. M. Vogels, K. Xu, and W. Ketterle, Rev. Rev. Lett. 89, 020401 (2002).

[64] J. Vogels, J. K. Chin, and W. Ketterle, Rev. Rev. Lett. 90, 030403 (2003)

[65] T. Jeltes, J. M. McNamara, W. Hogervorst, W. Vassen, V. Krachmalnicoff, M. Schellekens, H. C. A. Perrin, D. Boiron, A. Aspect, and C. I. Westbrook, Nature. 445, 402 (2007).

[66] S. Thankvanthri, K. Kapale, J. Dowling, Arbitrary coherent superpositions of quantized vortices in Bose-Einstein condensates via orbital angular momentum of light, Phys. Rev. A 77, 053825 (2008)

[67] J. F. S. Brachmann, W. S. Bakr, J. Gillen, A. Peng, and M. Greiner, Inducing vortices in a Bose-Einstein condensate using holographically produced light beams, Optics Express, Vol. 19, Issue 14, pp. 12984-12991 (2011)

[68] D. Ding, W. Zhang, Z. Zhou, S. Shi, G. Xiang, X. Wang, Y. Jiang, B. Shi, G. Guo, Quantum storage of orbital angular momentum entanglement in an atomic ensemble, Phys. Rev. Lett. 114, 050502, (2015)

[69] A. Bhowmik, P. Mondal, S. Majumder, B. Deb, Forming superposition of vortex states in Bose Einstein condensates by a non-paraxial Laguerre- Gaussian beam, arXiv:1602.06405

[70] L. Deng, E. W. Hagley, J. Wen, M. Trippenbach, Y. Band, P. S. Julienne, J. E. Simsarian, K. Helmerson, S. L. Rolston, and W. D. Phillips, Four-wave- mixing with matter waves, Nature 398, 218 (1999)

[71] A. Perrin, H. Chang, V. Krachmalnicoff, M. Schellekens, D. Boiron, A. Aspect, and C. I. Westbrook, Observation of atom pairs in spontaneous four-wave-mixing of two colliding Bose-Einstein condensates, Physical Review Letters 99, 150305 (2007)

[72] Stenholm, S., The semi-classical theory of laser cooling, Rev. Mod. Phys. 58, 699 (1986)

[73] Minogin, V. G., and Letokhov, V. S., Laser light pressure on atoms, Gordon and Breach, NY (1987)

[74] Arimondo E., Phillips, W.D., and Strumia F., eds. (1992), Laser manipulation of atoms and ions, Proceedings of the international school of Physics “Enrico Fermi”, Varenna, 1991, (North Holland, Amsterdam)

[75] Metcalf H., and van der Straten P., Cooling and trapping of neutral atoms, Phys. Rep. 244, 203 (1994)

[76] Vuletic V., Chin C., Kerman A. J., and Chu. S., Beyond optical molasses: 3D Raman sideband and cooling of atomic cesium to high

phase-space density, Phys. Rev. Lett. 84, 3 (2000)

[77] Wallis H., Dalibard J., and CohenTannoudji C., Trapping atoms in a gravitational cavity, Appl. Phys. B 54, 407 (1992)

[78] Phillips, D. W., Nobel Lecture: Laser cooling and trapping of neutral atoms, Rev. Mod. Phys. 70, 721 (1998)

[79] Askar'yan G. A., Sov. Phys. JETP 15, 1008 (1962) [80] Letokhov V. S., JETP Lett. 7, 272 (1968)

[81] Ashkin, A., Acceleration and trapping of particles by radiation pressure, Phys. Rev. Let. 24, 156 (1970)

[82] Bjorkholm J. E., Freeman R.R., Ashkin A., and Pearson D. B., Observation of focusing of neutral atoms by the dipole forces of resonance- radiation pressure, Phys. Rev. Lett. 41, 1361 (1978)

[83] Chu. S., Bjorkholm J.E., Ashkin A., and Cable A., Experimental observation of optically trapped atoms, Phys. Rev. Lett. 57, 314 (1986)

[84] Gaunt A., Schmidutz T., Gotlibovych I., Smith R., and Hadzibabic Z., Bose-Einstein condensation of atoms in a uniform potential, Phys. Rev. Lett. 110, 200406 (2013)

[85] Andersen M. F., Ryu C., Claude P., Natarajan V., Vaziri A., Helmerson K., and Phillips W. D., Quantized rotation of atoms from photons with orbital angular momentum, Phy. Rev. Lett. 95, 170406 (2006)

[86] Wright K. C., Leslie L. S., Bigelow N. P., Optical control of internal and

external angular momentum of a Bose-Einstein condensate , Phys. Rev. A 77, 041601(R) (2008)

[87] Wright K. C., Leslie L. S., Hansen A., Bigelow N. P., Sculpting the vortex space of a Spinor BEC Phys. Rev. Lett. 102, 030405 (2009)

[88] Brachmann J. F. S., Bakr W. S., Gillen J., Peng A., and Greiner M., Inducing vortices in a Bose-Einstein condensate using holographically produced light beams, Opt. Express 19, 12984 (2011)

[89] Quinteiro G. F., Kuhn T., Light-hole transitions in quantum dots: Realizing full control by highly focused optical vortex beams, Phys

Rev. B 90, 115401 (2014)

[90] Toyoda K., Miyamoto K., Aoki N., Morita R., and Omatsu T., Using optical vortex to control the chirality of twisted metal nanostructures, Nano Letters 12(7), 36453649 (2012)

[91] Liu M., Wen L. H., Xiong H. W., and Zhan M. S., Structure and generation of the vortex-antivortex superposed state in Bose-Einstein condensates, Phys. Rev. A 73, 063620 (2006)

[92] Ling W. H., Wang J., Feng J., Hu H., Dynamics of Bose-Einstein condensed vortex-antivortex superposed states in a two dimensional infinite depth square well , J. Phys. B: At. Mol. Opt. Phys. 41 135301 (2008)

[93] Wen L., Qiao Y., Xu Y., Mao L., Structure of two component Bose-Einstein condensates with respective vortex-antivortex superposition states, Phys. Rev. A 87, 033604 (2013)

[94] Allen L., Beijersbergen, Spreeuw R. J. C.; Woerdman J. P., Orbital angular momentum of light and the transformation of Laguerre-Gaussian laser modes, Phys. Rev A 45, 8185 (1992)

[95] Olson A., Niffenegger R., Chen Y., Optimizing the efficiency of evaporative cooling in optical dipole traps, arXiv 1211.3469 (2012)

[96] Jaksch D., Cirac J. I., Zoller P., Rolston S. L., Cote R., and Lukin M. D., Fast quantum gates for neutral atoms, Phys. Rev. Lett. 85, 2208-2011 (2000)

[97] Protsenko, Reymond G., Schlosser N, and Grangier P., Operation of a quantum phase gate using neutral atoms in microscopic dipole traps, Phys. Rev. A 65, 052301 (2002)

[98] Brennen G. K., Deutsch I. H., Jessen P. S., Entangling dipole-dipole interactions for quantum logic with neutral atoms, Phys. Rev. A 61, 062309 (2000)

[99] Brennen G. K., Caves C. M., Jessen P. S., and Deutsch I. H., Quantum logic gates in optical lattices, Phys. Rev. Lett 82, 1060-1063 (1999)

[100] Calarco T., Hinds E. A., Jaksch D., Schmiedmayer J., Cirac I., and Zoller P., Quantum gates with neutral atoms: controlling collisional interactions in time-dependent traps, Phys. Rev. A 61, 022304 (2000)

[101] Jaksch D., Briegel H.-J., Cirac J. I., Gardiner W., and Zoller P., Entanglement of atoms via cold controlled collisions, Phys. Rev. Lett. 82, 1975-1978 (1999)

[102] Mompart J., Eckert J., Ertmer W., Birkl G., and M. Lewenstein, Quantum computing with spatially delocalized qubits, Phys. Rev. Lett. 90, 147901 (2003)

[103] Eckert K., Mompart J., Yi X. X., Schliemann J., Bruss G., Birkl G., Lewenstein M., Quantum computing in optical microtraps based on the motional states of neutral atoms, Phys. Rev. A 66, 042317 (2002)

[104] Mateusz Kotyrba, PhD Thesis, Zeilinger Group

[105] Maximilian Ebner, PhD Thesis, Zeilinger Group